"Detection of underwater mines using sonar"

Pirot, Lucas

ABSTRACT

Currently, underwater mines and unexploded ordnance represent a persistent threat to maritime navigation and the environment. In submarine warfare, detecting such objects is particularly challenging, especially when they are abandoned and buried under sand. To address this issue, mine countermeasures have been developed that take advantage of various technologies, including acoustic and electromagnetic waves. Recently, new modeling approaches for ground penetrating radar (GPR) have led to significant advancements in the detection of buried landmines. The aim of this work is therefore to adapt the GPR methodology to enhance the detection and classification of underwater targets using sonar systems. To achieve this, laboratory experiments were conducted to simulate various scenarios involving a sonar sensor, a sediment layer, and various targets. Particular attention was given to understanding the measurements and pre-processing steps specific to the sensor. Subsequently, extensive numerical simulations were performed to validate and compare the results obtained experimentally. This comparison involved introducing the concept of a perfect acoustic reflector (PAR), which is useful for retrieving the transfer functions of the sonar-hydrophone-multilayered media system. These experiments highlighted both the limitations and potential of the model for analyzing realistic scenarios. Technical limitations such as the size of the water tank and sensor limitations, posed challenges to fully achieving the objectives. Despite these difficulties, the results contribute to a deeper und...

CITE THIS VERSION

Pirot, Lucas. *Detection of underwater mines using sonar.* Faculté des bioingénieurs, Université catholique de Louvain, 2025. Prom. : Lambot, Sébastien ; Hurtado Erasso, Camilo. http://hdl.handle.net/2078.1/thesis:49946

Faculty of Bioscience Engineering

Detection of underwater mines using sonar

Adapting a GPR methodology to enhance classification

Author	Pirot Lucas
Supervisors	Lambot Sébastien (UCLouvain) Hurtado E. Camilo A. (UCLouvain/Royal Military Academy)
Readers	Lopera Tellez Lucia Olga (Royal Military Academy) Hanert Emmanuel (UCLouvain)
Academic year	2024 - 2025

Thesis presented in partial fulfillment of the requirements for the degree of Bioengineer in environmental science and technology

Abstract

Currently, underwater mines and unexploded ordnance represent a persistent threat to maritime navigation and the environment. In submarine warfare, detecting such objects is particularly challenging, especially when they are abandoned and buried under sand. To address this issue, mine countermeasures have been developed that take advantage of various technologies, including acoustic and electromagnetic waves.

Recently, new modeling approaches for ground penetrating radar (GPR) have led to significant advancements in the detection of buried landmines. The aim of this work is therefore to adapt the GPR methodology to enhance the detection and classification of underwater targets using sonar systems.

To achieve this, laboratory experiments were conducted to simulate various scenarios involving a sonar sensor, a sediment layer, and various targets. Particular attention was given to understanding the measurements and pre-processing steps specific to the sensor.

Subsequently, extensive numerical simulations were performed to validate and compare the results obtained experimentally. This comparison involved introducing the concept of a perfect acoustic reflector (PAR), which is useful for retrieving the transfer functions of the sonar-hydrophone-multilayered media system.

These experiments highlighted both the limitations and potential of the model for analyzing realistic scenarios. Technical limitations such as the size of the water tank and sensor limitations, posed challenges to fully achieving the objectives. Despite these difficulties, the results contribute to a deeper understanding of acoustic propagation mechanisms and pave the way for future optimizations in underwater detection applications by using the approach of adapting the GPR methodology.

Acknowledgments

At the end of this work, I can finally look back on the series of adventures that have unfolded over the past year. With a great deal of emotion and a hint of nostalgia, I would like to express my gratitude to all the people who supported me during the completion of this Master's thesis.

Let me begin with my supervisor. Prof. Sébastien Lambot gave me the opportunity to work on a topic that deeply fascinates me: the design of experiments. He allowed me to combine this passion with a highly interesting field, acoustic waves. I am immensely grateful for his insightful advice and the structure he established throughout my work.

I would also like to thank Camilo A. Hurtado E. for his invaluable help and his undeniable talent for explaining, with ease, concepts that initially seemed so complicated to me. Camilo has always shown enthusiasm for my work and motivated me to continually push myself further. For that, I will never be able to thank him enough.

I wish to extend my gratitude to my readers, Lopera Tellez Lucia Olga and Hanert Emmanuel. I am deeply grateful for the time they will dedicate to reading my writings.

I would also like to thank the IT team, namely Bernard Niedergang and Fabienne Delbrouck, without whom access to the supercomputer would not have been possible, as well as Sébastien François, who enabled me to set up my experimental projects.

Finally, but certainly not least, I take these last few lines to warmly thank my family. Their trust and encouragement have allowed me to progress to where I stand today. I am eternally grateful to them.

Contents

List of Figures

List of Tables

List of Acronyms

UXO Unexploded Ordnance

MCM Mine Countermeasures

SBSS Sub-Bottom Scanning Sonar

SAS Synthetic Aperture Sonar

GPR Ground Penetrating Radar

PAR Perfect Acoustic Reflector

ROV Remotely Operated Vehicles

USV Underwater Surface Vehicles

SBES Single-Beam Echo Sounder

MBES Multi-Beam Echo Sounder

SBS Single-Beam Sonar

SBP Sub-Bottom Profiler

SSS Side-Scan Sonar

TS Target Strength

ADC Analog-to-Digital Converter

PEC Perfect Electromagnetic Conductor

PSTD Pseudo-Spectral Time Domain

AUV Autonomous Underwater Vehicle

Chapter 1

Introduction

1.1 General context

Since the nineteenth century, the use of underwater mines has increased. More than 550,000 underwater mines have been deployed only during World War II, both for offensive purposes and to defend aquatic territories. However, not all of these mines have been neutralized and still pose a significant threat to navigation and other maritime activities. Furthermore, the presence of underwater mines, along with UXO, poses an environmental concern. UXOs refers to explosive munitions that were armed and used, but did not detonate as intended. Both underwater mines and UXOs contain material components and chemical substances that can lead to environmental contamination [Tellez et al., 2017] [McDonald, 2008].

Today's mines are even more sophisticated and dangerous. They are stealthier, harder to detect, and equipped with advanced electronics that make them highly effective and elusive [Staelens, 2009]. In order to counteract the danger posed by these mines, various measures are taken. These precautions are called Mine Countermeasures (MCM). They can be both passive and active. One of these active measures is called 'mine hunting', which consists in detecting mines within a certain perimeter. Thus, mine hunting consists of four main stages: detection, classification, identification, and disposal. The first involves finding potential targets through the use of signals (magnetic or acoustic). The second step is to determine whether the target is a mine-like object or a completely harmless object. The third step involves the use of additional measures to confirm more precisely what type of mine it is, and finally the last step involves neutralizing the explosive object [Hożyń, 2021].

1.2 The sub-bottom scanning sonar (SBSS) project

In active measures against underwater mines, sonar systems play a crucial role in the location and identification of potentially dangerous objects buried beneath the seabed. The Sub-Bottom Scanning Sonar (SBSS), a project carried out between the Belgian navy and various public and private institutions, stands out for its innovative approach, focused on developing a low-frequency, high-speed sonar system to detect, classify and identify targets, either above the seabed or buried within the sediment.

The SBSS system uses frequencies below 20 kHz to take advantage of the specific resonances of buried objects, helping to differentiate them. The SBSS transmitter emits wideband chirp signals within an angular sector of ±120°, providing extensive coverage and capturing echoes through a system of hydrophones oriented transversely to the device's trajectory (across the track). Subsequently, a process known as Synthetic Aperture Sonar (SAS) is applied longitudinally (along-track).

This signal processing method, combined with detailed acoustic analysis, enables a more efficient distinction between real targets and harmless objects, thus reducing the number of false positives often seen with traditional sonar technologies. The use of acoustic resonances, still underutilized in this field, offers a significant advantage for target recognition.

Building on the framework of the SBSS project, this thesis aims to collect experimental data and apply a GPR method to improve the classification process of mine-like objects.

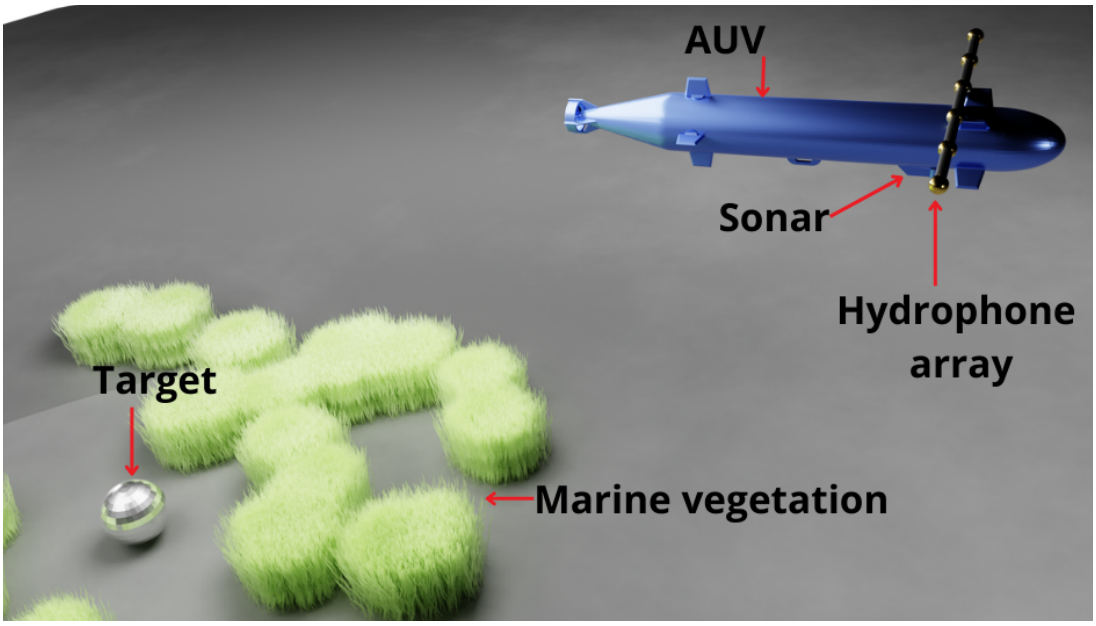

Figure 1.1: Simulated image of an Autonomous Underwater Vehicle (AUV) conducting mine and UXOs search using sonar. Image from [Hurtado Erasso, 2024].

1.3 Objectives

1.3.1 General objective

The general objective of the thesis is to adapt a proven GPR methodology that aims to enhance the signals received by a sonar and therefore improve the classification process of targets. Specifically, this work leverages the analogies between electromagnetic and acoustic wave propagation to apply advanced signal processing techniques originally developed for GPR such as the modeling approaches proposed by Lambot et al. [2004] and Lopera et al. [2007]. These methods include the characterization and filtering of parasitic reflections, retrieval of transfer functions, and inversion of Green's functions to localize and identify buried objects.

1.3.2 First specific objective

The first specific objective is to design an experiment involving a sonar sensor. The purpose of this experiment is to carry out and understand the measurements and pre-processing of the data in order to retrieve the raw full waveform, specifically cleaned of the gain function, for multiple scenarios.

1.3.3 Second specific objective

The second specific objective is to compare and validate the experimental results of the scenarios against numerical simulations. This comparison involves introducing the concept of a perfect acoustic reflector (PAR). This concept will also be useful for subsequent simulations aimed at retrieving the transfer functions of the sonar-hydrophone-multilayered media system. To achieve this, measurements with a PAR and results from the Green's function of 3D elastic wave propagation in a multilayered medium are required.

1.3.4 Third specific objective

The third specific objective is to perform measurements for a set of configurations involving the concept of layers as well as targets. Thus, various layer thicknesses and targets will be used to apply the GPR methodology.

Chapter 2

State of the art

2.1 Elastic and acoustic waves

When an acoustic wave (an oscillatory pressure disturbance) propagates in a fluid and encounters an immersed solid object, it induces elastic waves within that object. These elastic waves propagate through all parts of the structure and, in turn, generate pressure waves in the surrounding fluid, known as scattered waves or echoes [Burnett, 2015]. These concepts have direct applications in the propagation of waves through solids and fluids. The pioneering work of Newton, Hooke, Cauchy, and Navier laid the foundations for understanding dynamic elasticity, allowing us to predict and explain the propagation of disturbances in solids [Sánchez-Sesma and Iturrarán-Viveros, 2021].

Waves, whether elastic or acoustic (so named because they are responsible for the propagation of sound in a medium), are disturbances that propagate through materials, carrying energy without causing a permanent displacement of the material itself. As these waves travel through a material, they induce a temporary deformation, and once the wave dissipates, the material returns to its original shape. This behavior is characteristic of elastic waves, including body waves, a term used to describe waves propagating through the interior of any elastic medium. In the context of Earth, body waves are referred to as seismic waves [Selim Saleh, 2021]. These waves, divided into P-waves (longitudinal or compression) and S-waves (transverse or shear), and which differ in the way they move (see Figure 2.1), directly depend on the elastic properties of the materials through which they travel (e.g., density, Young's modulus, shear modulus, and Poisson's ratio) [Walley and Field, 2016].

The elasticity of a material, which is an approximation of its behavior under low deformation, helps to better understand this phenomenon. An ideal elastic material deforms proportionally to the applied load and returns to its original state without incurring damage. Thus, an elastic wave in this context is a mechanical disturbance that causes particle oscillations around their equilibrium position, without permanent change. However, in real materials, this propagation is affected by dissipation mechanisms, leading to wave attenuation depending on the distance traveled. The attenuation rate generally depends on the frequency of the wave, while the velocity determines how quickly the disturbance propagates through the medium [Walley and Field, 2016].

Acoustic waves, which propagate in fluids such as air and water, are a subdivision of elastic waves with a notable difference: they are always longitudinal. Elastic waves traveling in solids can also be transverse [Sánchez-Sesma and Iturrarán-Viveros, 2021]. In the field of oceanography, this understanding of acoustic and elastic waves is essential, particularly to predict the acoustic scattering by underwater objects [Burnett, 2015].

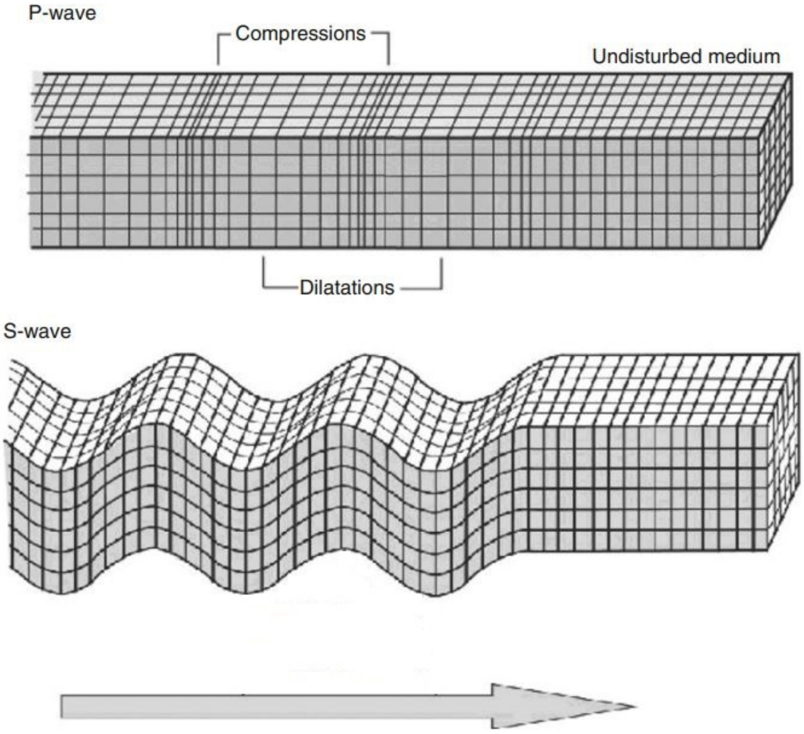

Figure 2.1: P-wave and S-wave motion. The arrow shows the direction that the wave is moving [Selim Saleh, 2021]

2.2 Governing equations

2.2.1 Elastic waves

Elastic waves are longitudinal and shear perturbations in solids, represented by displacement, pressure, or even velocity fields. The foundational work of Newton, Hooke, Cauchy, and Navier established the basis of dynamic elasticity theory in the early 19th century. Among the simplest solutions to the wave equation are plane waves, first described by D'Alembert. These plane waves are crucial for studying the propagation of elastic waves, especially in layered media and on material surfaces [Sánchez-Sesma and Iturrarán-Viveros, 2021].

The main physical variables are as follows:

- $\mathbf{u}(\mathbf{x}, t)$: the displacement (time-dependent vector field),
- ε: the strain tensor, defined as

  $$\varepsilon = \frac{1}{2}(\nabla\mathbf{u} + \nabla\mathbf{u}^T), \tag{2.1}$$

  where ∇ is the nabla operator, used to calculate the gradient (∇), the divergence ($\nabla \cdot \mathbf{u}$), or the rotational ($\nabla \times \mathbf{u}$)
- σ: the stress tensor which was developed by Cauchy and is related to the strain by Hooke's law:

  $$\sigma = \lambda(\nabla \cdot \mathbf{u})\mathbf{I} + 2\mu\varepsilon, \tag{2.2}$$

  where λ and μ are the Lamé parameters also known as the Lamé's constant and the Shear modulus, respectively. The units of λ and μ are both Pa (Pascal). λ refers to longitudinal waves (compressional waves) and μ corresponds to transverse waves (shear waves).

The wave equation for an isotropic medium (where all the waves travel at the same speed regardless of the direction in which they propagate), derived from the conservation of momentum ($\sum \vec{F} = m\vec{a}$, where m is the mass and $\vec{a}$ is the resulting acceleration), is given by Demanet [2012] as:

$$\rho \frac{\partial^2 \mathbf{u}}{\partial t^2} = \nabla(\lambda \nabla \cdot \mathbf{u}) + \nabla \cdot [\mu(\nabla \mathbf{u} + (\nabla \mathbf{u})^T)], \tag{2.3}$$

where ρ is the density of the medium (kg/m^3).

By using vector identities, and by using the assumption that λ and μ are constant, this equation can be simplified to:

$$\rho \frac{\partial^2 \mathbf{u}}{\partial t^2} = (\lambda + 2\mu)\nabla(\nabla \cdot \mathbf{u}) - \mu \nabla \times (\nabla \times \mathbf{u}). \tag{2.4}$$

Decomposing the displacement $\mathbf{u}$ into a scalar potential ϕ (longitudinal waves) and a vector potential ψ (transverse waves) via the Helmholtz decomposition:

$$\mathbf{u} = \nabla \phi + \nabla \times \psi, \tag{2.5}$$

we obtain the following wave equations [Dourado, 2015]:

$$\frac{\partial^2 \phi}{\partial t^2} = c_P^2 \Delta \phi, \tag{2.6}$$

$$\frac{\partial^2 \psi}{\partial t^2} = c_S^2 \Delta \psi, \tag{2.7}$$

where the wave speeds are given by:

$$c_P = \sqrt{\frac{\lambda + 2\mu}{\rho}}, \tag{2.8}$$

$$c_S = \sqrt{\frac{\mu}{\rho}}, \tag{2.9}$$

with corresponding wave numbers,

$$k_P = \frac{\omega}{c_P}, \tag{2.10}$$

$$k_S = \frac{\omega}{c_s}, \tag{2.11}$$

where ω is the angular frequency ($\omega = 2\pi{*}f$, where f is the frequency), k_p and k_s are respectively the wave number in rad/m of the P-waves and S-waves. Finally, the wave speed c corresponds to the speed of P-waves (c_P) and S-waves (c_S) Note that P-waves propagate faster than the S-waves, with $c_P \geq \sqrt{2} c_S$.

Note : The assumption that λ and μ are constant is a very strong one: there is a lot of physics in the coupling of ϕ and ψ that the above reasoning does not capture (material heterogeneity, non-linear elasticity, anisotropy, and viscoelastic dissipation).

2.2.2 Acoustic waves

Acoustic waves can be seen as a special case of elastic waves, occurring in fluid media (liquids or gases), where only compressional waves are present (no shear waves). In this case, the displacement $\mathbf{u}$

is reduced to a scalar pressure field $p(\mathbf{x}, t)$, and the equation of the elastic wave is simplified.

The governing equations for acoustic waves are ([Demanet, 2012]):

$$\frac{\partial \mathbf{v}}{\partial t} = -\frac{1}{\rho_0}\nabla p, \tag{2.12}$$

$$\frac{\partial p}{\partial t} = -\kappa_0 \nabla \cdot \mathbf{v}, \tag{2.13}$$

where ρ_0 is the density and κ_0 is the bulk modulus (more information about the bulk modulus in the Appendix A). They are both related to the wave speed c through $\kappa_0 = \rho_0 c^2$.

Combining these two equations yields the scalar wave equation for pressure:

$$\frac{\partial^2 p}{\partial t^2} = c^2 \Delta p. \tag{2.14}$$

This equation is analogous to the longitudinal wave equation for elastic waves.

2.3 Reflection and transmission coefficients

The interaction of an incident wave at the interface between two media with different acoustic impedances results in a reflected wave and a transmitted wave, as illustrated in Figure 2.2. The angles of incidence, reflection, and transmission are denoted by θ, θ_r, and θ_1, respectively. However, when the interface is not flat, the wave may scatter in different directions, leading to multiple reflections or diffractions. Additionally, when the sediment is not a fluid, the waves may generate surface waves like Rayleigh waves. Wave propagation can become highly complex [Urick, 1983].

The reflection coefficient V and the transmission coefficient W are defined as ([Pierce, 2019] [Brekhovskikh and Lysanov, 2006]):

$$V = \frac{Z_1 - Z}{Z_1 + Z}, \tag{2.15}$$

$$W = 1 + V, \tag{2.16}$$

where $Z = \rho c/\cos\theta$ and $Z_1 = \rho_1 c_1/\cos\theta_1$ are the acoustic impedances of medium 1 and medium 2. Here, ρ and c denote the density and speed of sound in the medium.

The relationship between the angles of the incident and transmitted waves is governed by Snell's law:

$$\frac{\sin\theta}{\sin\theta_1} = \frac{c}{c_1}. \tag{2.17}$$

In accordance with the law of reflection, the angle of incidence θ is equal to the angle of reflection θ_r:

$$\theta_r = \theta. \tag{2.18}$$

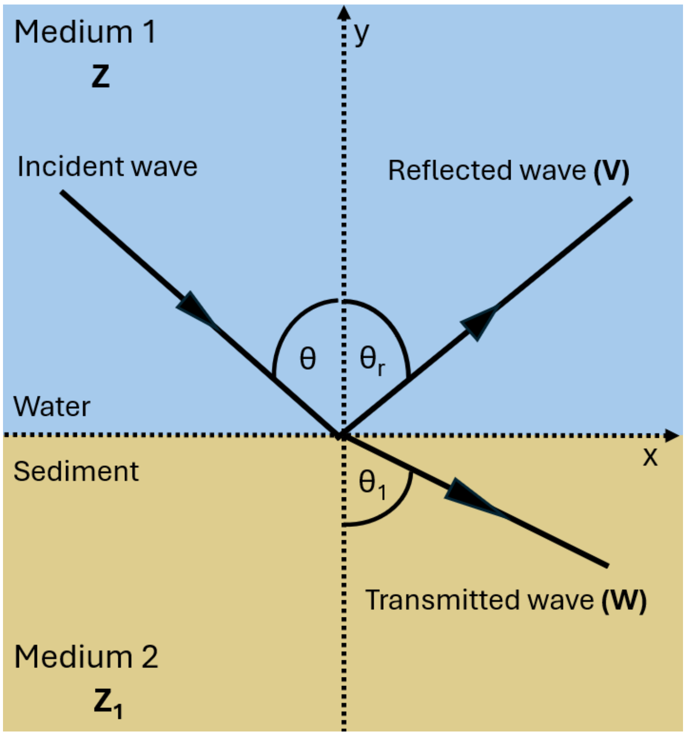

Figure 2.2: Schematic representation of wave interaction at the interface between two layers. The angles of incidence (θ), reflection (θ_r), and transmission (θ_1) are defined with respect to the normal to the interface. The reflection coefficient (V) and transmission coefficient (W) are the wave amplitudes between the reflected and transmitted waves.

2.4 Far field and near field

Sonar technology uses acoustic waves to detect and locate underwater objects. The propagation of sound from the source can be divided into two distinct regions which are important to differentiate: the near-field and the far-field. These two regions are characterized by their distance from the sound source.

2.4.1 Near field

The near field is the region located in the direct vicinity of the sound source. Generally, this distance is defined as being less than one wavelength of the emitted sound. Thus, it is located at a distance d such that:

$$d < \frac{D^2}{\lambda} \tag{2.19}$$

Here, D represents the diameter of the transmitting antenna and λ the wavelength of the sound [Urick, 1983].

In this region, acoustic waves are still in the formation process and are characterized by relatively complex variations in acoustic pressure and particle velocity, largely due to numerous interferences originating from different points of the sound source [Clay and Medwin, 1977]. For this reason, the data that can be collected in this specific area are difficult to interpret without specialized processing.

2.4.2 Far field

The far field, on the other hand, is located beyond the near field, where acoustic waves behave and propagate in a more coherent manner and can be approximated as plane waves. The far field begins at a distance [Lurton, 2010]:

$$d > \frac{D^2}{\lambda} \tag{2.20}$$

In this zone, the acoustic waves are more uniform and their behavior is easier to predict. This area is much more widely used by sonar systems due to its characteristics and is particularly useful for object detection Clay and Medwin [1977]. Note that the target itself behaves similarly to an antenna, producing an echo that can propagate in both the near and far fields. In non-monostatic configurations (when source and receiver are not aligned in the same direction), hydrophones are preferably positioned in the far field of the target's echo, where acoustic waves are more uniform and less affected by spatial variations.

2.5 Analogy between GPR and sonar

GPR has evolved over the last two decades, establishing itself as an important non-invasive electromagnetic technology in fields as diverse as environmental engineering or even archaeology [Tran et al., 2013]. One of GPR's major advances lies in its ability to detect landmines of any material. This technology offers a depth range that is greater than that of conventional metal detectors. These same characteristics make GPR a highly promising and effective method for mine clearance operations [Giannakis et al., 2015].

Acoustic waves and electromagnetic waves may appear different at first glance: the former propagate through particle vibrations in a medium, such as air or water, while the latter consist of variations in electric and magnetic fields and can propagate even in a vacuum. However, similarities can be drawn between these two types of waves, particularly in terms of the mathematical equations that describe them. Just look at how similar the pressure variations in an acoustic wave are to the electric field variations in an electromagnetic wave [Carcione, 2007].

This means that the techniques and concepts used to understand acoustic waves and electromagnetic waves could be applied to each other. The aim of this thesis is to reproduce some of the advances made with GPR and apply them to sonar technology.

For the particular case of far-field GPR with applications to planar layered media, Lambot et al. [2004] proposed a radar equation in frequency domain that accounts for all antenna effects through frequency-dependent global reflection and transmission coefficients, but also for wave propagation in layered media through 3-D Green's functions. This integrated antenna–medium model relies on the assumption that the spatial distribution of the backscattered field locally tends to a plane wave over the antenna aperture in far-field conditions [Lambot and André, 2014].

By adapting the approaches proposed by Lambot et al. [2004] for GPR and those proposed by Lopera et al. [2007] for landmine detection, it is possible to optimize the processing of sonar signals to locate and even identify buried objects. This method relies on filtering out parasitic reflections and retrieving the radar transfer functions.

When a signal is measured by sonar, it could be modeled by a transfer equation inspired by techniques used in GPR. The equation, for the case of the GPR, is expressed as follows [Lambot et al., 2004]:

$$S(\omega) = H_i(\omega) + \frac{H(\omega)G(\omega)}{1 - H_f(\omega)G(\omega)}, \tag{2.21}$$

with ω being the angular frequency and where:

- $S(\omega)$ is the signal measured by the GPR in frequency,
- $H_i(\omega)$ corresponds to the internal reflections of the transducer,
- $H(\omega)$ represents the emission-reception transfer function of the transducer,
- $H_f(\omega)$ models the multiple reflections between the transducer and the ground,
- $G(\omega)$ is the acoustic Green's function, describing the propagation of waves in the ground.

To improve the signal, it is important to characterize the different transfer functions. This can be done in two steps:

1. **Measurement of $H_i(\omega)$:** This transfer function, representing the internal reflections of the transducer, can be obtained by performing free space measurements, without any obstacle in front of the transducer.
2. **Measurement of $H(\omega)$ and $H_f(\omega)$:** To isolate these functions, measurements are made above a reflective surface, such as a metal plate in the case of electromagnetic waves or, for compression waves, a water-air interface (see Section 4.1.2).

Next, to extract the ground response and eliminate parasitic effects of the transducer, the following equation is used (from (2.21)) to retrieve a measured Green's function:

$$G^*(\omega) = \frac{S(\omega) - H_i(\omega)}{H(\omega) + S(\omega)H_f(\omega) - H_i(\omega)H_f(\omega)}, \tag{2.22}$$

where $G^*(\omega)$ is the filtered transfer function, corresponding to the response of the ground without parasitic reflections. This equation eliminates the internal reflections of the transducer.

Once the signal filtered from the antenna effects is recovered, it must be filtered again to remove the effects caused by multiple surface reflections (between the antenna and the ground). To achieve this, a computed Green's function describing wave propagation between the antenna (located in the air) and the ground surface must be subtracted from the radar signal as proposed by Lopera et al. [2007]. To compute this function, a few parameters must be determined using an inversion method. These parameters may be the antenna height or the dielectric permittivity of the soil surface. The inversion problem is formulated in the least-squares sense, and the objective function is accordingly defined as follows:

$$\phi(\mathbf{b}) = \sum_{i=1}^{N} \left| G^*_{\text{obs},i} - G^*_{\text{mod},i}(\mathbf{b}) \right|^2, \tag{2.23}$$

where:

- $\mathbf{b}$ is the vector of parameters to estimate (e.g., antenna height, soil surface dielectric permittivity),
- $G^*_{\text{obs},i}$ is the observed Green's function,
- $G^*_{\text{mod},i}(\mathbf{b})$ is the simulated Green's function.

Once these parameters are determined, it becomes possible to compute a synthetic Green's function and subtract it from the filtered data ($G^*(\omega)$). We have now the signal without the internal reflections of the system and additionally without the ground reflection. By using migration techniques to reconstruct the reflecting structure present in the subsurface and by focusing the reflections back to the true position of the object, it is then possible to determine the depth at which the object is buried.

2.6 Mine Countermeasures (MCMs)

As mining technology progresses, MCMs have evolved to become more sophisticated and advanced. They are equipped with detection technologies applicable to various domains, such as optics, acoustics, and electromagnetism [Cong et al., 2021]. Today, naval forces employ a variety of strategies for mine detection and neutralization, with the aim of minimizing human involvement in dangerous underwater operations. This shift toward reducing human risk has led to the use of AUV, Remotely Operated Vehicles (ROV), and Underwater Surface Vehicles (USV) within MCMs units [Cui, 2018]. These vehicles are often equipped with sensors and are capable of autonomously performing missions with high precision, thus improving the complexity and effectiveness of MCMs [Sun et al., 2021].

The many types of sonar used in underwater exploration are designed to meet relatively specific and varied operational requirements. The choice of frequency, high or low, depends on factors such as the target's position relative to the seabed and its size. High-frequency devices offer higher resolution, making them suitable for detecting small objects or mapping detailed features of the seabed. However, low-frequency devices are better suited to detecting larger objects or targets buried deeper or shallower in the seabed, because of the greater penetration of the waves. The following is a non-exhaustive list of all sonar types used for underwater exploration.

2.6.1 Single-beam echo sounder (SBES)

It is a long-standing invention, since studies involving the use of SBES or Single-Beam Sonar (SBS) were already being carried out when interest in ocean excavations began, as in the case of the sinking of the Titanic in 1912 [Wölfl et al., 2019]. Nevertheless, its use is still very much alive today, thanks to numerous technological upgrades. The SBES is responsible for the discovery of 18% of the world's ocean floor [Mayer et al., 2018]. SBSs incorporate piezoelectric transducers based on crystals or ceramics that can send and receive acoustic signals. By calculating the travel time of the acoustic wave and knowing the speed at which it travels, it is possible to determine the depth of the seabed [Mayer, 2006].

This part on SBS/SBES will not be further detailed here, as it is the subject of an entire section (Section 3.1) later in this work.

2.6.2 Multi-beam echo sounder (MBES)

The multi-beam echo sounder (MBES) represents a major advancement in underwater mapping. Unlike single-beam sonar, which emits a single beam to measure depth, the MBES emits multiple beams simultaneously, covering a wide swath of the seafloor.

This capability allows it to capture information over a large area, significantly improving the accuracy and efficiency of bathymetry surveys. Bathymetry is the study and measurement of ocean depths and underwater topography [Dierssen and Theberge, 2020] as in the case of Figure 2.3. To capture data from deeper ocean regions, low-frequency beams, often below 20 kHz, are used because they attenuate slowly, allowing for greater reach. However, MBES systems mounted on submersibles, which generally operate at higher frequencies, achieve higher resolution with a smaller coverage area due to shorter ranges and smaller "footprints" on the seabed, despite the rapid decay of high-frequency signals in seawater. This setup makes high-resolution surveys feasible, even at shallow depths. The success of MBES surveys also relies on post-survey data processing, which includes adjusting for sound speed profiles, detecting anomalies, and stitching overlapping swaths [Sun et al., 2021] [Violante, 2020].

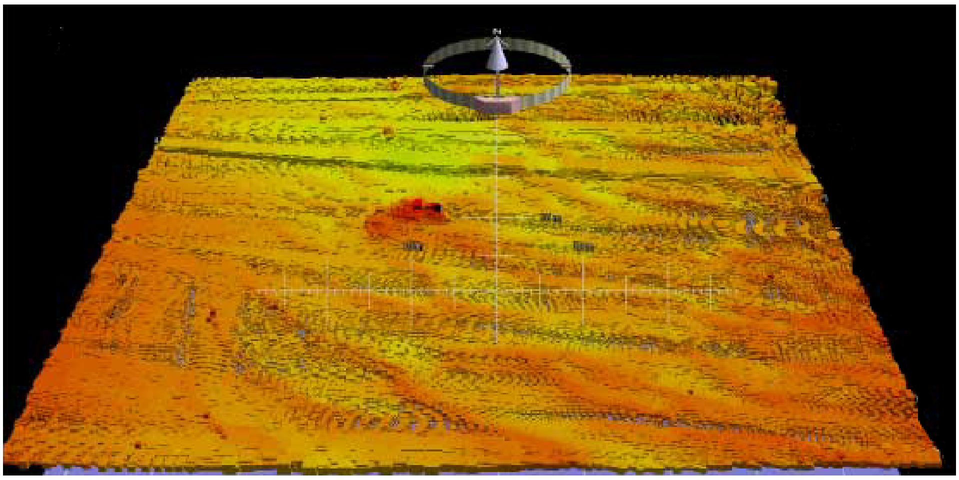

Figure 2.3: Raw MBES data that are color-coded according to depth (hot colors are shallower). From [Calder and Mayer, 2003]

Technically, the MBES system comprises two orthogonally mounted linear acoustic arrays, allowing a narrow beam to illuminate a corridor along the path of the ship. During the same time, multiple receiving channels with beams spaced at varying angles along the track capture data, generating a series of narrow footprints. Within each footprint, the system estimates the slant range to the seabed and measures the backscatter intensity, producing a detailed bathymetric and seafloor backscatter map [Hughes Clarke, 2018].

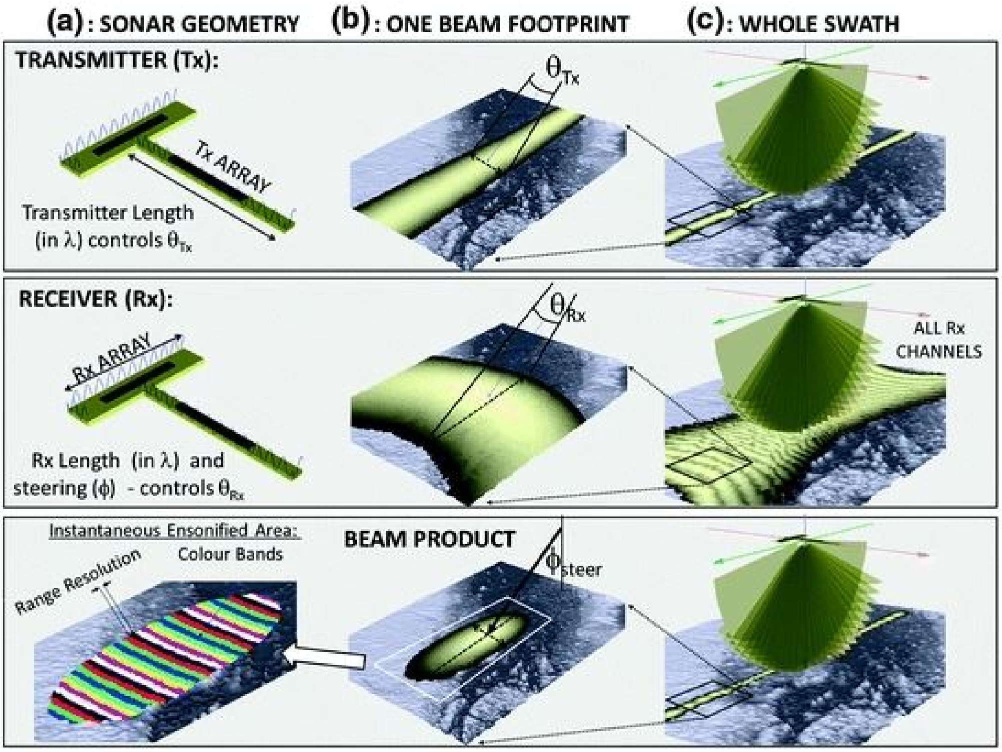

Figure 2.4: Illustration of sonar geometry, followed by an illustration of a single transmitted beam and, finally, a presentation of the many beams transmitted and received by a multi-beam sonar from [Hughes Clarke, 2018]

2.6.3 Sub-bottom profiler (SBP)

The sub-bottom profiler (SBP) is an advanced acoustic technology for mapping the underlying layers of the seabed, obtaining high-resolution profiles of (generally shallow) geological formations. This device is widely used in geological, geophysical, geotechnical, and archaeological studies due to its effectiveness in representing the structure and spatial distribution of submarine strata [Gutowski et al., 2002] [Wu et al., 2021].

Often, when SBP are used, they are also referred to as chirp sub-bottom profilers, which operate by emitting wide-band (see Appendix A for more details about this concept) acoustic signals, often between 1 and 24 kHz. A chirp sounder scans a continuous range of frequencies using chirp signals (signals whose frequency changes over time), from the lowest to the highest (see Figure B.1), unlike traditional sensors, which use a single frequency value. This frequency sweep (chirp) produces a controlled source signature, optimizing signal-to-noise ratio and image quality. Due to these features, chirp profilers offer vertical resolution up to a decimeter, allowing a detailed analysis of the composition and physical properties of underwater layers [Bull et al., 2005].

Sub-bottom sonar is based on principles involving acoustic impedance. Longitudinal waves are sent through the sediments, generating reflected echoes at each soil interface encountered. These signals are picked up by a transducer and stored, allowing successive geological layers of the seabed to be visualized in real time, until the sound energy fades [Wu et al., 2021]. In addition to its application in deep waters, sub-bottom sonar is also useful for detecting objects buried in shallow waters, such as archaeological remains, allowing fine prospecting in shallow environments [Plets et al., 2009].

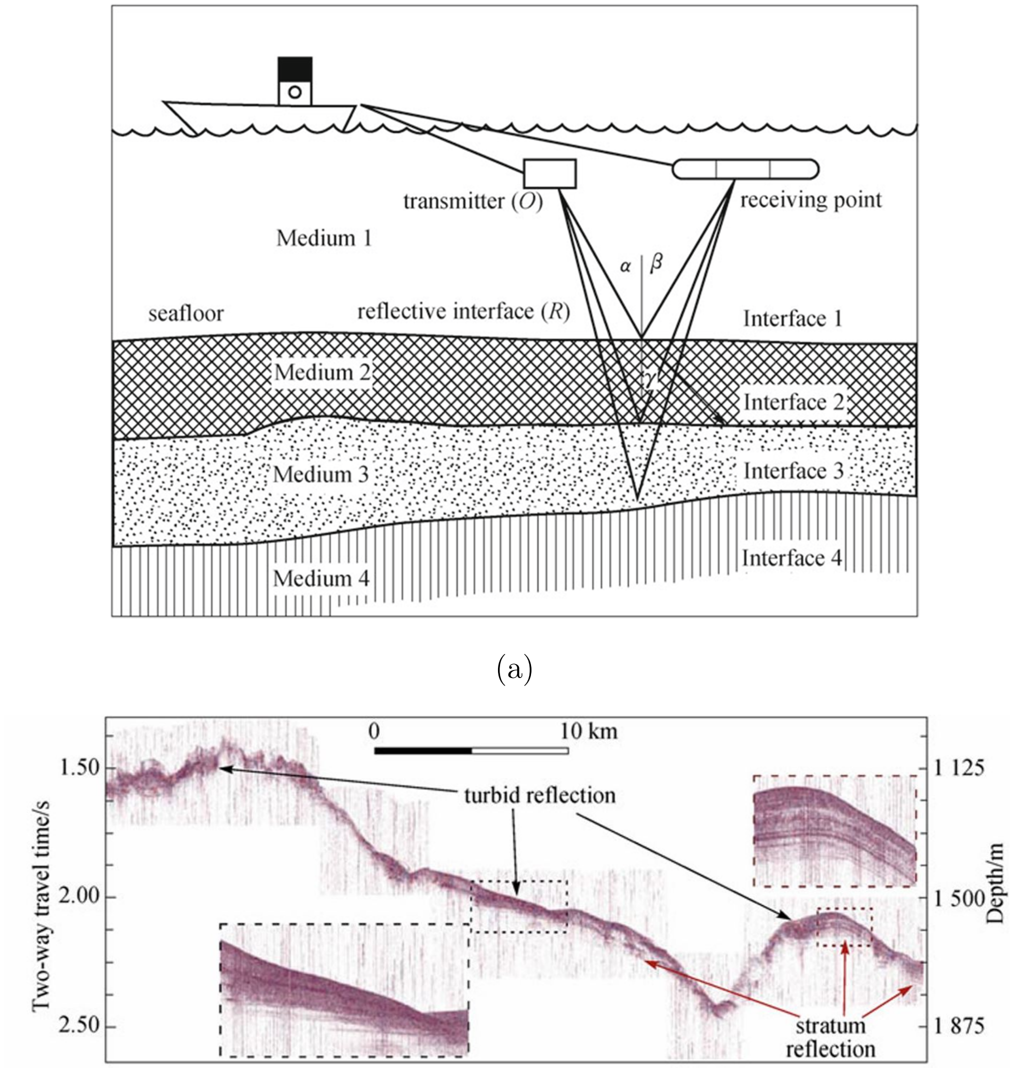

(a)

(b)

Figure 2.5: (a) Illustration of how a Sub-Bottom Profiler works to provide the detection of different underwater lithological layers. (b) Image taken by a SBP. Both from [Wu et al., 2021].

2.6.4 Side-scan sonar (SSS)

Side-Scan Sonar (SSS) was designed to obtain high-resolution images of the seabed, this time capturing variations within this seabed rather than depth data. SSS sonar uses an acoustic backscattering technique to represent the seabed substrate, interpreting differences in echo intensity as a function of the nature and roughness of the surface ([Violante, 2020] [Sun et al., 2021].

SSS systems comprise two transducers installed on a towed probe, often called a tow-fish, each emitting a beam of acoustic pulses directed to either side, port and starboard. The configuration of the beams, narrow horizontally but wide vertically, enables them to cover the entire measurement band along the sonar trajectory [Violante, 2020] [Huff, 1993]. However, a shadow effect persists below the device, forming a narrow band (called nadir) with no data directly beneath the probe [Rajapan et al., 2022].

Reflected sounds vary in intensity according to the composition of the seabed, with hard or uneven substrates producing stronger echoes than relatively smooth or deeper surfaces. This contrast allows for qualitative interpretation of the geological nature and micro-topography of the seabed [Sun et al., 2021] [Violante, 2020]. In some cases, higher frequencies, generally between 400 and 1200 kHz, are preferred for the precise detection of objects, such as wrecks, for example, because they improve image resolution by capturing mainly the surface layer of the marine substrate [Rajapan et al., 2022].

SSS devices are divided into two categories: ship-mounted systems, which use transducers installed on the sides of the hull, and towed systems, which can be deployed at different heights. The Vessel-mounted systems operate at lower frequencies (less than 10 kHz), offering wide coverage and greater efficiency for large areas. In contrast, towed systems, when placed close to the seabed, offer higher resolution for more detailed and higher frequency surveys, although their range is smaller [Wu et al., 2021]. The quality of the images obtained also depends on the speed at which the device moves: too high speed during sonar advance between two pulses compromises the system's longitudinal resolution. Consequently, a slow towing speed, generally around 0.2 m/s, is recommended to avoid this phenomenon, especially for surveys requiring high precision [Huff, 1993].

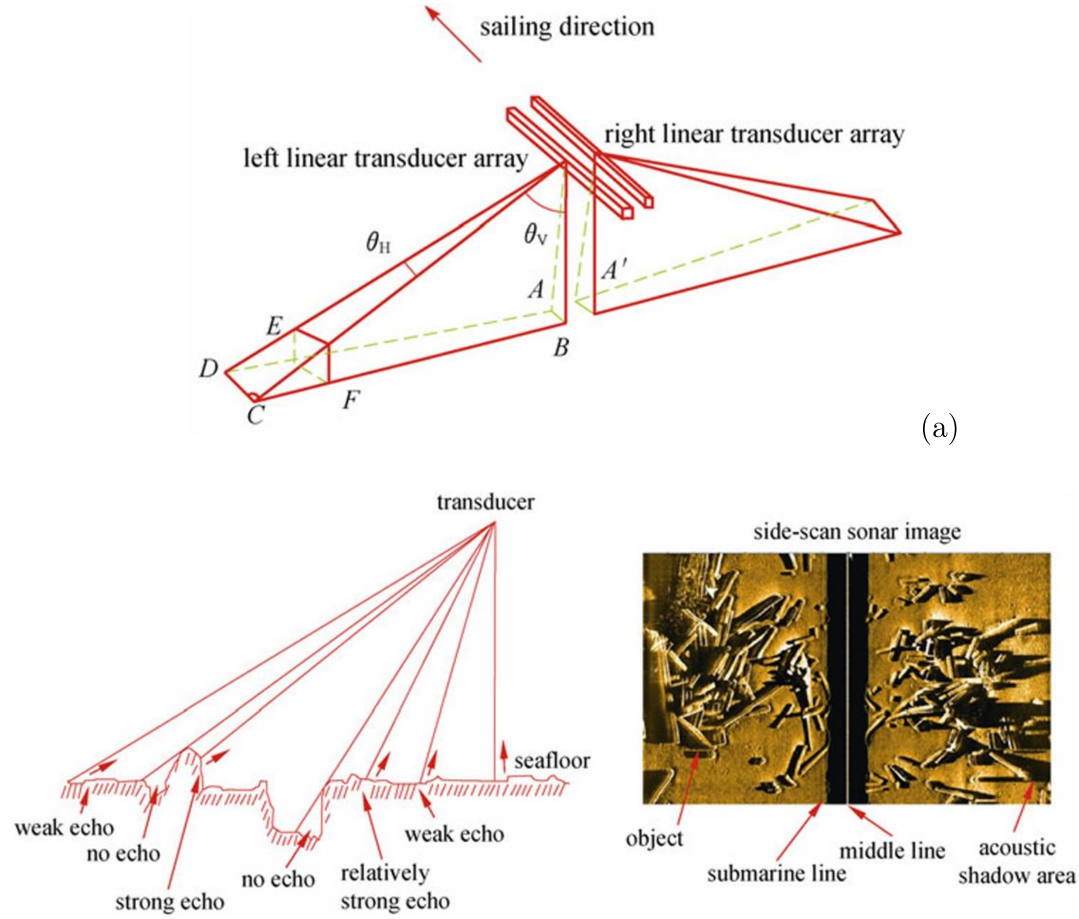

(a)

(b)

Figure 2.6: Principle of operation of the Side-scan sonar (a) with its projection and different opening angles (θ_H and θ_V) and (b) is an example of a recovered image from the device. Both from [Wu et al., 2021].

2.6.5 Synthetic aperture sonar (SAS)

SAS is an underwater imaging technology that surpasses the capabilities of traditional sonar systems by offering centimeter resolution over distances of several hundred meters. Adapted from synthetic aperture radar techniques, which use electromagnetic waves, SAS uses coherent integration of data collected over several transmissions as the sonar moves along its trajectory [Wu et al., 2021] [Marx et al., 2000].

One of the characteristics of SAS is its ability to maintain a constant resolution, regardless of the distance at which the image is captured. This "constant resolution" allows sharp images to be created even at great depths, up to 400 meters, with typical resolutions varying between 10 and 30 cm [Wu et al., 2021] [Hansen et al., 2011]. This technique differs from traditional sonar methods by coherently combining data from multiple pings, resulting in high-quality imaging and improved cross-sectional resolution compared to conventional beamforming systems [Marx et al., 2000]. Unlike conventional SSS, SAS employs a series of multi-element hydrophones. This hybrid approach is the result of advanced backscatter signal processing, enabling precise imaging in large areas [Hayes and Gough, 2009] [Hansen, 2013].

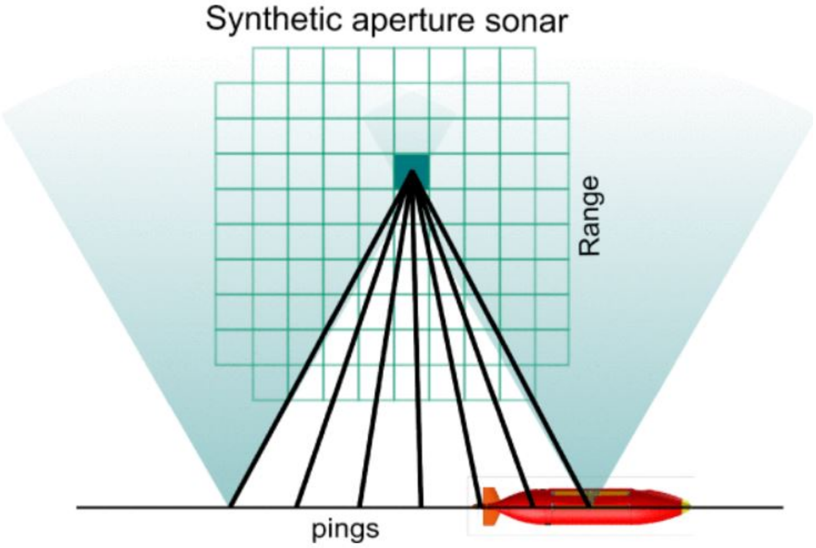

Figure 2.7: Illustration of how SAS works by combining data from several pings. From [Hansen, 2013]

In terms of frequency, SAS offers unique flexibility. High-frequency systems, such as the MUSCLE developed by NURC (300 kHz), provide very high-resolution images, although ambiguities may remain between mine-like objects and natural features. On the other hand, low-frequency SAS (LF-SAS) systems are particularly effective in detecting buried objects, as low-frequency acoustic waves penetrate deeper into the sediment, capturing internal details that are not visible with higher frequencies [Pailhas et al., 2010] [Pan et al., 2016].

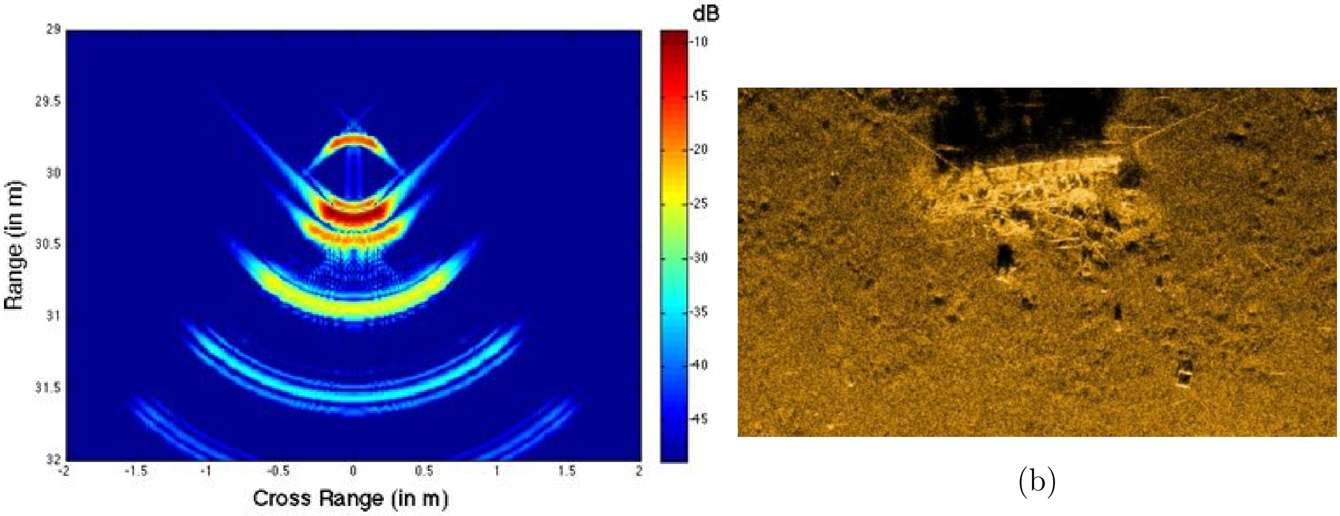

(b)

(a)

Figure 2.8: Both images are based on SAS technology. (a) is a low-frequency image of a PVC spherical shell (Ø: 50 cm) from [Pailhas et al., 2010], and (b) is a higher-resolution, high-frequency image of a shipwreck at 50-m range from [Hansen, 2013].

Chapter 3

Hardware: Ping2 sensor

3.1 Single-beam echo sounder (SBES)

The first echo sounders were used to detect, identify, and quantify fish or biomass in particular. The first experimental trials date back to the 1920s, and the frequencies often used ranged from 12 to 200 kHz, depending on the depth of the water studied [Knudsen, 2009] [Lurton, 2002].

SBESs are, therefore, relatively simple sensors that can be used in a variety of situations. They consist of a transmitting part and a receiving part. The distance measurement is initialized by sending a sinusoidal signal through a power amplifier. This signal is pre-adapted to the target's maximum depth. Once this signal has been reflected, it is converted into an electrical signal. Throughout the process, everything is carefully calculated and timed to avoid the signal from being received just before the projector has finished transmitting. The electrical signal is then processed (to remove unwanted ambient noise) and goes through a gain adjustment to better reflect the different amplitudes with which the return echoes are received. The idea is to be able to amplify signals coming from afar, while a signal that quickly returns to the sensor will be slightly erased.

The equation that allows us to calculate the distance that separates an object from the transducer is the following [Bjørnø et al., 2017] :

$$d = \frac{\tau c}{2}, \tag{3.1}$$

with :

- d is the height or length separating the sensor from the object (in m)
- τ is travel time (round trip) from the signal (in s)
- c is the average speed of sound in water (in m/s)

Having said this, the speed of sound in water is not a constant. In fact, it depends mainly on the density and compressibility of the medium through which it propagates. In the oceans, this density is influenced by static pressure (which increases with depth), temperature, and salinity. To represent this dependence, the speed of sound c can be modeled as a function of three main parameters: temperature T (in degrees Celsius), salinity S (in grams per kilogram or parts per thousand), and depth z (in meters). A simplified relation allowing for the calculation of this speed is given by the following equation [Jensen et al., 2011] :

$$c = 1449.2 + 4.6T - 0.055T^2 + 0.00029T^3 + (1.34 - 0.01T)(S - 35) + 0.016z. \tag{3.2}$$

As already mentioned, the application of such a transducer is varied but can depend on pulse length and effective frequency. In addition, ping duration, ping shape, and beamwidth are parameters that vary the shape of the recovered echo [Ferretti et al., 2015]. This also affects its ability to provide a representation of the seabed. It is easy to see that several intrinsic transducer characteristics can also play a role in object differentiation. Imagine a relatively long signal pulse that covers a distance greater than that between two objects. The two objects would then be detected as a single unit [Bjørnø et al., 2017].

Figure 3.1 shows the trace left by the main lobe of an SBES beam. The sensor first receives the strongest incident signal, followed by a backscatter from the seabed with a more moderate amplitude. This amplitude enables observations to be made about the characteristics of the seabed, such as its roughness or the nature of its coating. It should also be noted that the flatter and smoother the seabed, the better the signal will be reflected.

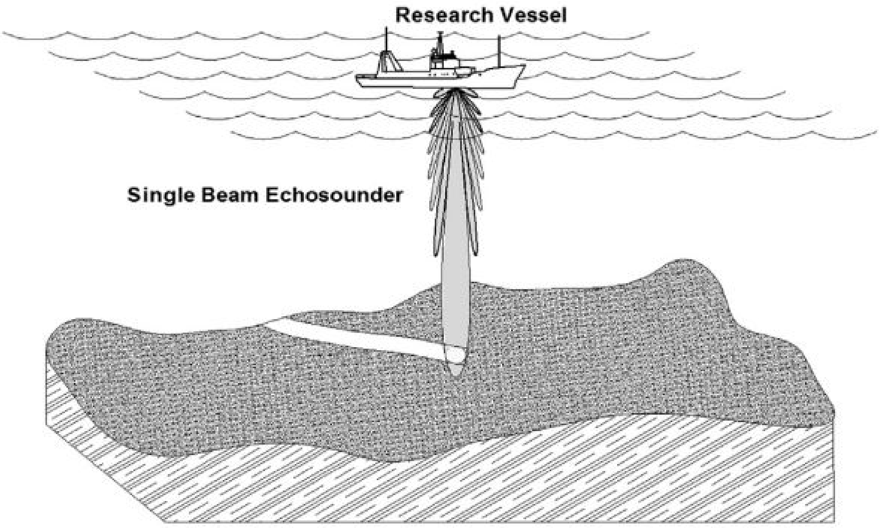

Figure 3.1: Representation of the single beam with its various lobes from an SBES, including the main lobe which reaches the seabed. From [Bjørnø et al., 2017]

3.2 Acoustic scattering

Imagine any object placed in free space and subjected to an acoustic wave. Real materials, whether metals, plastics, or others, deform elastically when subjected to stress, even if this deformation is minimal under the effect of low acoustic pressures [Burnett, 2015].

When the wave reaches the object, it generates an oscillating pressure on its surface, causing the elastic waves to propagate within the object. These internal vibrations are then reflected in the fluctuating pressure on the surrounding water, generating pressure waves that propagate through the water. These waves are called scattered waves or echoes and their intensity varies according to direction [Burnett, 2015].

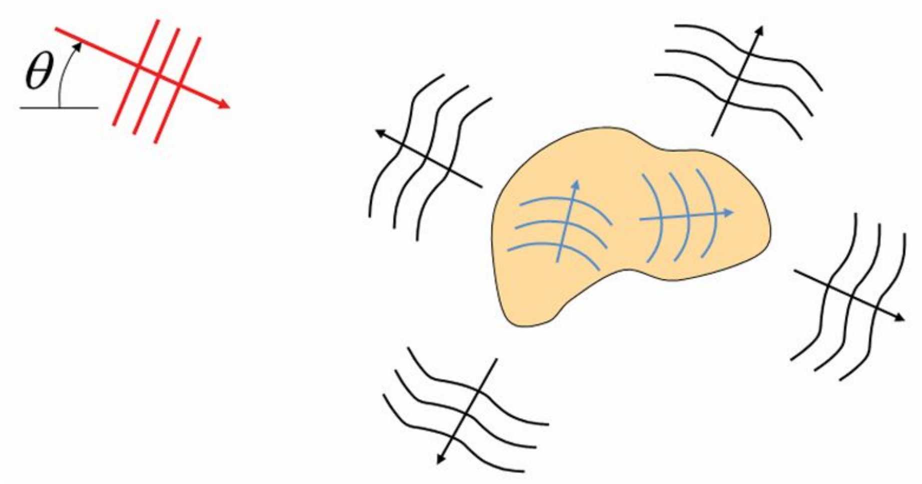

Figure 3.2: Schematic diagram from [Burnett, 2015] of an object immersed in water and struck by a plane wave (red), causing elastic waves within the object (blue), which then re-radiate scattered waves.

In order to visualize more precisely what an echo looks like, Figure 3.3 presents an example and includes both recorded and simulated echoes.

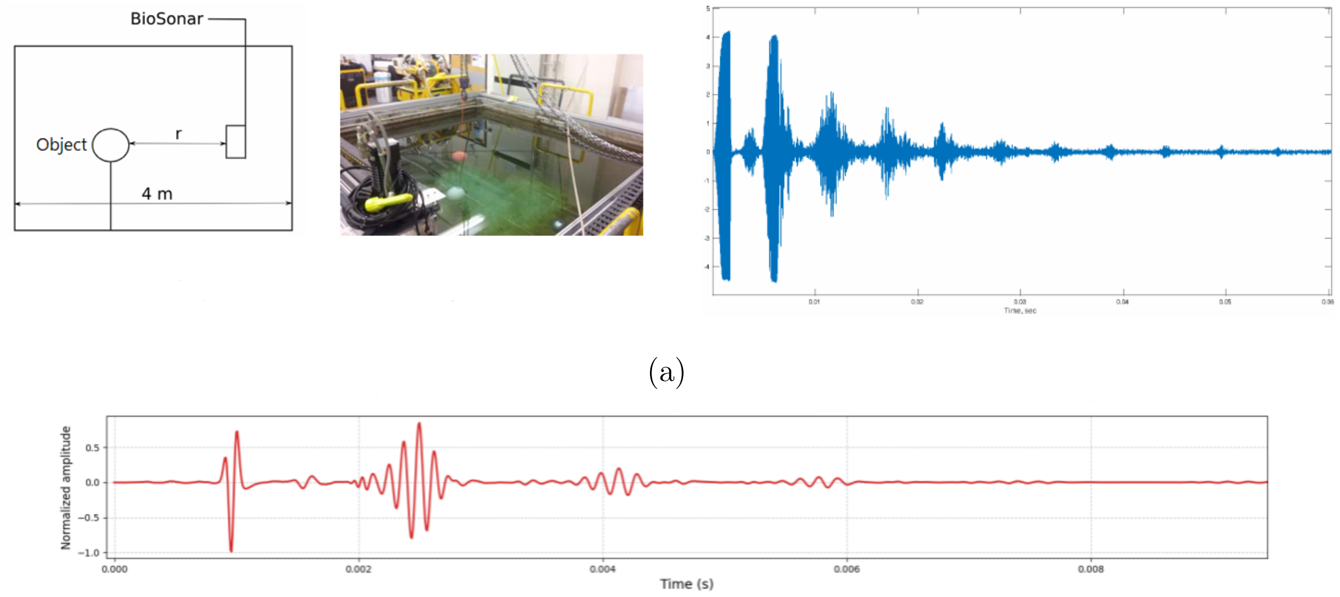

(a)

(b)

Figure 3.3: (a) Example of the echo recorded by a BioSonar in a 3m*4m*2m tank. The echo comes from the walls, bottom of the tank, and other surfaces. From Dmitrieva et al. [2017] (b) Echo of an elastic spherical shell obtained with the Python code developed by Camilo A. Hurtado E. called Acousticscattering.py (not published, private communication) and validated by comparison with the work of Tesei et al. [2008].

To model the interaction between an acoustic wave and an object, early studies were conducted by Rayleigh [1877], who established the theoretical basis for wave scattering. Later, Faran [1951] extended this work to account for elastic spheres. More recently, Kargl et al. [2012] developed an approach based on the scattering of a plane wave in free space. This approach is only valid for simplification purposes in the case of continuous waves that are not characterized by a beginning and an end. When the receiver is positioned far enough from the object, the pressure of the reflected wave can be expressed as follows:

$$p_{\text{scat}}(r) = p_0 f(\hat{r}, \hat{r}_i) \frac{e^{ikr}}{r}, \tag{3.3}$$

where :

- p_0 is the pressure of the incident wave.
- $f(\hat{r}, \hat{r}_i)$ is the scattering amplitude.
- $\hat{r}_i$ and $\hat{r}$ represent the directions of the incident and reflected waves, respectively.
- r is the distance between the object and the receiver.
- k is the wavenumber, which depends on the properties of the medium (here, water).

For simplicity, the frequency dependence of the scattering amplitude is omitted.

In sonar applications, monostatic backscattering is preferred, which occurs when we are interested in the reflected wave that returns directly to the source ($\hat{r} = -\hat{r}_i$). By restricting to this case, the scattering amplitude can be described using a single angular variable, denoted $f(\theta)$.

- For a cylindrical object, θ represents the angle relative to the cylinder's axis, and the amplitude does not depend on the azimuthal angle.
- For a spherical object, the scattering amplitude is independent of both the polar and azimuthal angles, further simplifying the analysis.

The scattering amplitude is often expressed using a dimensionless form function $F(\theta)$:

$$f(\theta) = \frac{a}{2} F(\theta), \tag{3.4}$$

where a is the radius of the object (sphere or cylinder) [Anderson, 1950].

The differential scattering cross-section (measure of an object's efficiency in diffusing, reflecting, or absorbing an incident acoustic wave, depending on its size, shape, and the properties of the surrounding medium [Urick, 1983]) is given by :

$$\sigma = |f(\theta)|^2 = \frac{a^2}{4} |F(\theta)|^2 = \frac{\pi a^2}{4\pi} |F(\theta)|^2. \tag{3.5}$$

The form function $F(\theta)$ describes how the object scatters the acoustic energy as a function of angle and frequency. This allows to connect this expression to the concept of Target Strength (TS).

The vibrations of the object and the resulting scattered waves depend on changes in the frequency of the incident wave, or on variations in the angle of incidence. When a plane wave strikes the object, the intensity of the wave returned in the direction of the source is determined by the TS. The equation most commonly used to measure the expression of the strength of an echo in the far field for a monostatic configuration in dB is the following [Burnett, 2015]:

$$TS(f, \theta) = \lim_{r \to \infty} 20 \log_{10} \left(\frac{r |p(\mathbf{r})|}{r_0 p_0} \right) \tag{3.6}$$

where :

- f : frequency of the incident wave.
- θ : aspect angle of the incident acoustic wave (often the azimuthal angle, which is a horizontal angle relative to the vertical to the ocean bottom).
- $p(\mathbf{r})$: pressure of the scattered wave.
- $||$: indicates magnitude.
- $\mathbf{r}$: position vector from the object to the observer (where TS is measured).
- r : magnitude of the position vector $\mathbf{r}$.
- r_0 : reference distance.
- p_0 : reference pressure.

This introduction to TS is important because it is particularly used in the equation for active sonar detection.

3.2.1 Active sonar equation

There are two types of sonar: active and passive. Passive sonars include only a receiver and no transmitter. The target will only be detected by its ability to emit sound. In active sonar, both a transmitter and a receiver are employed. The system operates on the principle of echolocation (this principle is also used by bats and dolphins) [Ainslie, 2010]. The active sonar equation is used to determine if an active sonar system can detect an echo returned by a target in the underwater environment. The sonar equation for a monostatic configuration (where the transmitter and receiver are co-located) is [Bjørnø et al., 2017]:

$$SL - 2TL + TS - NL + DI \geq DT \tag{3.7}$$

where:

- SL: **Source Level** (in dB) — the intensity of the emitted sonar signal.
- TL: **Transmission Loss** (in dB) — the loss of signal intensity due to propagation (both outbound and return paths).
- TS: **Target Strength** (in dB) — the reflective capability of the target.
- NL: **Noise Level** (in dB) — the ambient noise level in the environment.
- DI: **Directivity Index** (in dB) — the gain from the sonar receiver's ability to focus on the direction of the incoming echo.
- DT: **Detection Threshold** (in dB) — the minimum signal level (power of the acoustic signal received after reflecting off a target) required for detection.

For example :

Suppose a sonar system emits a signal with a source level of 200 dB, experiences a transmission loss of 100 dB (which is the round-trip), with the target strength at 20 dB, the noise level at 40 dB, and the directivity index at 10 dB. Finally, the detection threshold is set at 5 dB.

The sonar equation (3.7) becomes:

$$200 - 100 + 20 - 40 + 10 \geq 5 \tag{3.8}$$

$$90 \geq 5$$

In this case, detection is possible because the signal level is much higher than the detection threshold.

3.3 Introduction to the Ping2 sensor

The Ping2 is an altimeter and single-beam echo sounder (as described in Section 3.1) manufactured by Blue Robotics Inc. This device is a multipurpose underwater sensor that can detect objects up to 100 meters deep. It is a small, compact sensor that can basically be mounted on ROVs and USVs. In most cases, it is used to determine the distance between the surface of the water and the seabed, as well as to detect and avoid obstacles.

3.4 Technical details

The Ping2 operates at a center frequency of 115 kHz and exhibits a -3 dB beam width of 25 degrees. The use of this precise frequency is justified by the fact that it deviates from the usual frequencies found in similar devices. This sensor features a piezoelectric transducer capable of sending an acoustic signal and listening when it returns. Once the response signal has been retrieved, it is possible to view in real time the full echo response from the target, which is plotted directly in an open source application supplied by the manufacturer called "Ping Viewer" (and presented in Section 3.5.1). In addition, it is possible to dialogue with the sensor using a binary message format called the "Ping protocol". This protocol offers the possibility of using customized Python libraries to supply the required data without having to go through the dedicated application.

For its part, the device integrates a relatively powerful "bottom-tracking" algorithm, capable of differentiating between numerous entities by comparing the intensity of the measured signal. For example, the sensor can tell the difference between a seabed a few dozen meters below the surface and a fish passing just below it. In this way, it can differentiate between several echoes.

In terms of dimensions, the sensor is housed in a case with a top diameter of 50 mm and a bottom diameter of 47 mm, for a total height of 41 mm (see Figure 3.4). The upper part is formed by an anodized aluminum-reinforced housing.

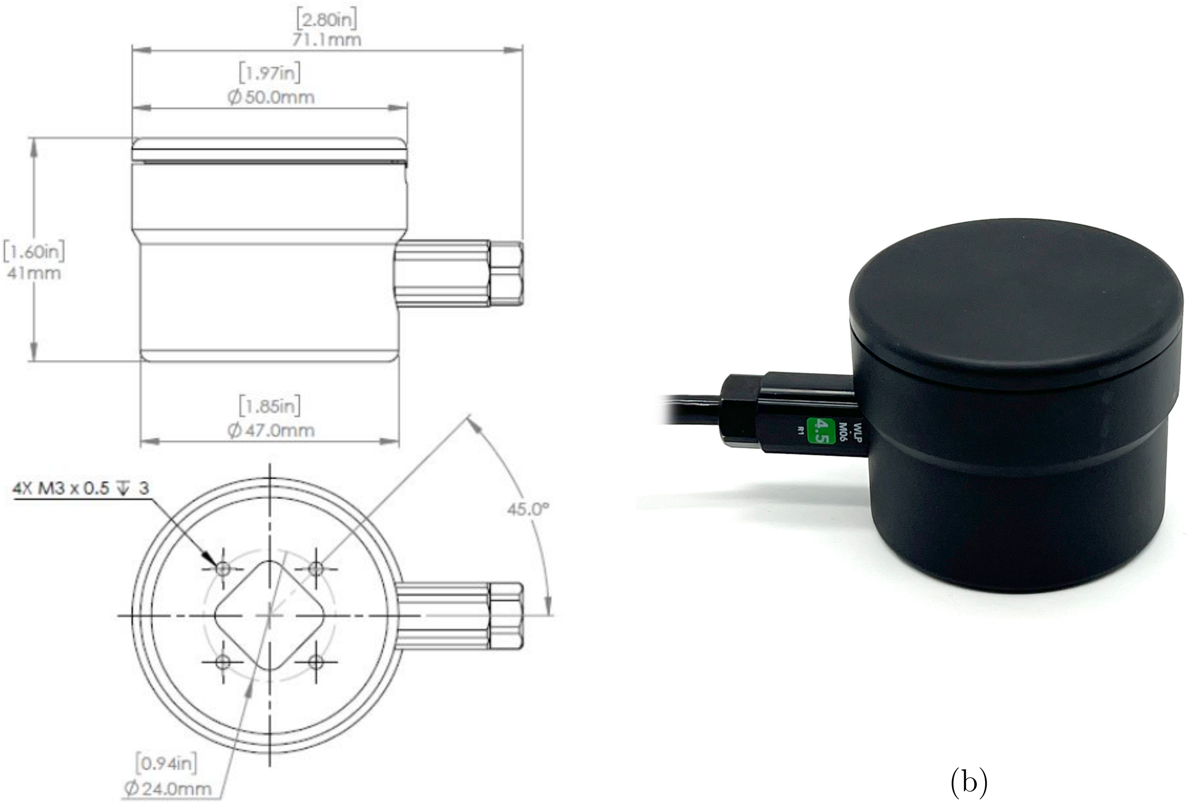

(b)

(a)

Figure 3.4: In (a), presentation of the 2D plans and measurements of the sensor and (b) is a picture of the Ping2. Both from the official website of the manufacturer [Robotics, 2024].

The entire device is powered by a voltage of 4.5 to 5.5 V and features simple 4-wire 24 AWG (0.5106 mm) wiring for both input current, ground connection, and two other wires, Rx (in) and Tx (out). All these wires are wrapped in an 875 mm long, 7 m long waterproof sheath and connected to a serial adapter also offered and sold by Blue Robotics. It is called the "BLUART USB to Serial and RS485 Adapter" and is an open-source circuit board that enables communication via USB with devices using serial UART or RS485, offering various ways of communication, depending on the protocol used.

3.5 Data acquisition

Data acquisition involves measuring a physical quantity (such as pressure) as a voltage, which is then converted into a digital signal. When using Ping2, there are two main ways to retrieve data:

- via the Ping Viewer application
- via the Ping protocol

Both of these solutions to retrieve data all send the same types of request and configuration commands directly to the sensor. The results obtained using either method are the same, although the acquisition format changes. The recovery process for the transducer is the same, and is roughly summarized in Figure B.3 in the Appendix.

3.5.1 Ping Viewer application

Ping Viewer is a graphical user interface to connect, configure, and save data via Ping2. This interface is divided into 4 main compartments. The first is the distance display, the second is the distance axis, the third is the return plot, and finally the last is the waterfall. These 4 aspects are shown in Figure 3.5

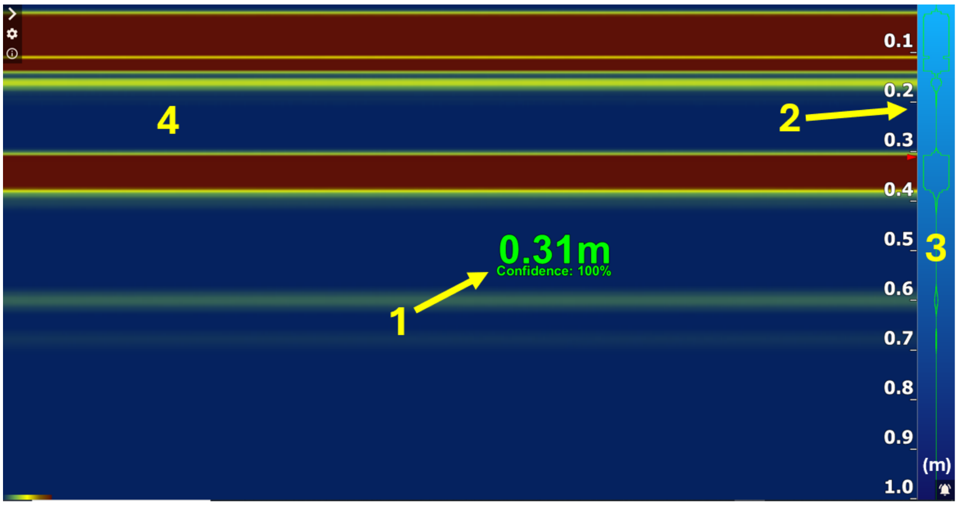

Figure 3.5: Ping Viewer interface for a measured distance of 0.31 m and a confidence of 100%. (1) is the distance reading, (2) is the distance axis (3) is the mirrored return plot and (4) is the plot of the samples called the waterfall.

The distance indicator displays the distance measured to the target based on the most recent reading taken by the transducer. Immediately below, the confidence level of the last sample is indicated in percent and is color-coded. Green indicates 100% confidence (maximum confidence), yellow 50% and red 0% (low confidence). Confidence increases with measurement consistency. It is not a notion based solely on the accuracy of the measured distance. The confidence estimation is determined by comparing the strength of the echo reflected from the bottom (return echo) with the level of ambient background noise (ambient noise floor).

The distance axis is shown on the right-hand side of Figure 3.5. It indicates the distance between the detected interface and the Ping2 sensor. A slight red arrow also locates the most likely position of the surface, which returns the strongest signals. The scale of this axis is automatically adjusted according to the current scanning range of Ping2.

The return graph shows the signal strength as a function of distance. It is a simple plot that shows the intensity of the reflected signal. Stronger signals leave much more pronounced traces. At the top of Figure 3.5, you can see very pronounced traces. These traces can be found throughout all distance measurements (as long as we define the start of the measurement at distance 0) and do not represent anything more than the vibratory signal within the device. In fact, when the Ping device emits the acoustic pulse, it continues to vibrate, like a bell ringing, and this residual energy is captured as a return signal until it dissipates. This phenomenon is comparable to multiple reflections within the transducer, even before the signal leaves the transmitter enclosure. This part of the signal is therefore defined as the *ringing signal* or can also be defined as $H_i(\omega)$ from Equation (2.21).

Finally, the waterfall graph is a display that occupies the main part of the application window. It plots consecutive profile samples (the distance is on the vertical axis, and the color represents the intensity of the signal). The horizontal axis represents the time, although the interval between each measurement is not automatically displayed. In concrete terms, each new ping taken appears on the right edge of the graph, while older data gradually move to the left.

The home screen also offers the ability to configure and change several key parameters: the number of pings emitted per second (ping/s), the speed of sound (m/s), an automatic or adjustable gain value, a scan start distance and a scan end distance. There is no need to go into detail about these parameters, as they're the same as those presented in the following Ping protocol presentation.

3.5.2 Ping protocol

The second way of communicating with the transducer, and surely the one most used for data acquisition in this thesis, is called the Ping protocol. This protocol lists a set of messages that can be requested directly in a Python script to retrieve data performed under the desired conditions.

Customizable commands can be used to request or set the value of a variable. Thus, there are two main commands:

- The set() command: can be used to switch the device to configurable/automatic mode, or to set other parameters such as sound speed, scan length, or gain value.
- The get() command : allows the user to retrieve crucial information such as the distance measured, the confidence with which this distance is measured, and many other variables (such as the Profile_data which is similar to the full waveform).

When it comes to retrieving data, the get() command is one of the most important. Ping2 developers have also collected information in more general messages such as: "myPing.get_profile()". This function, directly recognizable after downloading the manufacturer's library (Ping1D), retrieves the following information in a single operation:

Table 3.1: Parameter sets that can be retrieved using the "myPing.get_profile()" function provided by the Ping1D Python library.

Name	**Description**	**Units**
Distance	The current return distance determined for the most recent acoustic measurement.	mm
Confidence	Confidence in the most recent range measurement.	%
Transmit_duration	The acoustic pulse length during acoustic transmission/activation.	µs
Ping_number	The pulse/measurement count since boot.	/
Scan_start	The beginning of the scan region in mm from the transducer.	mm
Scan_length	The length of the scan region.	mm
Gain_setting	The current gain setting. 0=0.6; 1=1.8; 2=5.5; 3=12.9; 4=30.2; 5=66.1; 6=144	/
Profile_data_length	The length of the proceeding vector field, always equal to 200	/
Profile_data	An array of return strength measurements taken at regular intervals across the scan region. The first element is the closest measurement to the sensor, and the last element is the farthest measurement in the scanned range.	/

An example of a custom Python code used to perform the experimental measurements is provided in the Appendix C. This code allows retrieving all the useful information in a ".csv" format. Using such a code also allows to directly decode the 8-bit data provided by the sensor into a set of integer numbers (in the form of a list) which can then be displayed graphically. This is the Profile_data shown in Table 3.1.

3.6 Data manipulation

Once the data are recovered, the list of the return signal strength values can be formatted. Understanding the nature of these data is essential in the case of the Ping2 sensor, as it faces certain technical limitations that will be discussed in the following section (see Section 3.7).

Before making the graphs of our return values. The x- and y-axes have to be specified.

- Measurement of the return strength (Y-axis) :

Return strength is a variable set directly by the manufacturer as the signal amplitude over an interval from 0 to 255 (no units and no decimals). This value is set by hardware and cannot be changed by the user.

- Time interval (X-axis) :

The time interval must be adjusted according to each type of profile because it depends on a number of parameters, such as the length of the scan or the speed of sound in water. This interval can be calculated as follows:

$$\Delta t_s = \frac{\text{scan\_length}}{\text{profile\_data\_length} \cdot v_s}, \tag{3.9}$$

with v_s, the speed of sound (mm/s), the profile_data_length that corresponds to the vector field of the measurement, and finally, the scan_length that corresponds to the length of the scan (can be set depending on the part of the signal we are interested in).

Figure 3.6 helps to better understand how these different parameters come into play and influence the list of return strength values of the received signal. The figure therefore refers to a profile for an estimated distance. The notion of scan_start and scan_end are well represented to understand how the scan_length is constructed (these 3 variables can therefore be controlled by the user). The sensor will always manage to dissect the scan_length into a vector of 200 samples because this value is locked by the hardware part of the data recovery command (although in the case of Figure 3.6 it is equal to 24 to simplify the understanding of the image).

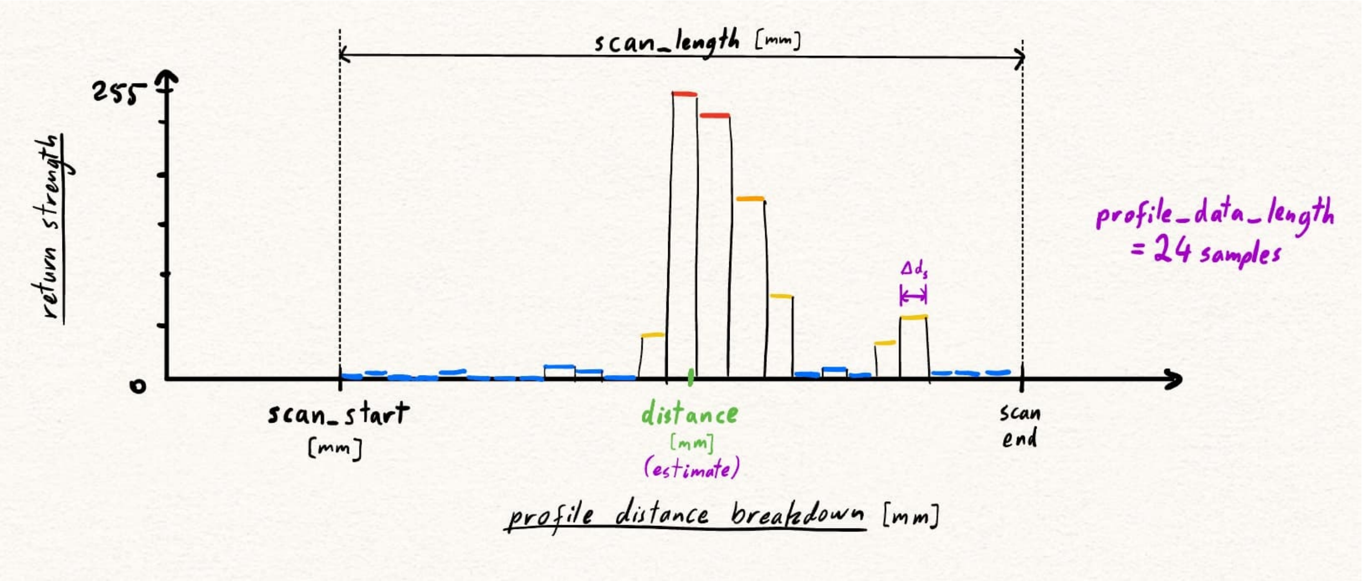

Figure 3.6: Explanatory graph of the different notions involved in shaping the distance profile values from [BlueRobotics Community, 2023].

Figure 3.7 allows visualization of the graph obtained after defining the different axes. The graph is separated into two parts (the first in red and the second in green). The first value to reach saturation (255) in the second part of the signal is the one corresponding to the maximum of the return force found on the path traveled by the signal. The distance from the surface causing this return strength is the one shown to the user. A straightforward step to verify the accuracy of the sensor's distance estimation involves recalculating the distance using known parameters, such as the speed of sound in water and the time taken by the sensor to detect the reflected surface (saturation peak). For this case, the time to reach the saturation peak is approximately $t = 0.32\,\text{ms}$. Given that the speed of sound in water for this profile is $c = 1400\,\text{m/s}$, the recalculated distance can be obtained using the formula:

$$d = c \cdot t$$

Substituting the values, it becomes:

$$d = 1400 \cdot 0.32 = 448\,\text{mm}.$$

This result closely matches the sensor's estimated distance of 445 mm, confirming the consistency of the measurement. The use of a sound speed of 1400 m/s in water is not an arbitrary choice. Indeed, it is only when this value is used during the sensor's measurements that the distance estimated by the sensor matches the distance manually measured with a tape measure. This means that 1400 m/s is the sound speed in water that provides accurate estimates under these conditions during this thesis. This value can be explained by a relatively cold water temperature (around 10 degrees), a very low salinity since the water used is tap water, and also by the fact that the transducer is working at shallow depths.

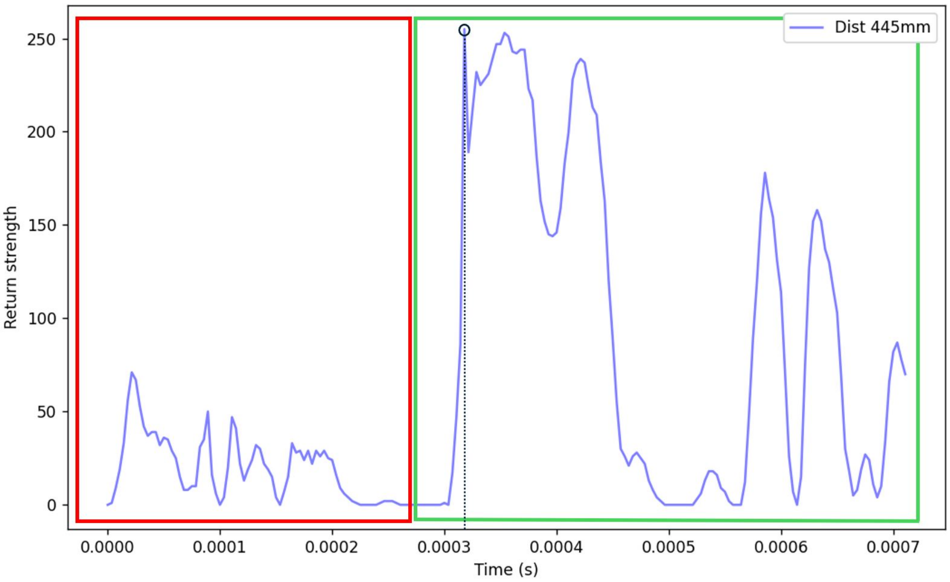

Figure 3.7: Graph of the profile data for a distance of 445 mm with a speed of sound in the water of 1400 m/s, a gain value of 5 and a scan_length of 1000 mm. Red part is the *ringing signal* and green part is the return echo information. The highest value, surrounded by a little blue circle, corresponds to the reflection of the detected surface.

3.7 Notes and limitations

The Ping2 sensor provides profile data derived from measurements taken by its Analog-to-Digital Converter (ADC). However, the information available and transmitted by the sensor is not the raw data collected by the ADC. Before being transmitted, these data undergo processing steps that include filtering, gain adjustments, and the addition of an offset (to ensure that any background noise in the data is appropriately adjusted or offset, so that the detected signal accurately represents the echo returned from the target). It is not possible to directly access the raw ADC values, which initially measure the intensity of the returned acoustic echoes. An other important point to note is that the ADC samples are at a much higher frequency than the rate at which the profile data are transmitted. This discrepancy creates technical constraints: on one hand, the bandwidth of the serial communication channel is too limited to transmit ADC data in real time at full resolution. On the other hand, the microcontroller's memory is insufficient to store all the data from a complete high-resolution transmission.

The sensor measures the amplitude of the reflected signal, but this measurement is adjusted by internal algorithms and does not represent the exact power of the signal reflected by the target. That is why the measurements provided by the sensor do not allow a direct measurement of the acoustic backscattering. However, it is possible to extract data from the processed profiles (these are the ".csv" files that contain the profile data). The information transmitted by the sensor is specifically designed to represent the response strength of emitted acoustic signals and not to provide raw acoustic measurements. In practice, the sensor captures the vibrations of the transducer via the

ADC, which are then processed to be transformed into a single measurement per profile point. The intensity data returned by the sensor are somewhat based on voltage measurements. However, no calibrated conversion is available to relate these values to a precise physical unit (such as pressure). This limitation comes from the use of custom transducers and the complexity of the amplification circuits, which makes the theoretical estimates unreliable.

The part that returns the strongest signal will prevail. In most measurements taken, the "target tracking" algorithm aims to target the surface or object placed in front of it. Generally, the smoother the surface, the better it will reflect the incident wave. In all cases, the device will adjust the signal to the target and always return a saturated peak, reaching the maximum return strength value (255). This capability also has its drawbacks, as the entire signal is scaled to the distance it was reflected from, applying an automatic gain that is difficult to recover (in addition to the user-applied gain). This aspect of Ping2 will be thoroughly discussed in Section 4.1.1. This automatic setting complicates the comparison between measurements, as the amplitude of the recovered signal is not really proportional to the distance at which a surface is detected. Currently, the selling company has not developed any support to recover the raw, unprocessed values.

Finally, temperature compensation is not integrated into the sensor. Therefore, the value of the speed of sound propagation in water is not accurate. However, by making our own distance estimates directly from the response profiles, it appears that there is a discrepancy between the measured distances and the estimated distances. We therefore agreed that a sound speed in water of 1400 m/s was the best estimate of reality, as said previously. In addition to this limitation related to the speed of sound in water, there is the duration of transmission of the signal, which is always fixed by the transducer at a value of 26 µs and cannot be directly changed by the user. This reduces the resolution of the signal, as a higher value would have allowed better visualization of the variations in the received signal. This is because a longer signal duration increases the signal-to-noise ratio, making it easier to distinguish the useful signal from ambient noise.

Chapter 4

Methodology

4.1 Laboratory experiments

This section reports on laboratory experiments and is divided into 3 parts. The first part is dedicated to acquisition of the gain function, the second to the notion of a perfect acoustic reflector (PAR), which is important in the sensor calibration stage, and finally, the last section is dedicated to the recovery of scenarios involving different experimental configurations. In all of the scenarios presented here, the same infrastructure has been used and all the measurements in this section were taken between October 14 and December 13, 2024, in the GERU Hall at the Université catholique de Louvain, Belgium.

The Ping2 single-beam echo sounder (see Section 3.3) is mounted on a mechanical arm with three-dimensional mobility (see Figure 4.1). The mechanical arm is set in motion by three MAC800 motors, controlled remotely from a computer with a Matlab script. This allows the arm to move freely along the x, y, and z axes. The x-y-z positioning system is adjustable, allowing its position to be set relatively and moves at a speed of 0.15 m/s. At the beginning and end of the movement, there is a phase of acceleration and deceleration. The exact value of the acceleration speed is not known.

The transducer, positioned so as to face the bottom, is immersed in a one-cubic-meter plastic tank (high-density polyethylene (HDPE)) reinforced by a metal skeleton and mounted on a wooden pallet to increase its stability. The bottom of the tank is padded with Plexiglas plates to make the bottom of the tank smoother and more uniform. The echo sounder provided numerous pings that were captured using the configuration just described, with the bottom at different distances from the transducer and the gain also set to avoid over-saturated signals as much as possible.

For each ping, measurements were meticulously taken to ensure that the distance was always greater than that required to remain in a far-field configuration. Given a transducer diameter of 50 mm and a Ping2 wavelength ($\lambda = \frac{v}{f} = \frac{1400\,\mathrm{m/s}}{115\,\mathrm{kHz}} \approx 0.0122$ m) at a maximum water sound velocity of $v = 1400\,\mathrm{m/s}$, the far-field distance is reached at approximately:

$$\text{Far-field distance} = \frac{D^2}{\lambda} \approx \frac{(50\,\mathrm{mm})^2}{\lambda} \approx 20.54\,\mathrm{cm},$$

where D is the diameter of the transducer and λ is the wavelength of the sound beam. In any case, this distance will never be approached, as the transducer's minimum effective detection distance is 30 cm. Below this, the information returned is not accurate.

(a) (b)

Figure 4.1: (a) is the experimental setup involving the mechanical arm and the one-cubic-meter tank. (b) is the Ping 2 sensor mounted at the end of the arm and looking straight down at the tank bottom.

In order to retrieve the raw data from the transmitter/receiver via the Ping protocol or the Ping Viewer application, the transducer is connected to a laptop with the following configuration: Intel(R) Core(TM) i7-7700HQ CPU, 2.80GHz, 2.81 GHz, 16 GB RAM. The connection between the two components is ensured by a USB to TTL serial adapter also produced by Blue Robotics.

4.1.1 Gain function and theoretical background

The gain function, denoted as $g(t)$, plays an important role in modeling the response of the transducer as a function of time t. This function provides a concrete understanding of how the gain evolves and reflects the sensitivity of the transducer to a given excitation. Various cases can be considered for $g(t)$, each corresponding to a specific behavior, and a non-exhaustive list is provided below:

- **Constant case:** when $g(t) = a$, the gain is constant and does not depend on time. This represents a stable system where the response remains the same regardless of the duration.
- **Linear case:** when $g(t) = a \cdot t$, the gain increases proportionally with time as the amplification increases progressively.
- **Nonlinear case:** when $g(t) = a \cdot t^b$, the gain depends non-linearly on time. Growth can be faster depending on the value of the factor b ($b > 1$) or slower ($0 < b < 1$) than linear progression.
- **Exponential case:** when $g(t) = e^t$, the gain follows exponential growth. In this case, the response becomes rapidly very large over time.

Thus, these few forms presented of $g(t)$ provide some flexibility for understanding and interpreting the collected data.

The gain function applied to the Ping2 transducer and echo sounder is quite difficult to retrieve, as these data are not provided directly by the manufacturer. Given that only the experimental measurements are available, it can be reconstructed using an inverse modeling approach. It is possible to define the term "inverse modeling" as follows: it is a process of extracting information from measurements of the physical quantities associated with the acoustic field. It should be noted that this model may be an inaccurate representation of a real scenario, especially since the experimental data itself may be distorted by noise [Bjørnø et al., 2017]. It is important to clarify that even though, in some ways, the data profiles contain information about the physical processes that govern the propagation of the acoustic signal, these data are only stored as digital amplitudes, which do not refer directly to well-known physical units (see Section 3.7).

To recover the gain applied to the signal, start with this equation:

$$s_{\mathrm{g}}(t) = s(t) \cdot g(t), \tag{4.1}$$

where, $s_{\mathrm{g}}(t)$ is the signal received by the transducer, $s(t)$ is the ideal raw signal received by the echo sounder, $g(t)$ is the applied gain.

To experimentally attempt to recover the gain applied to the entire data set, a relatively large distance interval was set. This was arbitrarily chosen, while avoiding excessively short lengths to limit possible reflections due to the size of the water tank used. Thus, measurements were taken over a distance range of 400 to 700 mm. These distances are those that separate the sensor head from the bottom of the tank.

It is necessary to specify that these measurements were taken manually using a measuring tape and are not those returned by the transducer (429 to 715 mm). Indeed, because of the sensor's geometry, it seems that there is a systematic offset from 15 to 30 millimeters, suggesting that the distance is not calculated from the emitting surface but from a virtual origin within the sensor. This offset can vary according to the speed of sound in water, although the one and only value for sound in water used during the measurements was deliberately set at 1400 m/s.

In the case of Ping2, at least two types of gain come into play. The first is a gain that can be configured manually and can take six different values. These values are listed in Table 3.1. The second is an automatic gain, independent of the experimenter's control, which relies on an algorithmic process to detect the target.

The following steps explain the method used to try to recover the applied function of gain :

- Begin by defining a reference signal, which should be the shortest distance measured by the sensor (429 mm), from a set of distances.
- Select any other signal of interest.
- Identify, for both signals, a notable and recurring point in the upper part of the *ringing signal*. This notable point will serve as a threshold. Two thresholds are therefore defined, one for each of our signals (reference signal and signal of interest).
- For each of the two signals, retrieve only the values that exceed their respective threshold and keep only the values located in the part of the *ringing signal*.

- Divide the filtered values of the signal of interest by the filtered values of the reference signal from the previous step. This step allows to obtain the ratio between these two signals. From Equation (4.1):
$$\frac{s_{g_1}(t)}{s_{g_2}(t)} = \frac{s_1(t) \cdot g_1(t)}{s_2(t) \cdot g_2(t)} = \frac{g_1(t)}{g_2(t)} \quad \text{with } s_1(t) = s_2(t)$$
- Once the ratio of these values is obtained, fit a linear model (assuming that the gain follows a linear adjustment over time).

All the values that will be presented were obtained using the Ping communication protocol, carefully ensuring that the user-adjustable gain was locked at 5. The scan length is set to its minimum value of 1000 mm to provide the best possible resolution at this distance. The speed of sound in water is set to 1400 m/s. Furthermore, only the values that returned a confidence of 100% were selected to represent the interval.

4.1.2 Concept of the perfect acoustic reflector (PAR)

In order to retrieve the full-wave sonar equation discussed in section 2.5, it is important to recover certain transfer functions specific to sonar. These transfer functions are denoted as $H_i(\omega)$, $H(\omega)$, and $H_s(\omega)$, following Equation (2.21). These functions can be determined during the calibration step of the transmitting device on what is called a Perfect Electromagnetic Conductor (PEC) [Lopera et al., 2007] [Sluÿters et al., 2024]. In the specific case of acoustics, the PEC is converted to a PAR.

When an acoustic wave passes from a medium with a high sound speed, such as water, to a medium where the sound speed is significantly lower, such as air, the interface between these two media acts almost entirely as a near-perfect acoustic reflector. This phenomenon is explained by the marked differences between the acoustic impedance of the two media, with the specific acoustic impedance given by the following equation [Pierce, 2019] :

$$Z = \frac{\rho c}{\cos\theta},$$

where ρ represents the density, c the speed of sound and θ the angle of incidence of the wave.

For the air-water interface, the ratios

$$\frac{(\rho c)_{\text{air}}}{(\rho c)_{\text{water}}} \approx 0.0003 \quad \text{and} \quad \left(\frac{c_{\text{air}}}{c_{\text{water}}}\right)^2 \approx 0.05$$

show that the impedance of air is negligible compared to that of water. The interface thus behaves as a pressure-release surface, reflecting nearly all of the incoming acoustic energy.

According to Brekhovskikh and Lysanov [2006], at normal incidence ($\theta = 0$), the reflection coefficient V in Equation (2.15) approaches -1, which means that the reflected wave is almost equal in amplitude but opposite in phase to the incident wave. In fact, taking the values $\rho = 1000\,\text{kg/m}^3$, $c = 1400\,\text{m/s}$, $\rho_1 = 1.2\,\text{kg/m}^3$, and $c_1 = 343\,\text{m/s}$ in Equation (2.15) and considering that the wave strikes the surface normally (i.e., the angle to the normal is 0), the value of the reflection coefficient is $R \approx -0.9994$. This approximation applies not only to the air-water interface, but also to any system where the ρc value of the second medium is negligible compared to that of the first. In contrast, when a wave is incident from air onto water, the acoustic properties of the interface cause a significant increase in the acoustic pressure in the transmitted medium.

To retrieve valid data for calibration in the PAR configuration, the same experimental setup as the one of the gain function acquisition was used with one difference. In fact, the transducer is no longer positioned to face the bottom of the tank, but rather to face upward toward the top of the tank, namely the water-air interface (as shown in Figure 4.2).

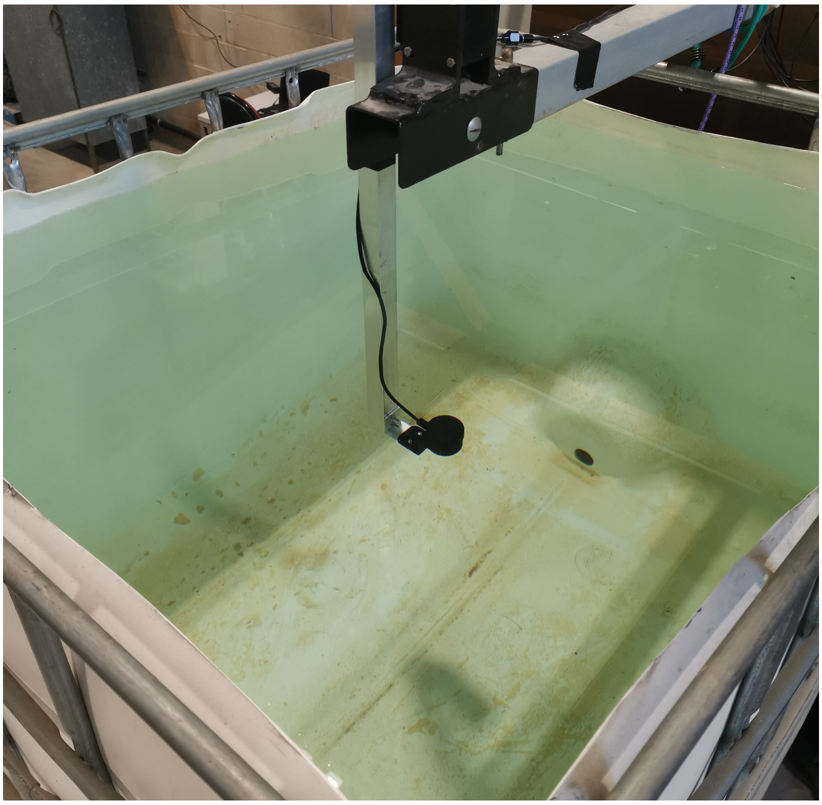

Figure 4.2: Experimental setup for collecting profile data at different distances with the sensor facing upwards towards the PAR surface.

Several distance profiles were recovered, all carefully performed with a user-adjustable gain of 5, a scan length locked at its minimal value of 1000 mm. The use of a gain of 5 allows for visualization of the entire signal without too much saturation compared to lower gain values.

4.1.3 B-scan scenarios

For this part of the experiment, B-scans of several configurations were conducted. The main goal was to display different types of reflected surfaces, varying sediment heights, and also incorporate the concept of a target.

A B-scan in GPR involves moving the antenna along a straight path over the surface of interest while recording the reflected signals at different points. The data collected at each position is called an A-scan, representing the intensity of the reflected signal at that specific point. In the case of this experiment, the B-scan also involves a sonar sensor that moves along a trajectory to recover the echo at different positions. The A-scan, on the other hand, is comparable to a single signal studied as a function of time. The Ping Viewer application emphasizes temporality and evolution, while the B-scan focuses on a fixed spatial view. In a way, Ping Viewer offers a dynamic, time-evolving perspective, while the B-scan provides a snapshot of the spatial distribution at a given moment. Therefore, for the remainder of this study, the B-scan is preferred.

To perform the B-scans, the Matlab script controlling the movement of the mechanical arm was modified to create 80 cm long segments all at an initial height of 45 cm. The y- and z- coordinates were fixed, allowing movement only along the x-axis. This movement always occurred from right to left (that is, in the negative x-direction, see Figure 4.1).

B-scan measurements are taken in one go, including the acceleration and deceleration phases of the movement for a total of 90 pings. The sensor does not stop at each distance interval, as this would require a significant amount of time for the various tested scenarios, as well as for other reasons that will be stated in the discussion chapter. However, this motion is not uniform and includes both acceleration at the beginning and deceleration at the end of the path. These phases have an impact on the measurements because they do not allow to recover the time interval between each of the 90 pings taken over the 80 cm traveled. Thus, ping 1 corresponds to the measurement taken for x = 0 cm and ping 90 corresponds to a distance of x = 80 cm. However, since the time elapsed between each ping is not the same, a decision was made to present the results based on the ping rather than the distance traveled.

For the various configurations selected, the first is the standard configuration described in Section 4.1. Then sand was added (see the technical details of the sand in Figure B.2). This sand was added at different heights, starting with 1.5 cm without including a target. Next, different targets were used and sand was added from 1.5 to 2.5 cm and finally 4 cm high (still including the Plexiglas layer). The final height was used to almost completely cover the target. The two types of targets used are described in Figure 4.3. It consists of a concrete brick, a stone with irregular sides, and a 3D-printed mine. This mine resembles a Manta model, with its shape recreated using polylactic acid (PLA) filaments on a PRUSA i3 MK3 printer (see Figure 4.4), and its design is inspired by a related document [Chu, 2009]. Unfortunately, the 3D printed Manta mine could not be used because its density was slightly too low to prevent it from sinking, even though it was filled with various types of ballast.

Figure 4.3: Targets used for the B-scans sections. On the left, an irregularly-shaped rock approximately 3.5 centimeters high and 7 centimeters long, in the middle, a 4*10*12 cm concrete brick, and on the right, a 3D-printed Manta mine with 4 centimeters high, with a large diameter of 10 centimeters and a small diameter of 4 centimeters.

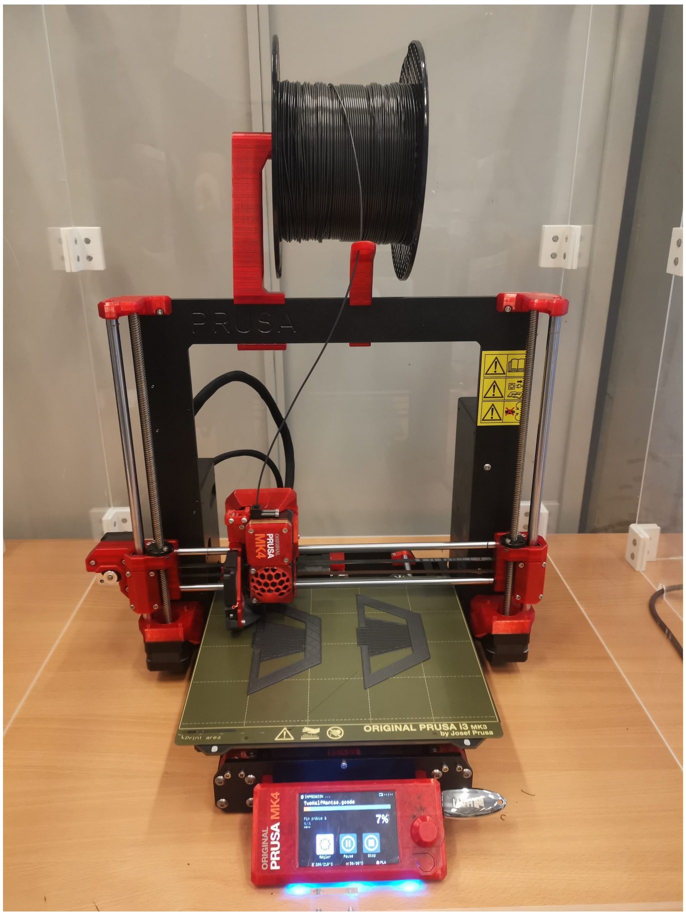

Figure 4.4: Photo taken during the 3D printing of a Manta mine on a PRUSA i3 MK3 printer.

Pictures showing some of the configurations used are shown in Figure 4.5. When targets were used, they were always placed directly below the movement path of the sonar to facilitate detection. To avoid any intrinsic variation in the results obtained, the sensor values are locked and are the same for all measurements. The value of the speed of sound in water is 1400 m/s, the scan length is adjusted to its minimum value of 1000 mm, and the user-adjustable gain is locked at 5, to provide data that are consistent with and comparable to that provided in the previous sections.

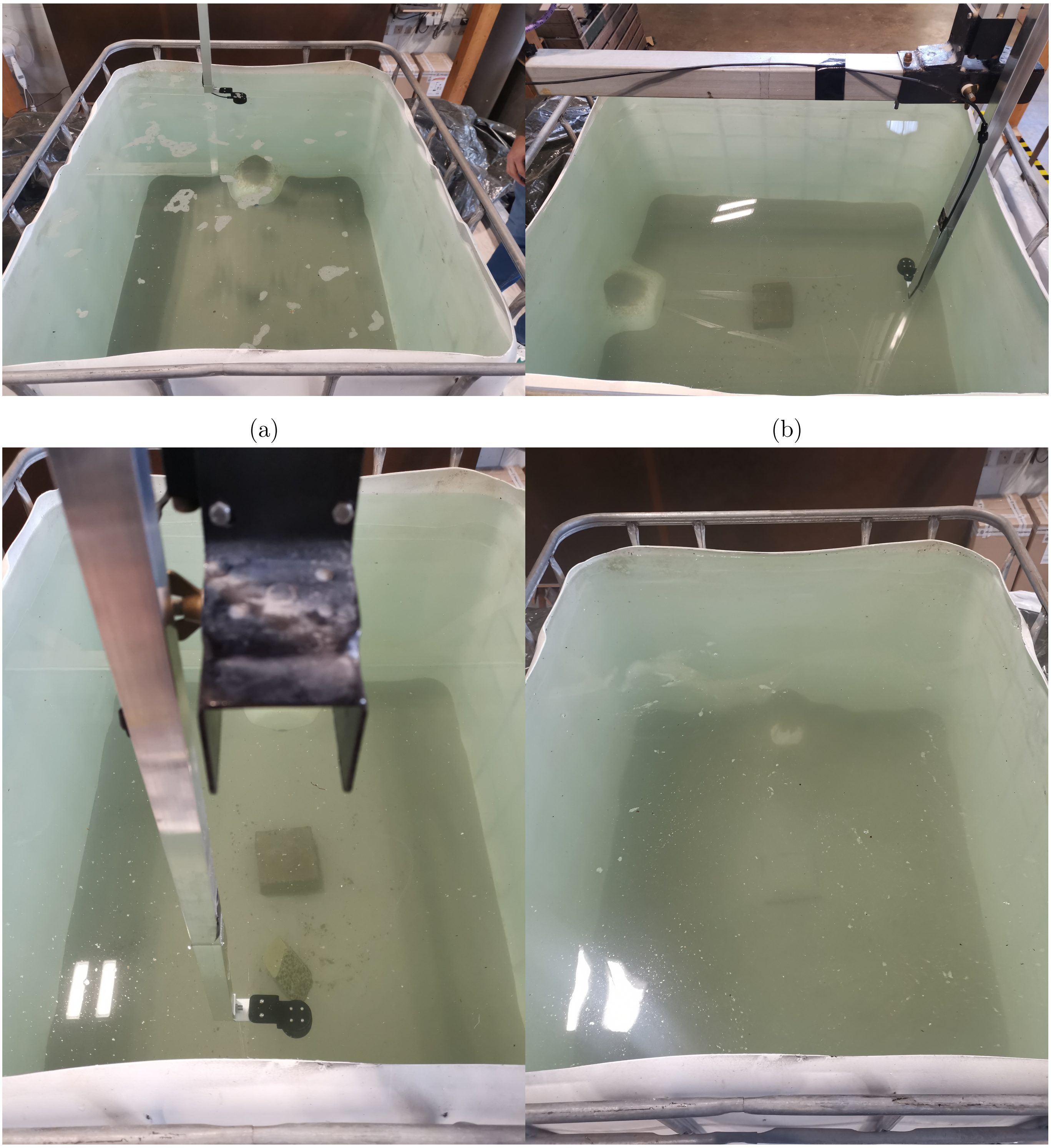

(a) (b)

(c) (d)

Figure 4.5: (a) Experimental setup including a 1.5 cm layer of sand. (b) Insertion of a concrete block as a target, still with 1.5 cm of sand. (c) Concrete brick embedded in 2.5 cm of sand with a rock placed on the sand's surface. (d) Concrete block almost buried under 4 cm of sand.

4.2 K-wave numerical simulations (MatLab)

The k-wave simulation package is an open source toolbox for simulating the propagation of ultrasound and acoustic waves in realistic environments. These time-domain simulations are based on a pseudospectral k-space method that supports various sources and detection surfaces. However, this package is limited because it does not allow the inclusion of diverse targets. Only so do layers with different parameters. The k-wave package has a well-detailed user guide, part of which serves as an inspiration for this section [Treeby and Cox, 2024].

An acoustic wave traveling through a pressurized medium generates numerous changes within it. These different variations (in pressure, velocity, or any other physical parameter) can be simplified by a series of first-order differential equations using the k-wave library. The simulation package therefore offers various functions capable of solving these series of equations in different dimensions, namely :

- kspaceFirstOrfer1D
- kspaceFirstOrder2D
- kspaceFirstOrder3D

These functions are relatively simple to use and allow one to introduce a very special notion called perfectly matched layer, or PML. This layer roughly absorbs the acoustic waves that arrive at the edge of the simulation domain and can therefore simulate an infinite domain beyond its limits.

There are many useful methods for determining the solution of differential equations. These methods depend on quite a few factors, such as the size of the computational domain and the properties of the medium. The method used in this case is the pseudospectral (PS) method, which is a numerical technique that solves differential equations by decomposing more complicated solutions into series of smooth global functions. This results in greater precision and faster reduction in the error rate [Fornberg and Sloan, 1994]. They also solve the problem of memory capacity and the number of time steps required in well-known simulations using finite-difference methods. Nevertheless, the simulations remain of a relatively high order of magnitude and require substantial resources. This is why optimized CPU codes for compressional waves were used to reduce the computation time by a factor of 6 to 10.

Note that these first-order functions presented previously are only valid for compressional waves, and two other functions are interesting to use when one wishes to add an additional component, namely, a solid layer now involving shear waves in addition to compression waves. These two functions are :

- pstdElastic2D
- pstdElastic3D

The Pseudo-Spectral Time Domain (PSTD) functions require the same configurations as the first-order functions (kspaceFirstOrder1D, kspaceFirstOrder2D and kspaceFirstOrder3D), with a few differences. One of the main differences is that the optimized CPU codes are not applicable for shear waves, limiting the use of these functions to smaller simulations. For this reason, only first-order functions are described in the following.

Before any simulation is carried out, four very important objects need to be defined :

- The computation grid
- The medium properties
- The acoustic source
- The sensor

Simulations use a computational grid. For each dimension (x, y, z), information such as the number of points (N_x, N_y, N_z) and the spacing between them (dx, dy, dz) are specified. The choice of these parameters depends on the size of the domain and the maximum frequency to be modeled. The spatial gradient calculations make strong use of the fast Fourier transform (FFT). The time to compute each FFT can be minimized by choosing the total number of grid points in each direction to be a power of two or to have small prime factors.

In addition, the desired grid size must be increased to include the PML. The use of a PML is of great interest when modeling the behavior of waves in free space. In practice, however, it is more complicated. In fact, using FFTs in the process of calculating spatial gradients implies that the wave field is periodic. This behavior suggests that when a wave disappears as it passes one side of the simulation, it reappears on the other side. It is like imagining a train disappearing into a tunnel on the right of our field of vision, only to emerge immediately to the left of another tunnel on the other side.

To represent this infinite propagation field, increasing the number of grid points in the simulation would be necessary, but this would have a heavy impact on the machine's computing time. To remedy this, the PML is integrated as an absorbing limit, which, once touched, allows the wave to disappear without leaving traces because of anisotropic absorption. This PML can also be included externally, but this is a resource-intensive option.

Implementing such a layer requires two conditions:

- An absorption coefficient high enough to withstand large waves.
- The layer should not reflect waves when touched.

This layer can be configured by assigning a well-defined thickness (units of grid points) or by defining the absorption parameter (units of Nepers $\cdot s^{-1}$).

The medium is defined by setting physical properties such as the *speed of sound* and the *density* of the material. These properties can be constant (homogeneous medium) or spatially varying (heterogeneous medium). For example, a varying speed of sound can be specified to model interfaces or layers with different acoustic properties.

Acoustic sources are defined by specifying an initial pressure or introducing a particle velocity source. For example, in some simulations, a source can be modeled as an initial pressure distribution shaped like a disk, with characteristics such as the position, radius, and amplitude of the source being defined. This is specified in terms of both acoustic pressure and velocity.

The sensors are modeled by indicating the positions on the grid where the pressure or velocity values of the particles are recorded. The choice of sensor location can significantly influence the accuracy of recorded data and, consequently, the overall quality of simulation results. Note that the library does not propose a monostatic source and receiver position by default, but it is possible to align their positioning to create a similar structure.

Concerning the numerical model stability, it is also possible to control the precision and performance of the simulation by adjusting key parameters. One of the most critical parameters is the Courant-Friedrichs-Lewy (CFL) number, which determines the time step size based on the maximum propagation speed in the medium. The CFL number is calculated as:

$$CFL = \frac{c_0 \cdot \mathit{\Delta} t}{\mathit{\Delta} x},$$

where c_0 is the speed of sound, Δt is the time step and Δx is the spatial resolution.

Maintaining an appropriate CFL number ensures the stability of the numerical model, as a time step too large can lead to unstable simulations where numerical errors grow exponentially and explode [De Moura and Kubrusly, 2013].

Thus, the stability and accuracy of the model depend on three main factors:

- The discrete equations must be consistent with the equations governing the physical phenomena.
- The numerical model must be stable, which means that numerical errors should not amplify over time.
- The numerical solution should be accurate, converging to the continuous solution as the spatial and temporal discretizations become finer.

By selecting the CFL number, it is possible to balance computational performance with the need for accurate and stable results. For instance, reducing the time step size (i.e., lowering the CFL number) may improve stability but increase computational cost. This is why a certain balance must be struck when simulating a new situation.

4.2.1 Green's function

The purpose of this section is to explain the methodology adopted to simulate results that can later be used with the experimentally collected data to get the transfer functions of the sensor and attempt to remove the effects caused by the sonar-hydrophone.

Referring to Section 2.5, to recover the transfer functions of our sonar-hydrophone-multilayered medium system, it is precisely important to determine the Green's function for the 3D elastic wave propagation in a multilayered medium. "Green's function is a powerful mathematical tool for solving all kinds of differential equation problem. It was first introduced by George Green in 1828 and it enables to understand how a linear system responds to a point perturbation signal (Dirac's mass) in a specific mathematical context" [Hoernig, 2010].

However, after much research in the literature, the analytical determination of such a function proved too complicated to establish, so it was decided to simulate it with numerical tools, such as the k-wave Matlab package. This is why undergoing this numerical simulation step would allow the generation of numerical results comparable to the experimental results, enabling the calibration of the sensor.

The simulation of the Green's function was set to respect the same configuration adopted when recovering experimental data involving a PAR (see Section 4.1.2) by using a supercomputer made available by the Université catholique de Louvain. The computational system used in this study is a PowerEdge T640 Server, optimized for high-performance tasks. It features an Intel® Xeon® Gold 5118 processor (12 cores, 24 threads, 2.3 GHz) and 64 GB of RAM (8 x 8 GB, 2667 MT/s). Storage includes a 300 GB 15K SAS drive for the operating system and two 2 TB 7.2K RPM drives in RAID 1 for data redundancy.

The code of the simulation capable of giving the Green's function using a PAR configuration (see Section 4.1.2) can be found in Appendix C.

Two main configurations with an 8-centimeter difference were implemented. The choice to begin detecting the water-air interface at 30 centimeters from the sensor is explained by the fact that this is the shortest detection distance for the sensor under real-world conditions. The second distance of 38 centimeters was arbitrarily set, as optimal calibration requires multiple measurements at different distances from the water-air interface. As mentioned above, to initiate a simulation, four important aspects must be determined: the grid, the properties of the layers, the source, and the receiver. For each of the two configurations, these parameters are relatively similar.

The computational grid was set to conform to a size that is a power of two. A grid of 512×256×256 mm was thus simulated. Given that the Ping2 sensor has a beam angle of 25°, it is not necessary to simulate a grid with excessively large values in y- or z-dimensions. Inside this grid, the monostatic sensor and the interface are separated by the desired distance. With a uniform grid spacing of 1 mm in all three dimensions (dx, dy, dz), they are positioned 300 grid points apart in the case of the 30 cm simulation, and 380 grid points for the one of 38 cm.

For the choice of layers used, the primary propagation domain of the waves is water. To achieve this, the density is set to 1000 kg/m^3, and the speed of sound propagation in water is set to 1400 m/s (similar to the real situation) throughout the grid. Only the values corresponding to the air layer were modified to set the wave propagation speed at 343 m/s and the density at 1.2 kg/m^3. Figure 4.6 refers to the density and wave velocity within the computational grid for the simulation case at 30 cm.

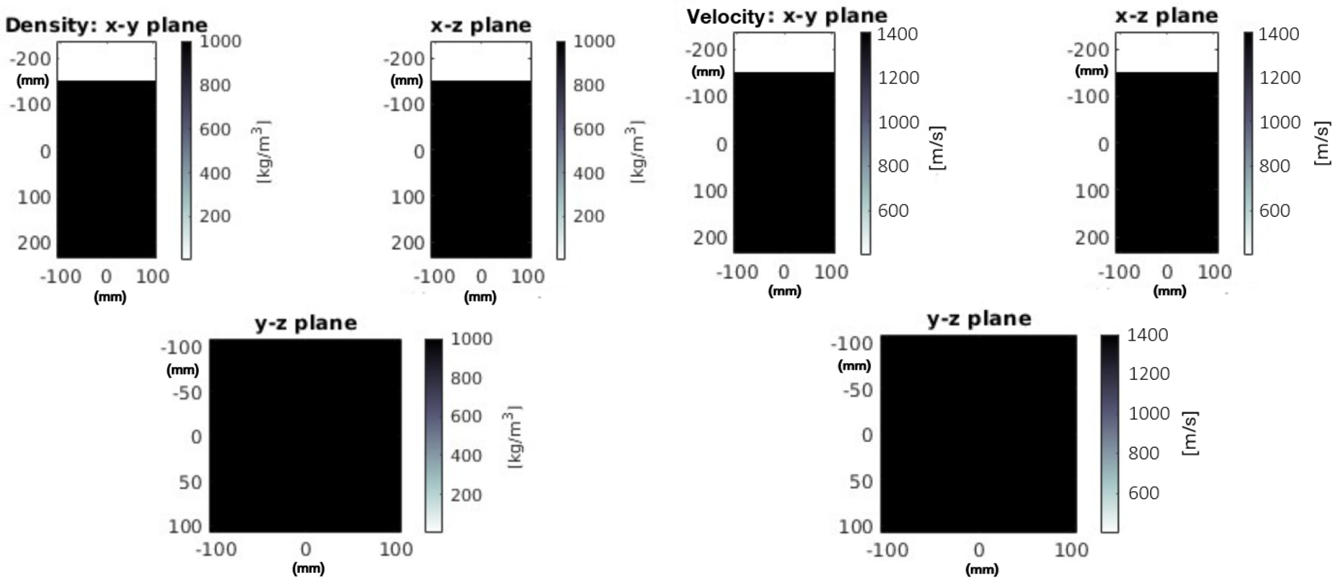

(a)

(b)

Figure 4.6: Density (a) and velocity (b) grids for the simulated layers in the case of a perfect acoustic reflector for a 512*256*256 mm grid.

The source, as previously mentioned, is a crucial aspect to simulate in order to approximate real-life situations. The k-wave library provides the ability to implement a point source which can be configured using two main parameters. The first is the magnitude, and the second is the radius of the source. The magnitude is set in Pascals (Pa) and is defined by the following equation given by [Urick, 1983]:

$$\mathrm{SL} = 10 \log \frac{\text{source intensity}}{\text{intensity of reference}}, \tag{4.2}$$

where, SL is the Source Level in dB.

Based on the information provided by the manufacturer of the Ping2 sensor, which states that the SL for the reference intensity of one µPa at 1 meter is 198 dB, the calculated magnitude (source intensity) is 7943 Pa (see Figure 4.7). As for the radius, it is specified in terms of the grid spacing (which is the same in all three dimensions). A radius of 25 is used to simulate a sphere with a 5 cm diameter, capable of mimicking the sensor in use. Finally, the sensor is defined as a unitary collection point and is placed in the exact center of the source.

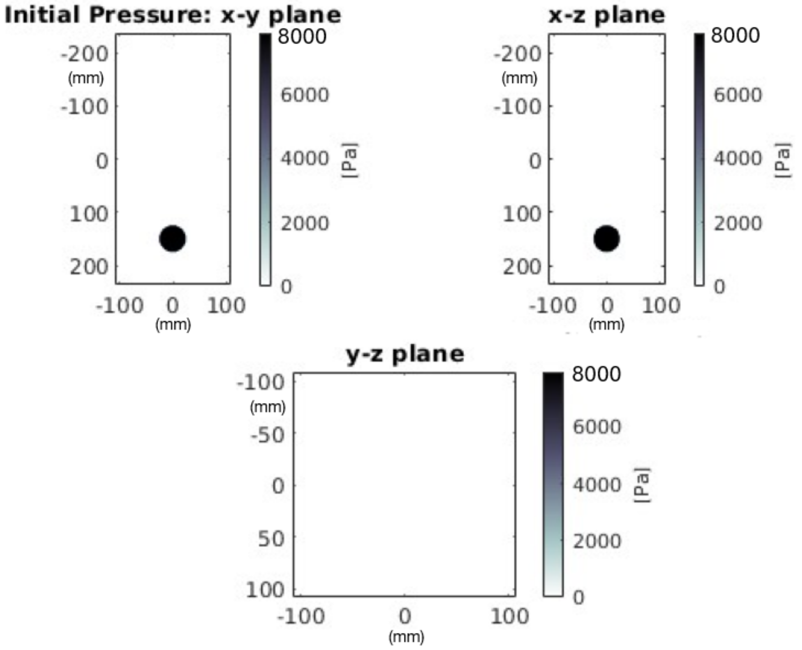

Figure 4.7: Initial pressure conditions of the simulation in the case of a perfect acoustic reflector (30 cm apart from the source) for a 512*256*256 mm grid.

The configuration for 38 cm is identical in every aspect, except for the position of the interface and the source/receiver, which are spaced an additional 8 cm apart.

4.2.2 Free field simulations

In order to capture the $H_i(\omega)$ signal presented earlier in Section 2.5, a free field measurement is required. Note that in the model used, there is no physical source and receiver, but it is more an ideal point source and receiver, so that $H_i(\omega)$ accounts for the direct transmission between the two points.

The free field measurement is based on the same configuration as the previous two spacings (30 and 38 cm), but with the water-air interface removed. As a result, the waves encounter only the PML placed at the edges of the simulation and are absorbed. This ensures that only the waves and reflections generated under free field conditions are captured when a signal is emitted. The density and velocity are therefore uniform across the entire simulation surface at 1000 kg/m^3 and 1400 m/s.

4.2.3 Pseudo-spectral time domain simulations

In this part of the experiment, simulations involving a different type of function than those previously studied will be tested. These are the pstdElastic 2D and 3D functions. Unlike the previous ones, these functions implement not only compression waves (P-waves) but also shear waves (S-waves) allowing to introduce a solid layer. Unfortunately, these functions do not benefit from optimized code and only allow for small simulation sizes, on the order of a few centimeters. It is therefore not possible to obtain signals comparable to the configurations encountered in the laboratory, such as those conducted in Section 4.1.3.

Two configurations are tested:

- Simulation of two layers: one of water and one of sand (marine sediments). The source and receiver will also be in a monostatic configuration with an initial pressure of 50 Pa. These values were changed because of the small size of the simulation (the use of such a value helps maintain a balance between spatial resolution and source amplitude. It was set arbitrarily through trial and error until a simulation was achieved that minimizes artifacts from an overly large source). Table 4.1 summarizes the parameters of the different simulated layers, and Figure 4.8 shows the position of these layers within the simulation grid.
- Simulation of three different layers. The first layer (the uppermost) is a water layer. The next layer is intended to mimic the presence of a mine, and finally, the last layer is composed of sand. The aim of simulating a layer that mimics the behavior of a mine subjected to acoustic waves is not ideal. Indeed, since the k-wave package does not allow for the simulation of specific shapes, replacing it with a layer appears to be the best solution. The parameters of the source and receiver remain unchanged from the previous configuration to remain consistent. Table 4.2 and Figure 4.9, respectively, present the physical parameters assigned to the layers and the way they are arranged.

The Matlab code for the two configurations is provided in Appendix C.

Table 4.1: Physical parameters of the different simulated layers for the first configuration (water-sand layers).

Layer	**Cp (m/s)**	**Cs (m/s)**	**ρ (kg/m³)**
Water	1400	not applicable	1000
Sand	2000	800	1800

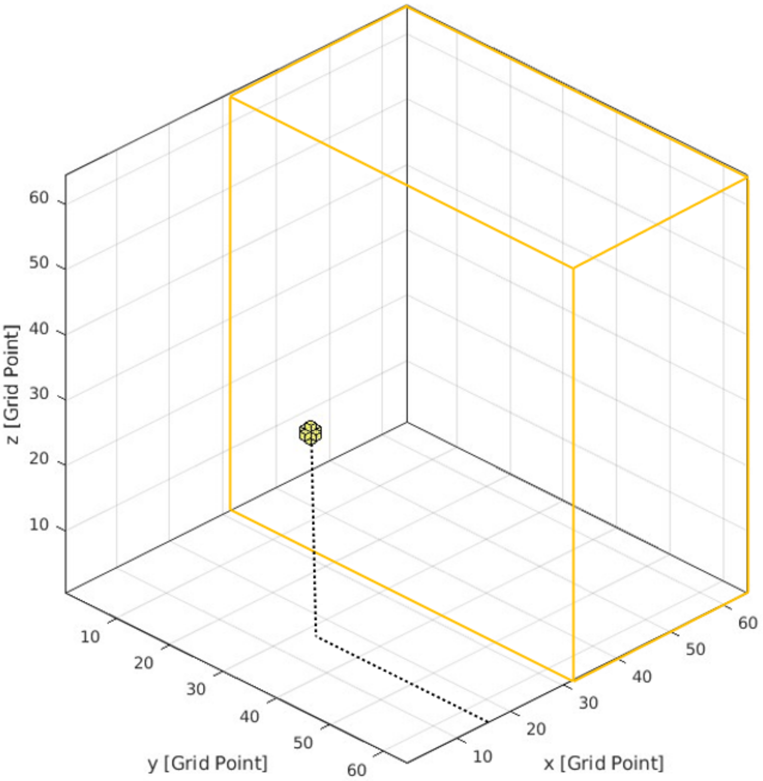

Figure 4.8: Simulation grid of 64×64×64 with a grid space of 0.0013 m, totaling 8×8×8 cm. The source/receiver is marked by the yellow ball within the water layer and more than 2 cm away from the orange sand layer (marine sediments).

Table 4.2: Physical parameters of the different simulated layers for the second configuration (water-mine-like-sand layers).

Layer	**Cp (m/s)**	**Cs (m/s)**	**ρ (kg/m^3)**
Water	1400	not applicable	1000
Mine-like (steel)	5800	3100	7850
Sand	2000	800	1800

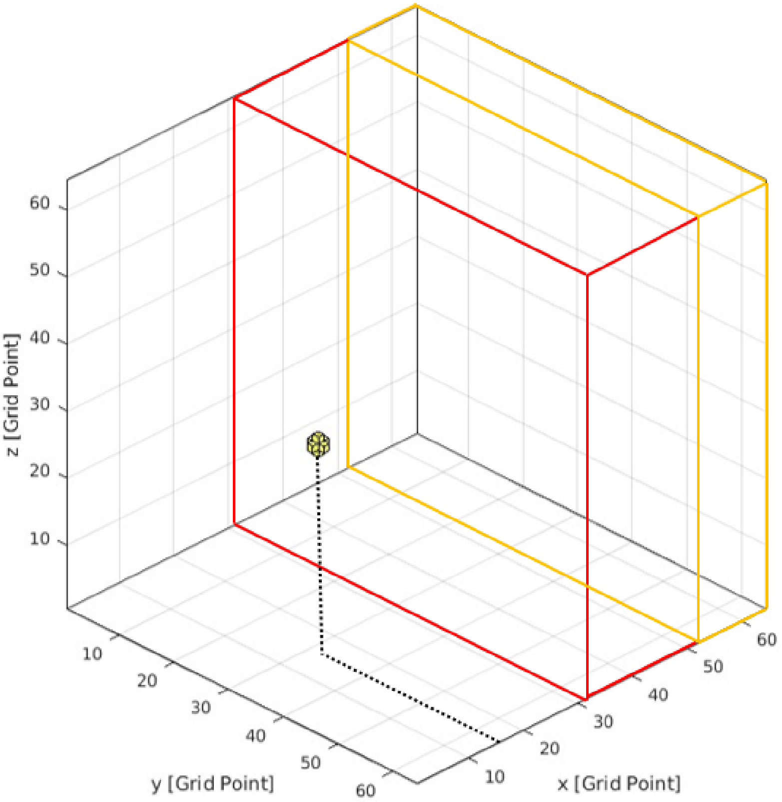

Figure 4.9: Simulation grid of 64×64×64 with a grid space of 0.0013 m, totaling 8×8×8 cm. The source/receiver is marked by the yellow ball within the water layer and more than 2 cm away from the mine-like layer (in red). The third layer is sand (in orange) and is approximately 5 cm apart from the sensor.

Chapter 5

Results

5.1 Laboratory experiments

5.1.1 Gain function acquisition

The graph of acquisition of the different return strength profiles provided by the sensor over the 400-700 distance interval (429-715 mm if considering the virtual origin) is included in Figure 5.1. The signal can be divided into two main parts. The first part of the signal is roughly between $x = 0$ ms and $x = 0.25$ ms and is also called the *ringing signal* because it refers to the internal resonance artifact of the sensor. The second part, which starts at the end of the first and continues to the end of the scan length, refers to the return echo information.

The choice of a user-adjustable gain equivalent to 5 is made so that a maximum of the values presented does not show a complete saturated *ringing signal.* However, the measurement for 625 mm remains relatively too saturated and is therefore excluded, as it does not allow for a reliable estimation of the applied gain function.

Figure 5.1 shows several profiles in which the first part displays relatively similar signals but on different scales. A recognizable repeating pattern is apparent. For the second part of the signal corresponding to the return echo, the distance detection peaks correspond to the saturated peaks. If one calculates the traveled distance by referencing the saturated peak, this distance indeed matches that returned by the sensor. Each detection peak (in the second part of the signal) is separated by a gap that indicates the additional time that the signal takes to reflect off its target. The overall pattern is therefore relatively consistent, as it is possible to observe that these peaks move farther apart as time, and consequently distance, progresses.

The presence of these saturated peaks in each of the profiles suggests that the sensor adjusts its signal at each distance so that the returned distance is the saturated value. Therefore, the concept of corrective and automatic gains makes perfect sense. To best retrieve this gain value, it is important to focus on the first part of the signal (*ringing signal*) to understand how these profiles are scaled.

An additional observation is that, for most detection peaks in the second part of the signal, the value reaches a maximum of 255 once before decreasing. This observation is valid with the exception of the 625 mm signal. This behavior is often observed during data acquisition and can be attributed to wave interference effects. In particular, constructive interference occurs when waves combine coherently, reinforcing the reflected signal and resulting in a stronger return. Conversely, destructive interference happens when waves combine out of phase, effectively canceling out the reflection associated with a specific scattering event. As McGrane et al. [2004] explain, constructive interference amplifies reflections, while destructive interference can even cause the reflection zone to disappear entirely.

Finally, it is also interesting to note that in its initial part, the signal retrieved for all these values tends to increase as the distance between the sensor and the detected interface increases (valid for the range from 429 to 560 mm). Meanwhile, for other measurements, the opposite behavior is observed (range from 675 to 715 mm). However, these changes are not abrupt and appear to occur between two intervals or "zones" where the behavior remains consistent.

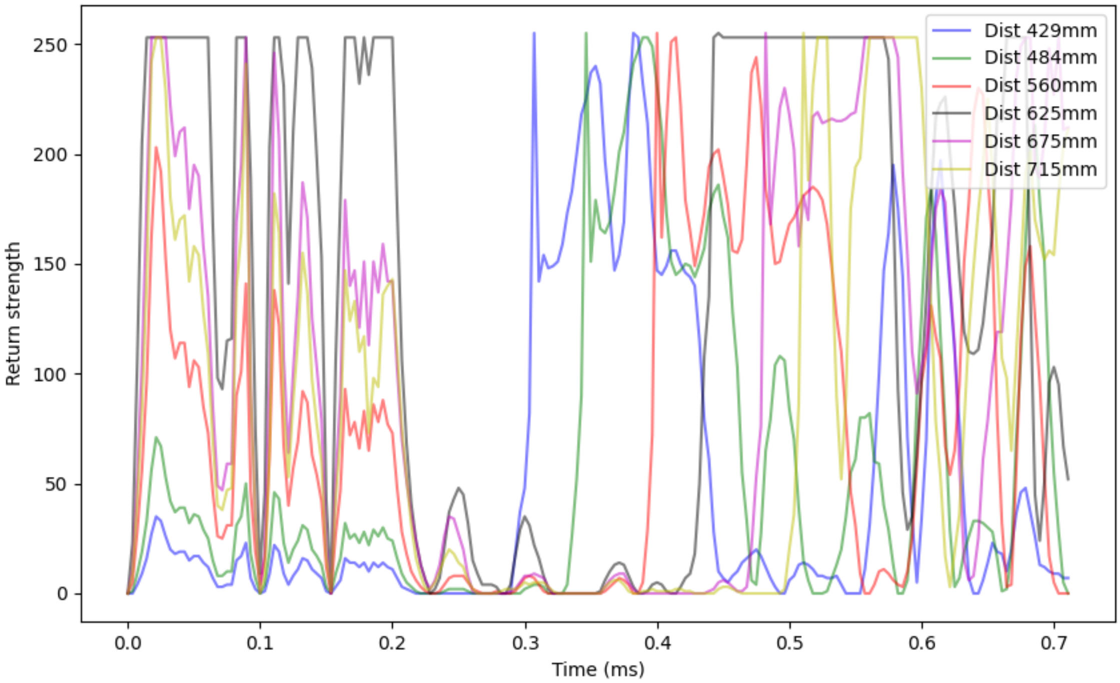

Figure 5.1: Profile data from 429 to 715 mm (values returned by the transducer) with a user-adjustable fixed gain of 5.

Figure 5.2 illustrates the first step of the process presented in the methodology chapter (see 4.1.1) to try to fit a linear model. To begin, the reference signal must be designated, corresponding to the smallest signal in the presented interval, specifically the signal for the 429 mm distance. Based on the basic assumption that the gain varies with distance, selecting the shortest distance value as the reference signal is a logical choice. In this example, the signal of interest corresponds to 484 mm.

Figure 5.2 provides a zoomed view of the initial segment of the signal, with a threshold assigned to each of the two studied signals to isolate their higher segments. This step is crucial to capture the tendency of the signals to increase with distance. The threshold is set at a relatively high identifiable point that recurs consistently across all retrieved signals. These thresholds are represented by red circles and are equivalent to 10 for the first signal and 22 for the second signal.

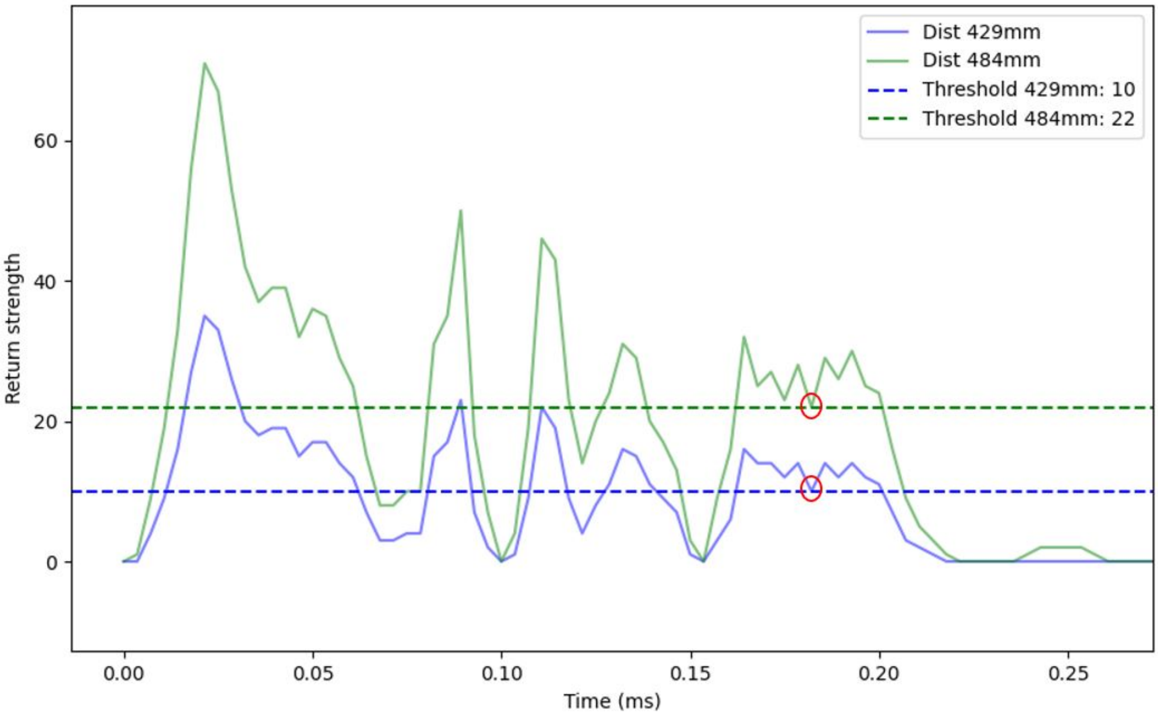

Figure 5.2: First part (*ringing signal*) of the two signals studied with a threshold (in red circle) applied to all the corresponding profile data.

Figure 5.3 presents the ratio of all values that exceed the threshold of 22 for the second signal (484 mm) to those that exceed the threshold of 10 for the reference signal (429 mm). The graph is divided into two main sections. It is readily observed that the first section is relatively flat, whereas the second exhibits numerous variations. These results support the hypothesis that the initial portion of a signal at one distance closely resembles the corresponding portion of a signal at a different distance. This similarity holds except for a scaling factor that appears to multiply the values of the first signal to produce the second.

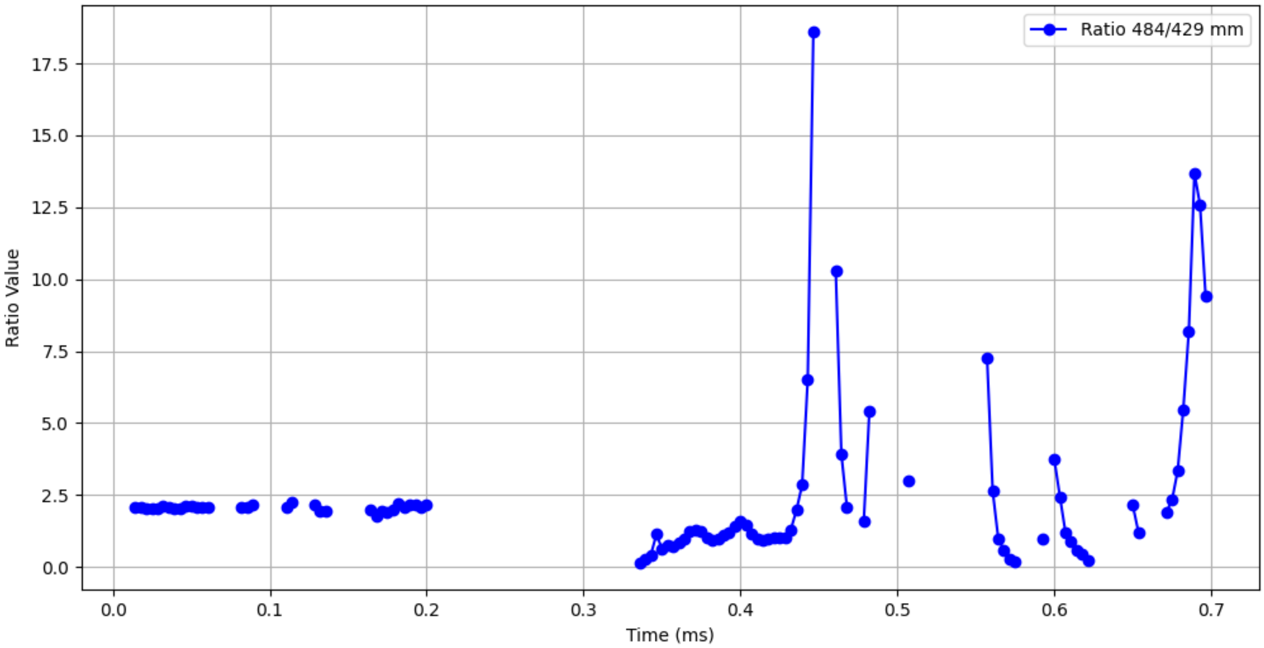

Figure 5.3: Graph of the ratio of the first signal (interest signal) to the second signal (reference signal) for values exceeding their respective threshold.

Figure 5.4 provides a zoomed view of the initial section, previously described as relatively flat. Upon closer inspection, a more scattered distribution of points becomes apparent. With the ratio values now magnified, it seems that they change over time.

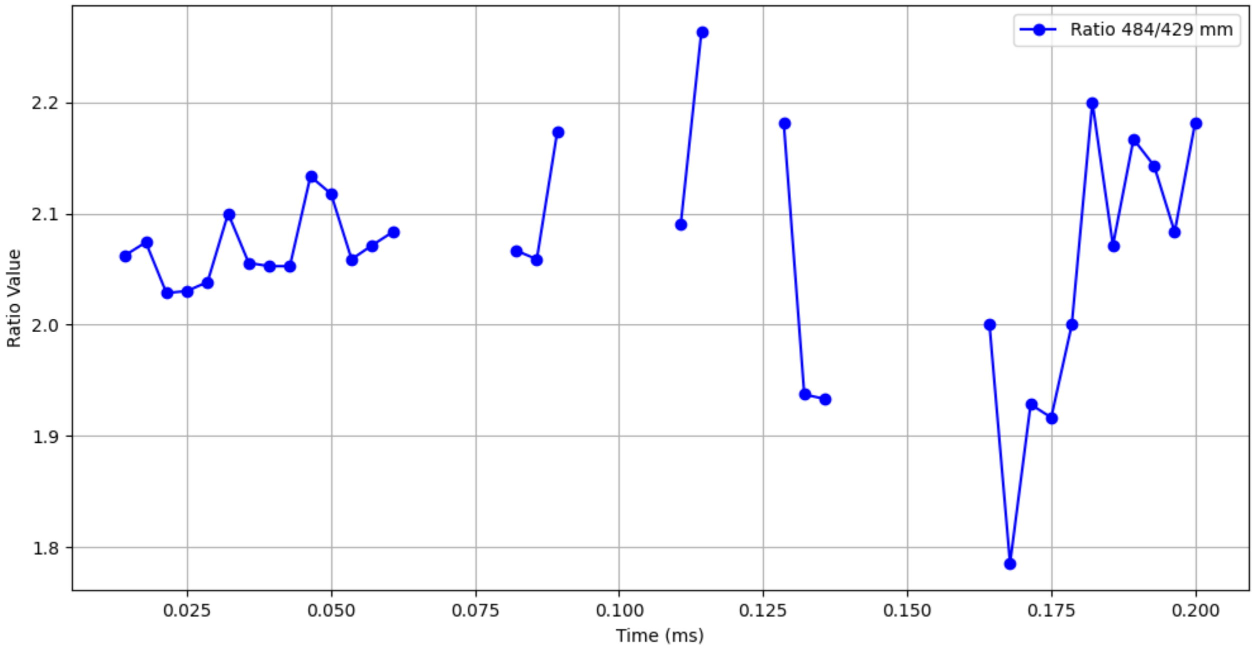

Figure 5.4: Zoom on the initial section of the graph showing the ratio between the two studied signals.

Figure 5.5 represents the final step in the gain function recovery process. By fitting a linear regression model to the set of residual points, the resulting line equation corresponds to the gain function. In this case, it corresponds to: $g(t) = -0.085 \cdot t + 2.074$. However, this figure also shows that the data do not clearly follow a linear trend and that if we try to fit a linear model anyway, its slope is very small. A correlation coefficient of -0.059 indicates a very weak and negative relationship between the two variables, suggesting that they are almost independent. The R^2 value of 0.003 shows that the independent variable explains only a negligible portion of the variation in the dependent variable. Note that the very small value of the slope can also be explained by the noise level encountered, which renders it insignificant. In other words, the apparent variations in gain could simply be due to noise rather than an actual variation.

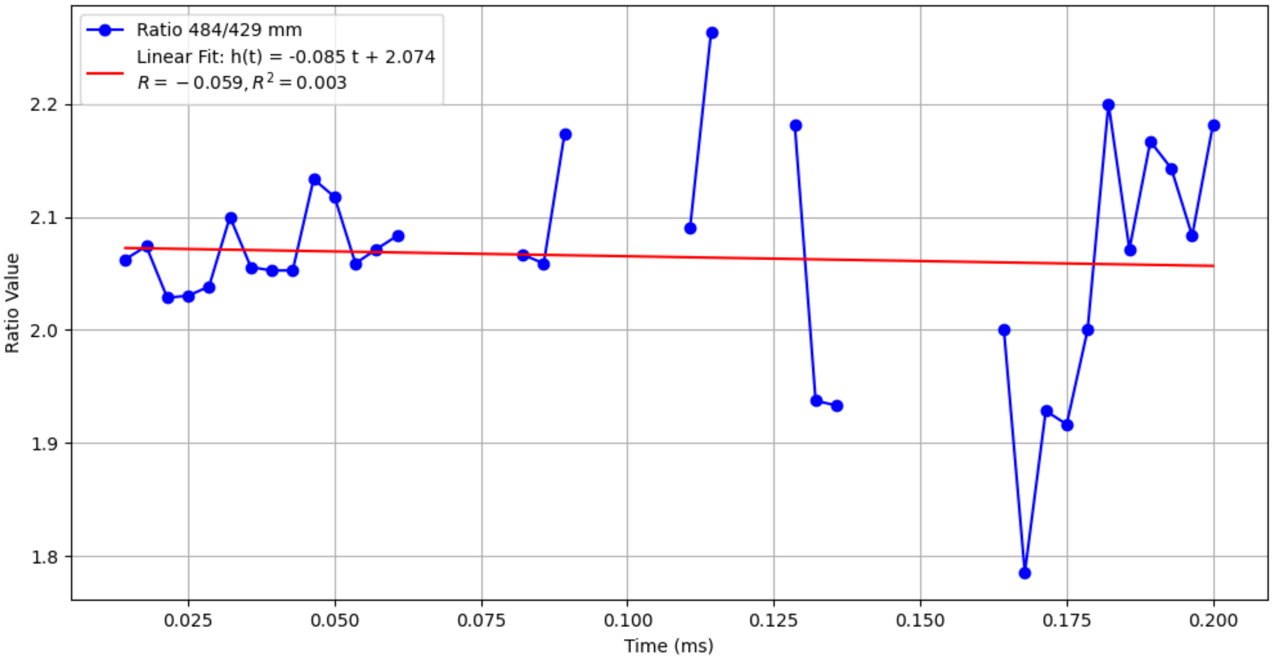

Figure 5.5: Graph of the linear model applied to all the values resulting from the ratio of the previously filtered points.

Now, repeating the gain calculation process across all signals in the range of 429 to 715 mm allows one to obtain 3 other equations which are presented and fitted in Figure 5.6. The observation remains the same as before. In fact, even though the slopes of the lines are all positive this time, the R^2 values are too low to conclude that a linear model fits. Figure 5.7 allows for better visualization of these previously obtained lines. It also shows a line whose equation would have allowed us to recover the average gain function applied across a whole set of values if this linear relationship had been proven, but attempting to combine all these equations into an average equation is not conclusive. Consequently, our applied gain function called $g(t)$ cannot be attributed to the average equation of the linear regression. The regression hypothesis is thus rejected along with the trend because the gain of the system automatically changes.

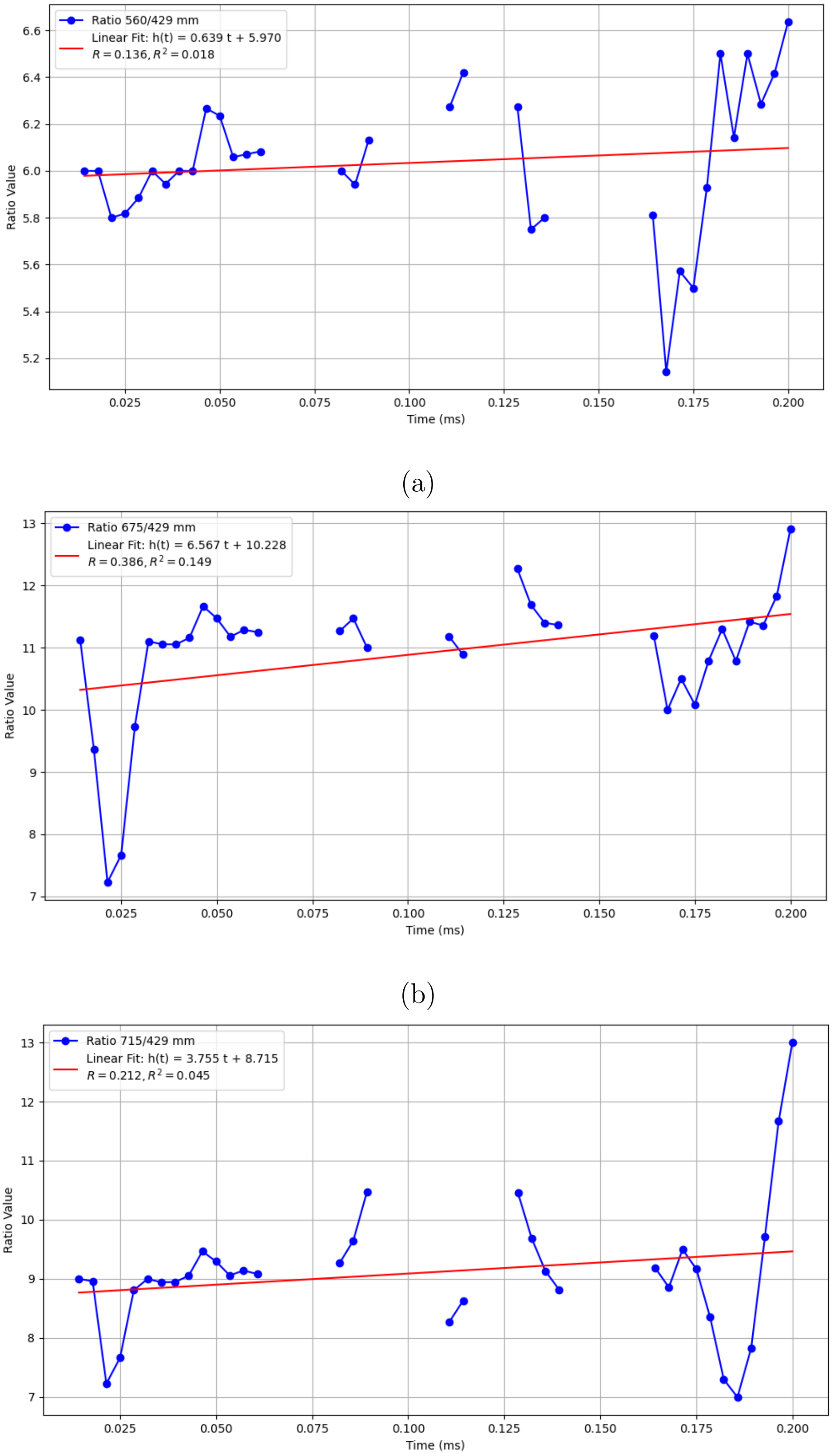

(a)

(b)

(c)

Figure 5.6: (a) Plotting the straight line of the linear model on the interest signal of 560 mm, (b) of 675 mm, and (c) of 715 mm.

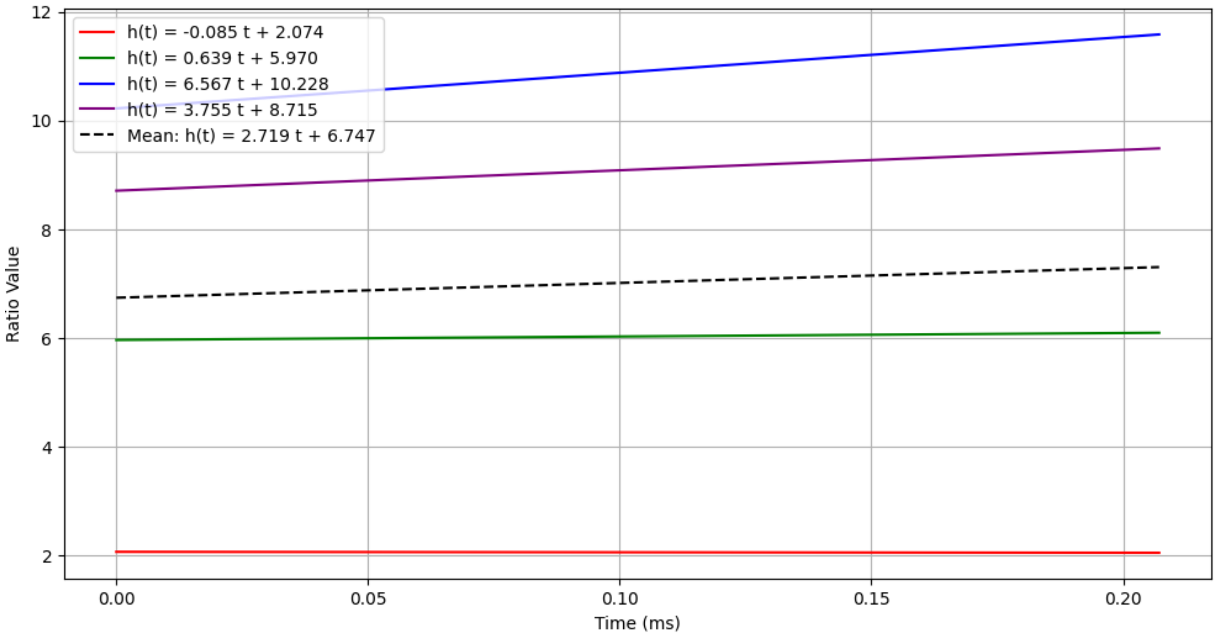

Figure 5.7: Linear regressions for different signals along the studied interval (429 to 715 mm) and the average gain equation.

The final figure dealing with the gain is that of the normalized signal (see Figure 5.8). To obtain this graph, start with the raw unprocessed signals and divide each of them by their characteristic linear equation (although the linear relationship is not proven). This normalized signal is quite interesting as it rescales all signals based on the importance of the amplitude of their first section.

After this division, we can observe that almost all signals share an identical ringing signal which is representative of direct reflections inside the sensor. Subsequently, each signal shows a first reflection, which is the target, followed by multiple reflections. These same multiple reflections are also followed by reflections coming from a distance greater than the target. It is also interesting that the first reflection due to the target for an initial signal (at a shorter distance) is followed by a similar but weaker reflection at a greater distance. This observation can be generalized for the first 4 signals, but not for the last signal at 715 mm, which increases instead of decreasing. The observed increase in the peak may be the result of constructive interference caused by internal sensor reflections or external clutter, for example, the edges of the box.

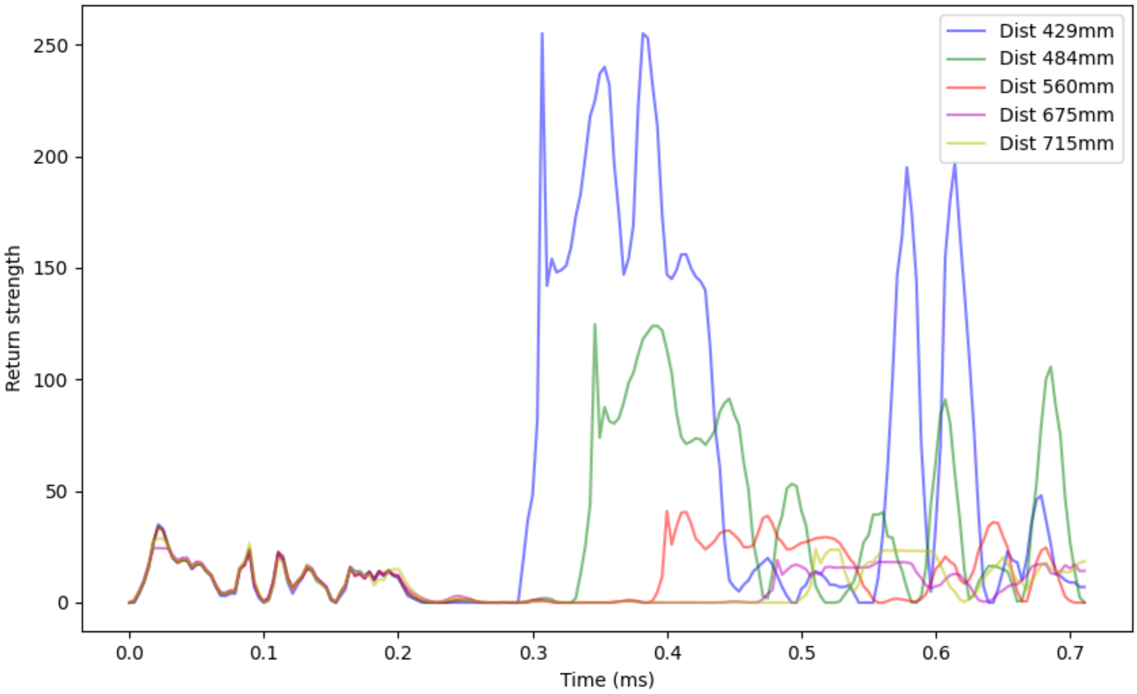

Figure 5.8: Signals collected by the sensor during measurements taken at different distances from the bottom of the tank, from which the previously calculated linear gain functions have been removed.

5.1.2 Perfect acoustic reflector (PAR) measurements

Figure 5.9 allows us to visualize the difference between using a user-adjustable gain of 5 and 0. For a gain of 0, the air-water interface is clearly visible, and only a slight mark of multiple reflection is observed. They are visible at 0.6 m, which is twice the position of the perfect acoustic reflector at 0.3 m (two-way travel distance). The use of a gain of 5 is tinged with multiple reflections between the sensor and the water-air interface again.

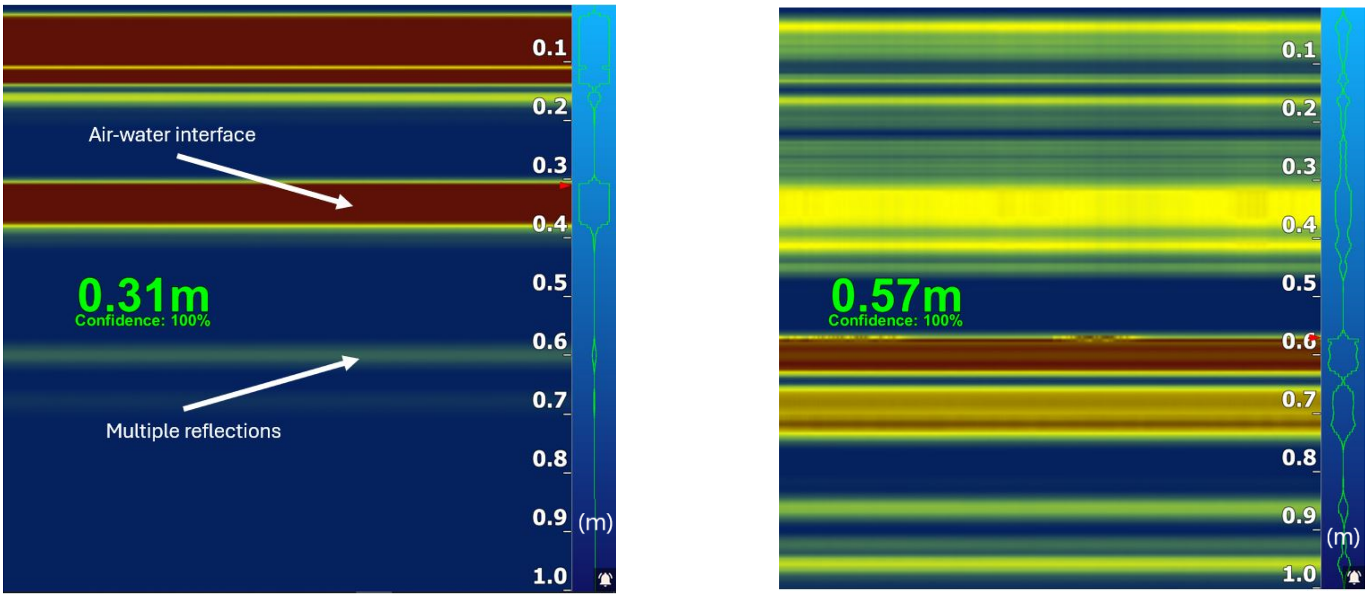

(a)

(b)

Figure 5.9: Images from the Ping Viewer application. Both images were taken in the same configurations and distances, with only the user-adjustable gain changing. (a) uses a gain of 0, while (b) uses a gain of 5.

For sensor calibration, several signals recorded at different heights and involving the PAR configuration have been recovered. Figure 5.10 shows the plot of these signals.

The distances returned by the sensor are not accurate. Indeed, when moving from gain 0 to 5, the measurements seem to focus on multiple reflections. However, a first detection peak (inside the red dashed lines) for each measurement is visible near the actual distances separating the sensor from the water-air interface and does not saturate.

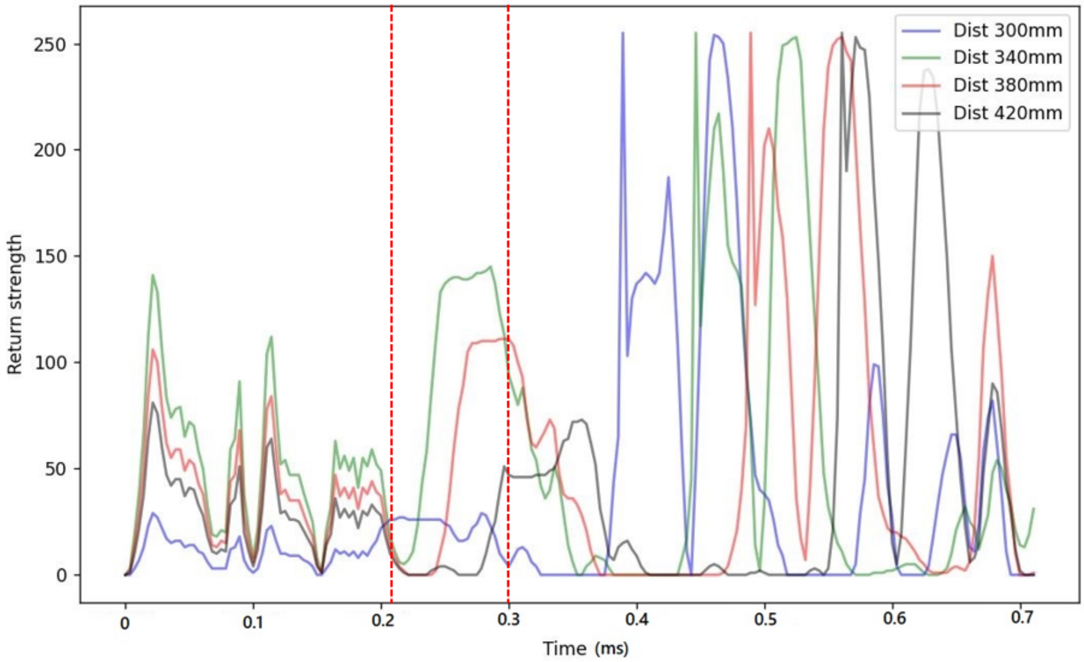

Figure 5.10: Graph for 4 different heights spaced 4 cm apart in the perfect acoustic reflector configuration. The area between the red dashed lines indicates where the detection peaks would be located if the user-adjustable gain had been set to 0.

5.1.3 B-scans scenarios

The B-scan results obtained with the sensor show significant differences depending on the configurations studied. In Figure 5.11 (a), only a Plexiglas plate is present at the bottom of the tank. It is therefore possible to observe a distinct yellow line appearing after 0.3 milliseconds, indicating a clear reflection of the signal as it strikes this rigid, dense surface. However, vertical artifacts due to the high gain interfere with accurate detection of the real background. It is noticeable that the signal is irregular (mostly at the beginning) due to the sensor's acceleration and deceleration phases. This irregularity can also be explained by the presence of a rounded dome that acts as a water outlet on the side of the water tank. This dome, curved inward, introduces a discontinuity in the ground reflections, adding further disturbances superimposed on those linked to acceleration at the start of the movement.

In Figure 5.11 (b), with 1.5 cm of sand added (see Figure 4.5 (a)), a more diffuse reflection is observed just at the 0.3 ms mark, indicating that the level of the reflected surface has increased. Absorption and scattering of ultrasonic waves by the sand attenuate the reflected signal, making the background less distinct and introducing a slight delay compared with the Plexiglas in its configuration alone. This attenuation can also be explained by a smaller reflection coefficient with the new water-sand interface. Variations in the speed of the transducer and the rounded dome continue to affect the signal at the beginning of the scan, creating disturbed and less coherent patterns. Sand also introduces the notion of discontinuity since the way it is incorporated into the tank does not allow for a smooth deposit. As a result, the impression of a smooth surface, as observed in the configuration with only Plexiglas, is slightly lost.

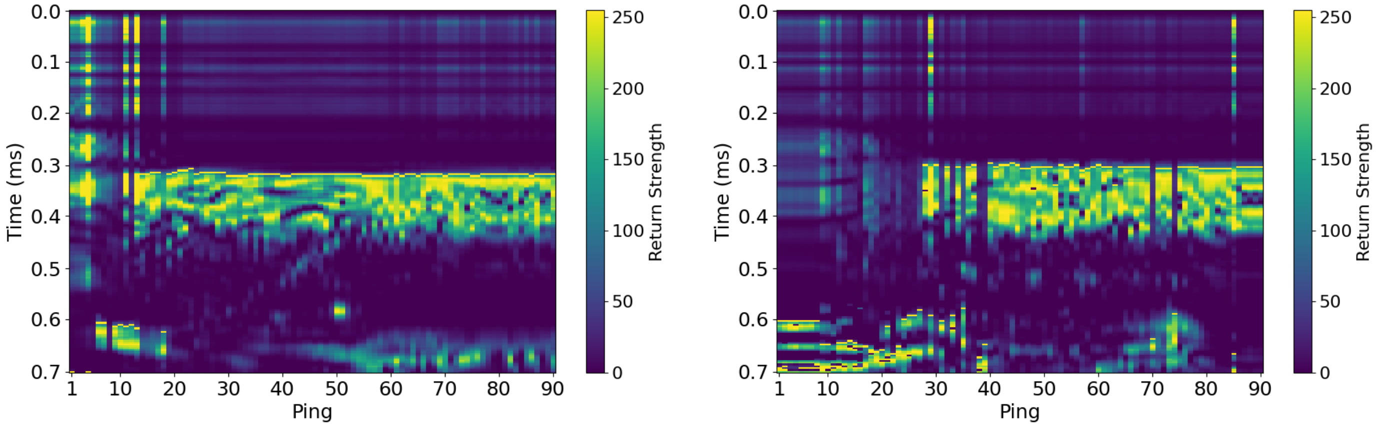

(a)

(b)

Figure 5.11: B-scan over 80 cm length and gain at 5. (a) is the configuration with Plexiglas alone and (b) shows both the Plexiglas and 1.5 cm of sand superimposed. Neither includes a target.

When a target is added on top of this sand layer (see Figure 4.5 (b)), such as a brick in the case of Figure 5.12 (a), the B scan shows complex reflections between 0.2 and 0.3 milliseconds. Concrete brick, as a dense and rigid material, introduces marked reflection patterns and areas of high yellow intensity visible between pings 30 and 60 marked with a red rectangle. These patterns are due to the presence of an additional interface in addition to sand, in this case brick. As in previous configurations, the start of the B-scan remains affected by perturbations in the experiment's configuration.

An interesting observation is to add to the previous configuration a second target. This time, the new target is lighter, less dense, and smaller than the first. This refers to the rock located on the left in Figure 4.3. Figure 5.12 (b), which refers to the configuration 4.5 (c), clearly shows once again the brick placed next to the stone. However, the rock, which should appear around ping 70, is not directly visible (it should be located at the end of the red arrow). This may be due to its smaller size and the lack of a sufficiently large flat reflective surface.

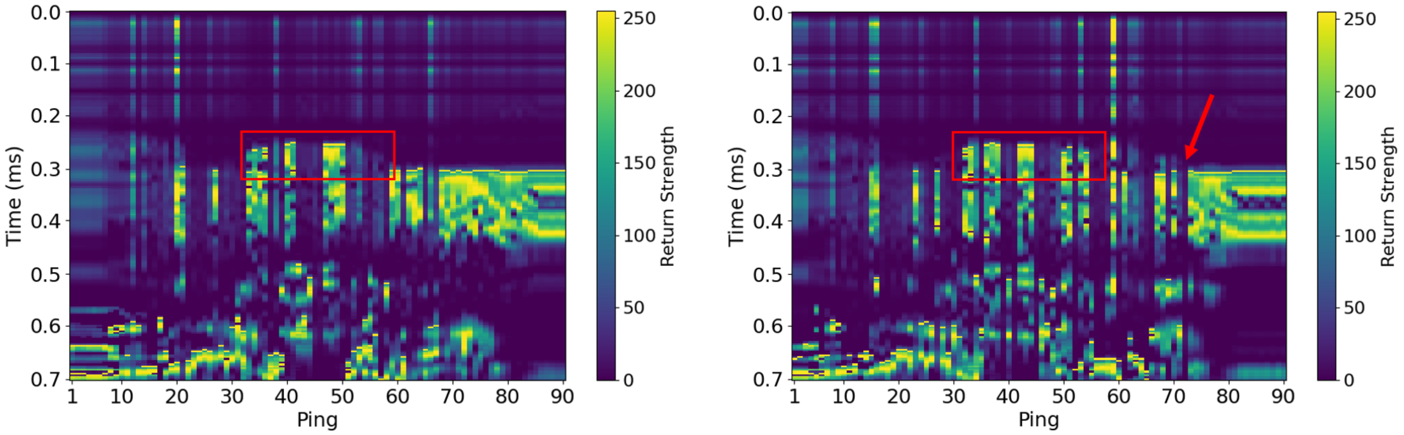

(a)

(b)

Figure 5.12: B-scan over 80 cm length and gain at 5. (a) is the configuration with Plexiglas, 1.5 cm of sand and a target (brick) in the red rectangle and (b) is Plexiglas, 1.5 cm of sand and two targets side by side (brick and rock). The red arrow indicates where the rock should be detected.

This paragraph is now included in this results section to test the detection range of the Ping2 sensor. The manufacturer specifies a -3 dB beam width of 25 degrees.°. Knowing the height separating the sensor from the target and the value of this angle (see Figure 5.13), it is easy to calculate that the sensor will have difficulty effectively detecting the target once the cross distance (the distance between the sensor and the target perpendicular to the motion) exceeds approximately 10 centimeters, as calculated in the following Equation (5.1):

$$x = 45\,\text{cm} \cdot \tan(12.5^\circ), \tag{5.1}$$

giving:

$$x \approx 45 \cdot 0.2217 \approx 9.98\,\text{cm}$$

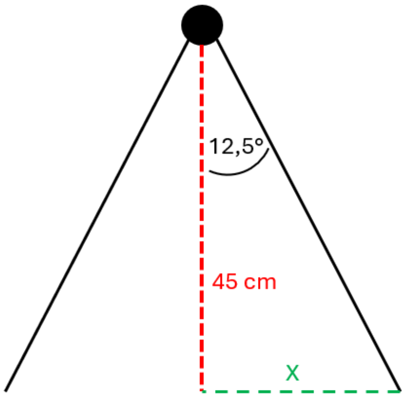

Figure 5.13: Calculation of the maximum effective detection distance (in green), also known as the cross distance.

If we refer to Figure 5.14, this is indeed what can be observed. In image (a), when the cross distance is 10 cm, the concrete brick is barely detected (in the red rectangle) and appears much less clearly than in the previous figures. Although it is still possible to detect a trace of the brick, it is because the brick still appears at the edge of the beam, as part of its length remains visible in the field. Note that the brick still appears in the same ping interval because it has not moved. It is the sensor that has been slightly shifted by a few centimeters along its Y-axis. However, once this distance is increased by a few centimeters (until 25 cm), as in image (b), the brick completely disappears from the sensor's field of view, confirming the sensor's functional range. However, it is possible that a part of the brick is indeed hit, but its orientation relative to the incident waves causes reflections that do not return to the sensor.

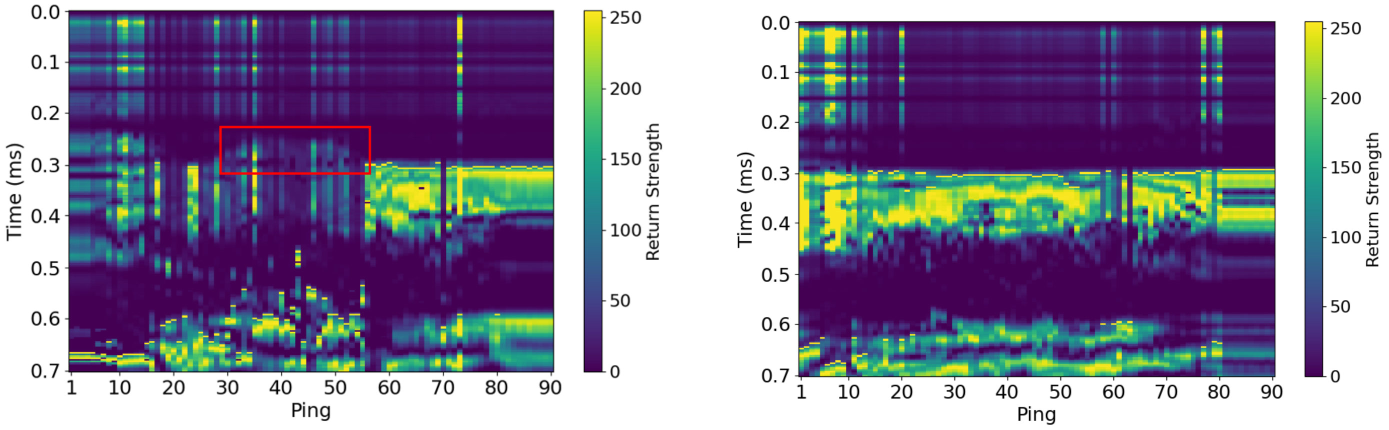

(a)

(b)

Figure 5.14: B-scan over a length of 80 cm and gain at 5. (a) is the B-scan for a cross-distance configuration equal to 10 cm with the concrete brick in the red rectangle and (b) for a cross-distance of 25 cm. Both configurations include the Plexiglas layer, a 1.5 cm layer of sand and a brick.

The final experimental configuration involving B-scans concerns the detection of a concrete brick at different burial depths in the sand. Figure 5.15 presents the four scenarios tested, in which a progressive decrease in the visibility of the brick is observed as the thickness of the sand layer increases. In Figure 5.15 (d), the top surface of the brick is barely visible from the surface of the sand. However, we can see that the brick sends a stronger signal than the surrounding sand. Since the brick is denser, it is no surprise that the reflection is greater.

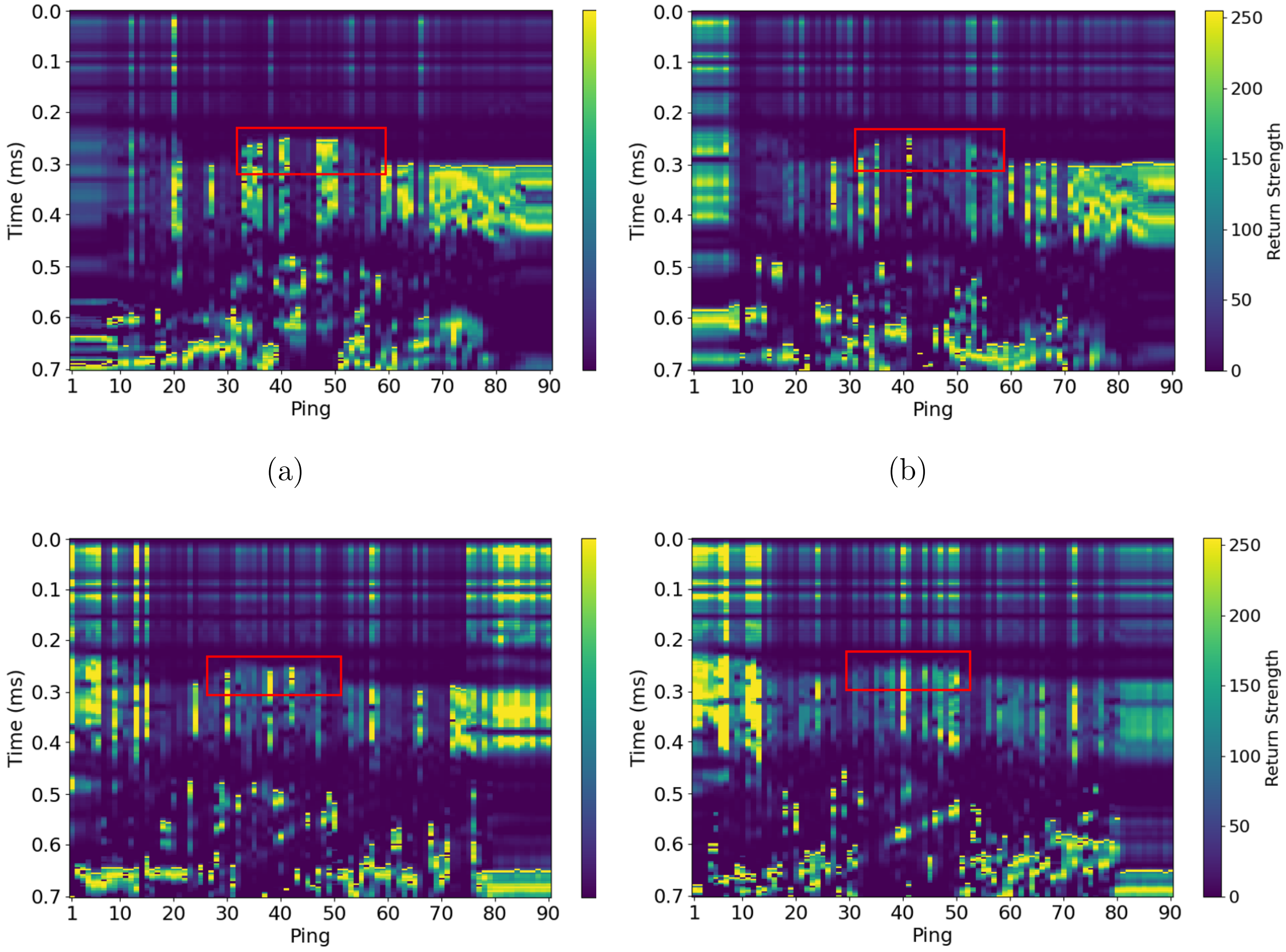

(a) (b)

(c) (d)

Figure 5.15: (a) B-scan with a brick, just above the surface of the sand (b) B-scan for the brick buried in 1.5 cm of sand (c) B-scan for the brick buried in 2.5 cm of sand (d) B-scan for the brick almost fully buried. The brick is in the red rectangle in both images.

5.2 Numerical simulations

5.2.1 Green's function and free field simulations

Thanks to the optimized CPU codes, the simulation for the configuration with a 30 and 38-centimeter distance between the monostatic sensor and the water-air interface is completed in just over 7 hours.

A simple sketch showing the sensor for simulations conducted at distances of 30 cm and 38 cm from the air-water interface is shown in Figure 5.16.

As stated earlier, the receiver is a unitary point located exactly in the middle of the emitting source. It is possible to record the signals received by this entity throughout the simulation. Figure 5.17 specifically shows the history of the signals received by the sensor when a water-air interface is placed 30 cm from it. The vertical axis represents the intensity of the received signal, ranging from 0 to 1 with black indicating high pressures and yellow tending toward zero pressures, but also from 0 to -1 for negative pressures. This value scale enables one to capture even the slightest variations, allowing us to analyze the behavior of the waves during the simulation. In this figure, a distinct black mark can easily be observed at the initiation of the simulation. This corresponds to the signal emitted by the source and directly captured by the receiver.

Then, just after 0.1 ms, a second mark is visible. To understand this second mark, it is essential to consider how the source emits waves. This source cannot be configured with a beam angle and therefore emits waves circularly from its center in all directions. Thus, as shown in Figure 5.18, the waves propagating to the right, left, and behind quickly bounce off the edges of the simulation. This behavior is suboptimal because the PML should act as an absorbing layer but seems to be unable to absorb all the incident waves. This occurs when the simulated pressure amplitudes are too high for the k-wave package. However, Figure 5.19, which captures the sensor signal according to the pressures encountered, does not indicate this pressure peak, suggesting that these pressures are minimal and do not interfere with the received signal. Therefore, PML works relatively well.

Finally, around 0.4 ms (corresponding to a distance of 60 cm for the wave to reach the interface and return to the sensor), reflections caused by the encounter with the perfect acoustic reflector can be observed. These waves that return to the source after nearly bouncing off the interface appear to be broken down into multiple waves, as if they interact with the structure, causing multiple reflections and giving them a fragmented appearance.

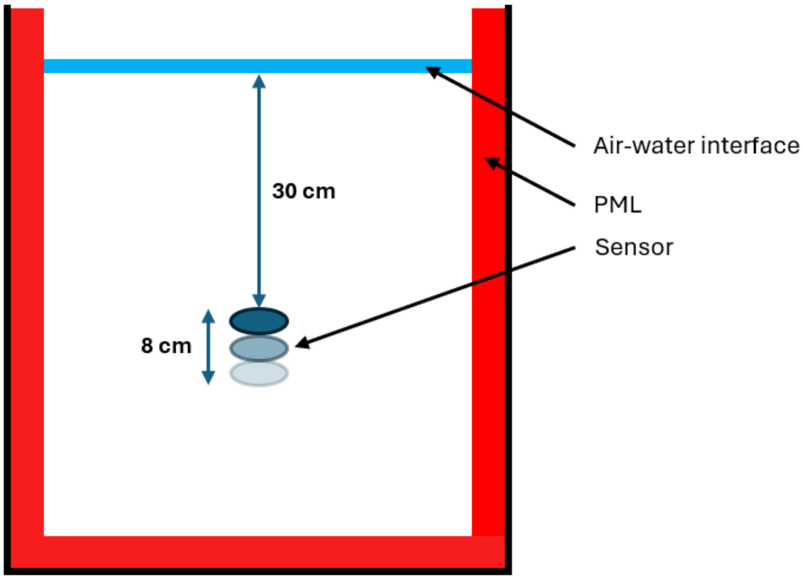

Figure 5.16: Simple sketch of the configuration for the water-air interface at 30 cm and 38 cm from the sensor.

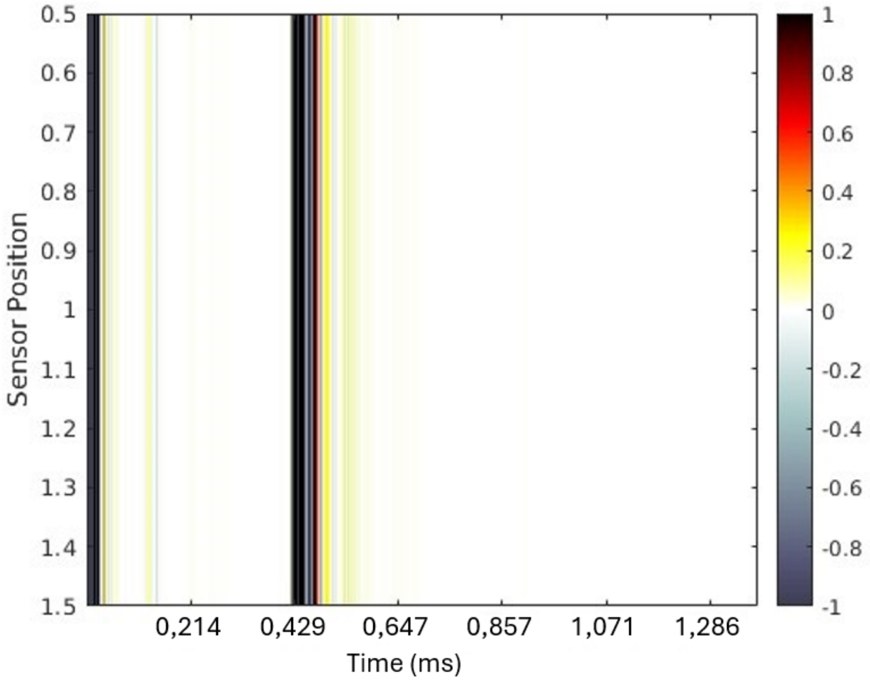

Figure 5.17: Graph of the pressure return against a water-air interface located 30 cm away from a point source of 7943 Pa. The x-axis, which was previously expressed in time steps, has been converted back to ms.

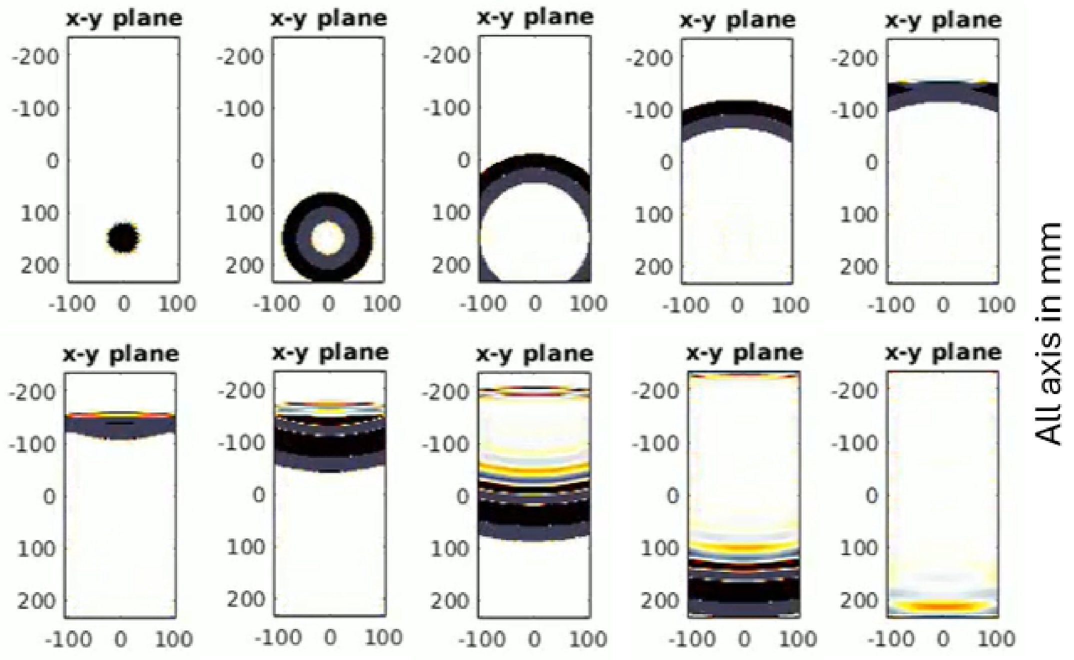

Figure 5.18: Time lapse of the simulation of an incident wave of 7943 Pa at 30 cm from a water-air interface. The source/receiver is

Figure 5.19, which presents the signal recorded by the sensor, traces the pressure changes within it. At the start of this simulation, the source records a positive pressure variation of nearly 8000 Pa due to the emission of waves by the source. Shortly after, the signal drops to negative pressures, reaching almost -80,000 Pa. This extreme pressure is explained by the fact that the sensor is located within the source itself. Since the distance between the source and the sensor is very small (possibly zero), the direct signal could theoretically be infinite, leading to these extreme pressure values. This behavior varies depending on the model implementation. The remainder of the signal is relatively smooth, staying close to a pressure of 0 Pa most of the time, until the waves reflected by the interface return to the sensor. Thus, after 0.4 ms, a pressure variation can be observed due to their return to the sensor. Figure 5.19 (b) provides a close-up view of this pressure variation, showing values of a few hundred Pascals.

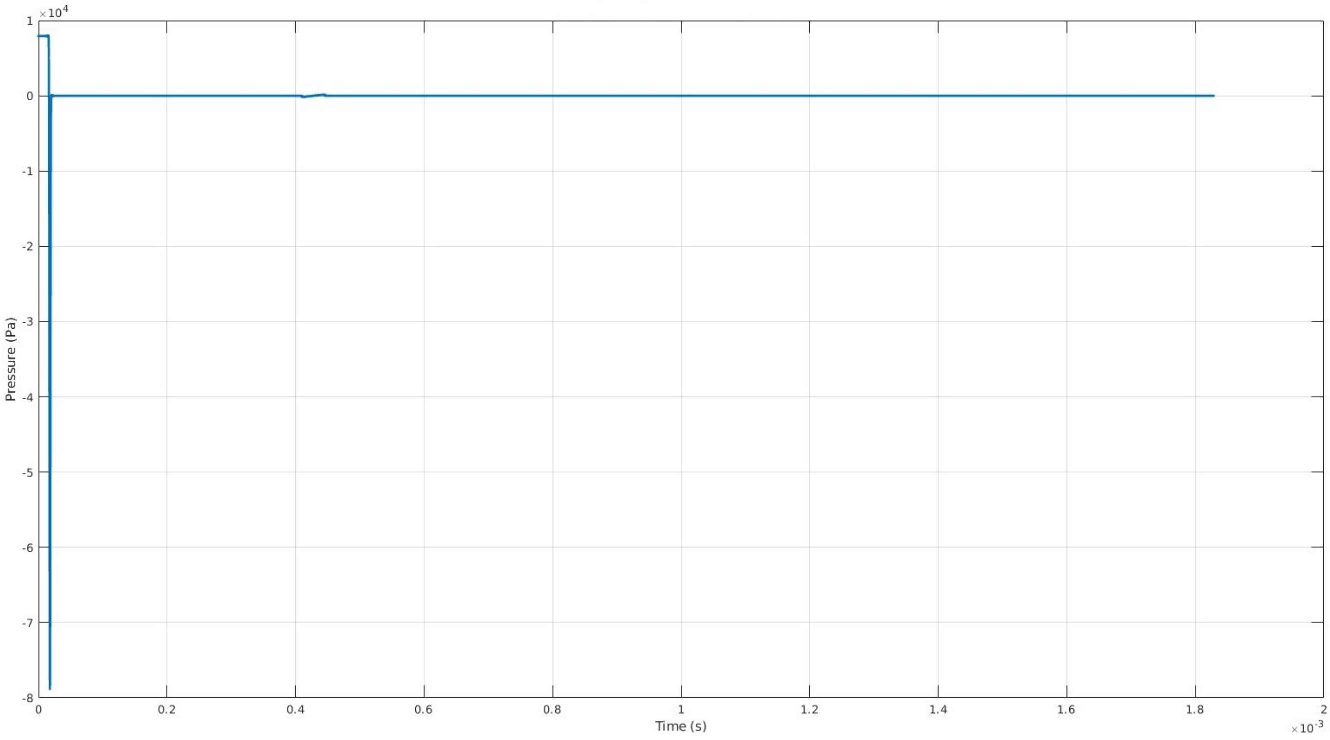

(a)

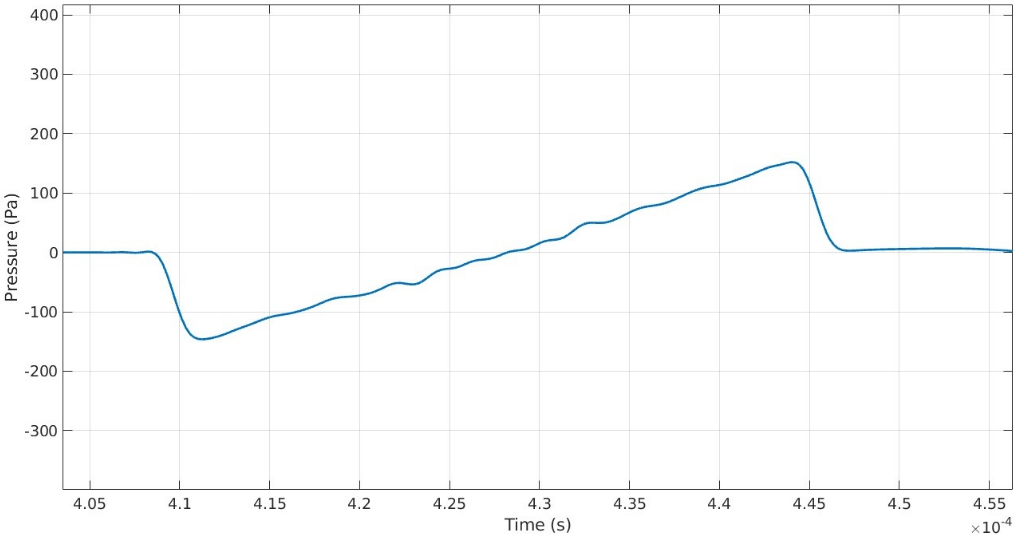

(b)

Figure 5.19: (a) Signal received by the sensor for a water-air interface located 30 cm from a point source of 7943 Pa. (b) provides a close-up of the pressure change caused by the returning waves.

After measuring the pressure evolution 30 cm from the interface, it is possible, by removing the interface, to perform a simple pressure measurement in the free field, the result of which is shown in Figure 5.20. As previously observed, the same pressure variations (of the same magnitude) appear at the beginning of the simulation. The remainder of the graph is a line that hovers around 0 Pa throughout the time interval. This serves as a verification that the simulation is working correctly, as no pressure changes are recorded. The free field simulation for 30 cm and 38 cm is identical, since both simulations share the same grid dimensions. Even if the source is in different locations, the signal recorded by the sensor remains the same because no wave is reflected from the absorbing boundary conditions.

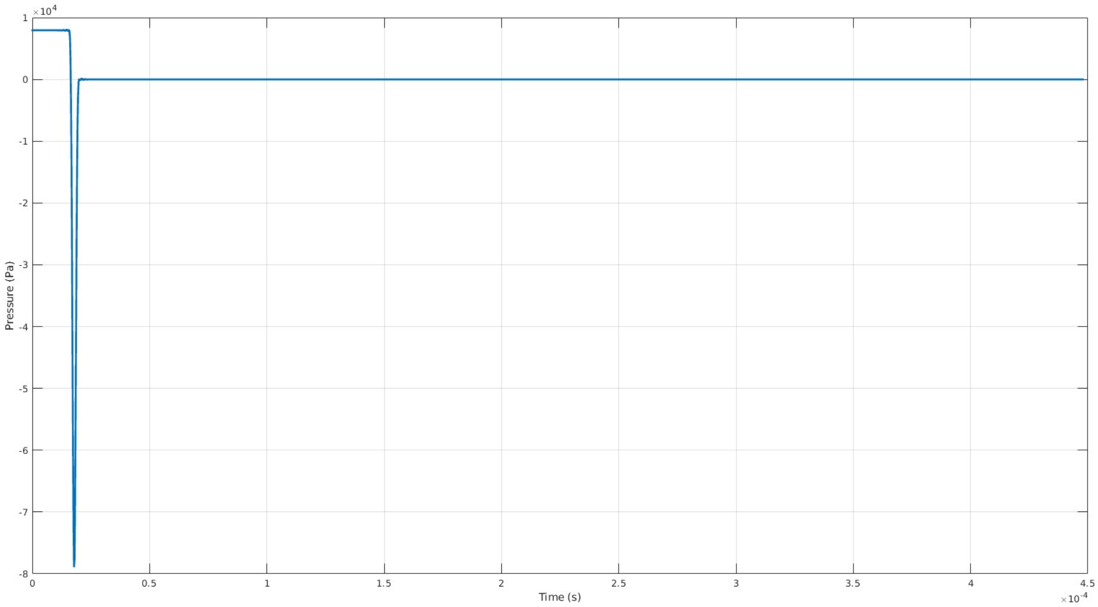

Figure 5.20: Free feel signal for a point source at 7943 Pa and a grid size of 512*256*256 mm.

The retrieval of $H_i(t)$ (here in the time domain as it allows for a simple subtraction without requiring a Fourier transform like in the frequency domain) presented earlier in Section 2.5 is possible once the signal is recorded for both the interface configuration and the free field configuration. It simply requires subtracting the free field signal from the signal obtained with the interface. By doing so, it is possible to isolate a signal that represents only the pressure variation caused by the interaction with the interface, free from any disturbances related to the sensor itself. The result for the 30 cm simulation is presented in Figure 5.21 and in Figure 5.22 for the 38 cm simulation.

These two filtered signals are quite interesting because they provide a relatively clean and well-detailed representation of the signal resulting from the reflection of the incident waves. Another observable phenomenon is the attenuation of waves as they travel through the computational grid. It seems that the attenuation follows a pattern 1/R due to the spherical spreading of the waves (with R equal to the distance traveled). For just an additional 16 cm of travel, an attenuation of approximately 20 Pa is observed in the positive range and around 20 Pa in the negative range between the two signals.

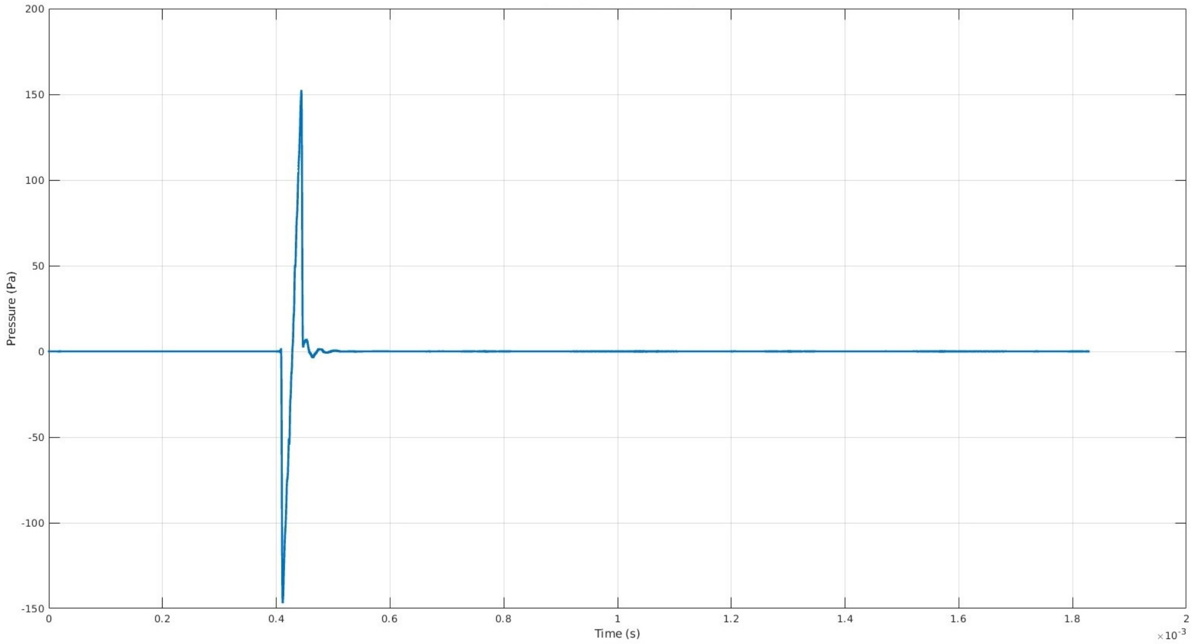

Figure 5.21: Filtered $H_i(\omega)$ signal for a water-air interface located 30 cm from a point source of 7943 Pa.

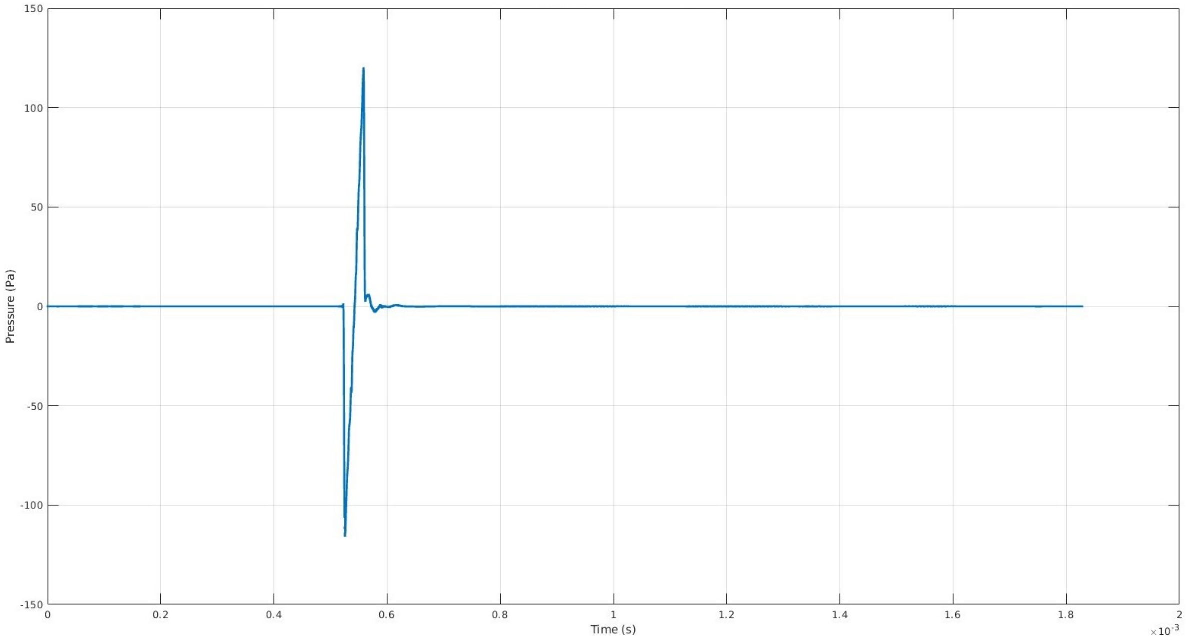

Figure 5.22: Filtered $H_i(\omega)$ signal for a water-air interface located 38 cm from a point source of 7943 Pa.

5.2.2 Pseudo-spectral time domain simulations

For the first configuration, which involves a layer of water and a layer of sand, it is possible to observe how the P-waves and S-waves propagate throughout the simulation in Figure 5.23. The main wave, when it hits the sand interface, generates shear waves. Of course, the compressional waves continue to travel within this new layer as well. It is interesting to note that these waves move faster than the shear waves. The final frame notably allows us to visualize this difference in speed, as the P-waves have completely disappeared (because they have already reached the end of the simulation grid), while the S-waves are still traveling through the same sand layer.

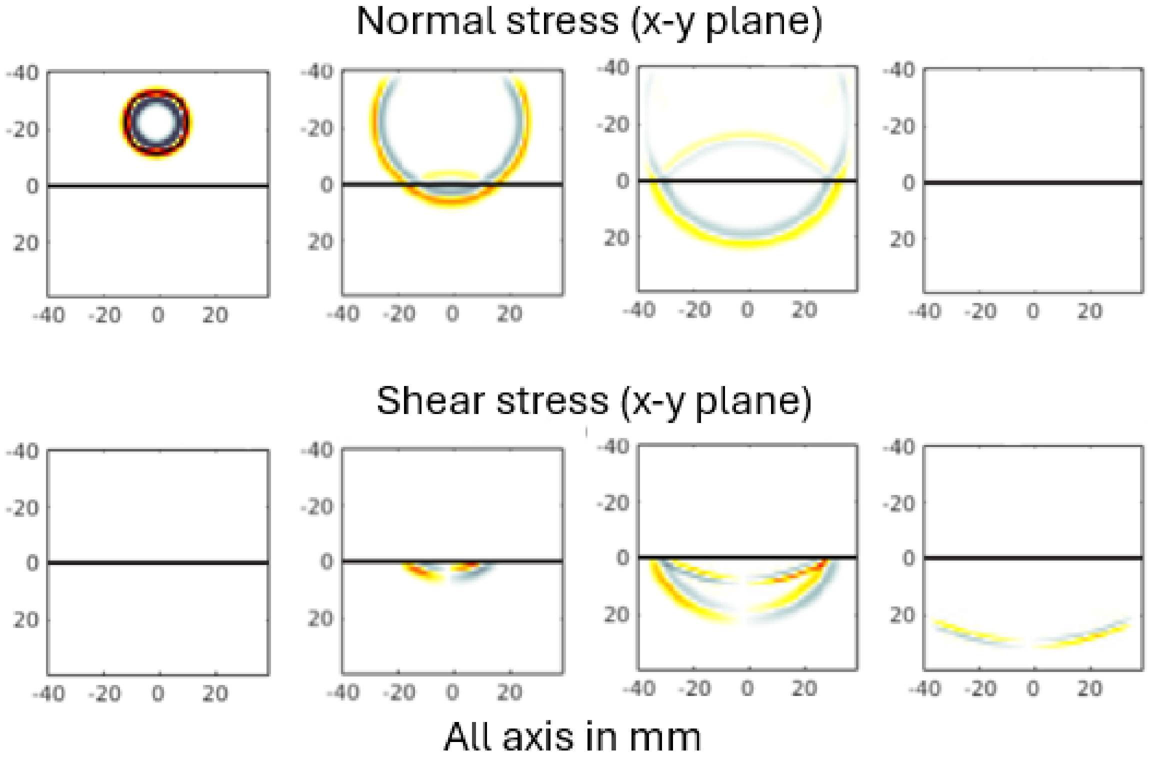

Figure 5.23: Time-lapse of the propagation of a 50 Pa wave within a layer of water and sand inside a 8*8*8 cm size grid.

If we now look at the filtered signal (to which we subtracted $H_i(t)$) received by the sensor, shown in Figure 5.24, we can observe a pressure variation around $3 \cdot 10^{-5}$ s. This pressure variation is, in fact, caused by the waves that travel back towards the sensor after reflecting between the interface of the water and sand layers.

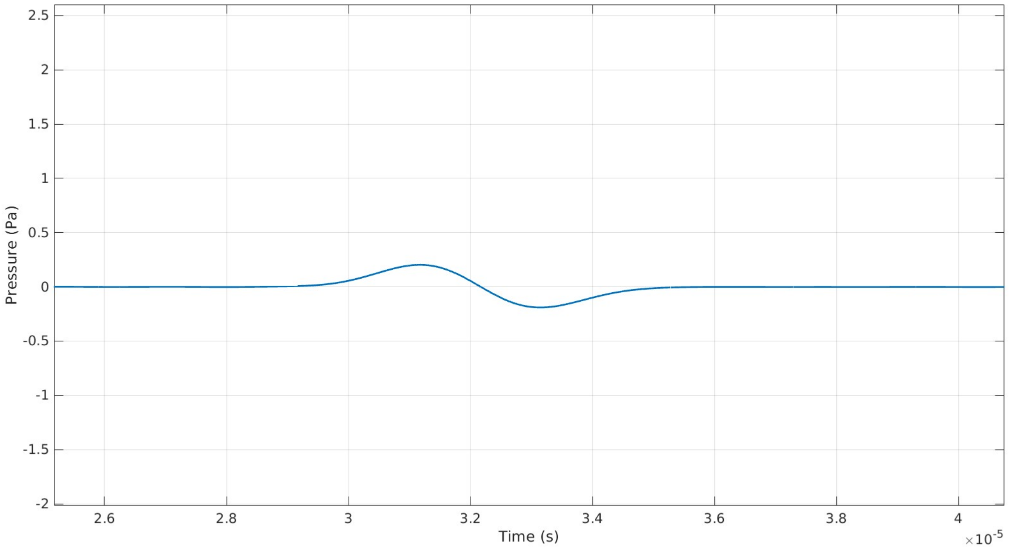

Figure 5.24: Filtered signal recorded by a monostatic sensor in a configuration involving a layer of water and a layer of sand.

The results of the configuration involving three layers, including a water layer, one resembling a mine, and finally a sand layer, are presented in Figures 5.25 and 5.26. The first one is once again a time lapse that allows for the visualization of the movement of both types of waves over time. A relatively interesting observation is that the shear waves that originate within the layer representing the mine move very quickly and in a rather complex manner. The propagation pattern resembling a semicircle, which was observed in the previous configuration when interacting with the sand (see Figure 5.23), is not the same. This is due to the relatively high speed of these waves within a layer exhibiting such physical characteristics. The transition of waves from the like-mine layer to the sand layer is quite weak and barely perceptible. It seems that they have more difficulty passing from one solid layer to another, whether for P waves or S waves. These waves appear to propagate more quickly.

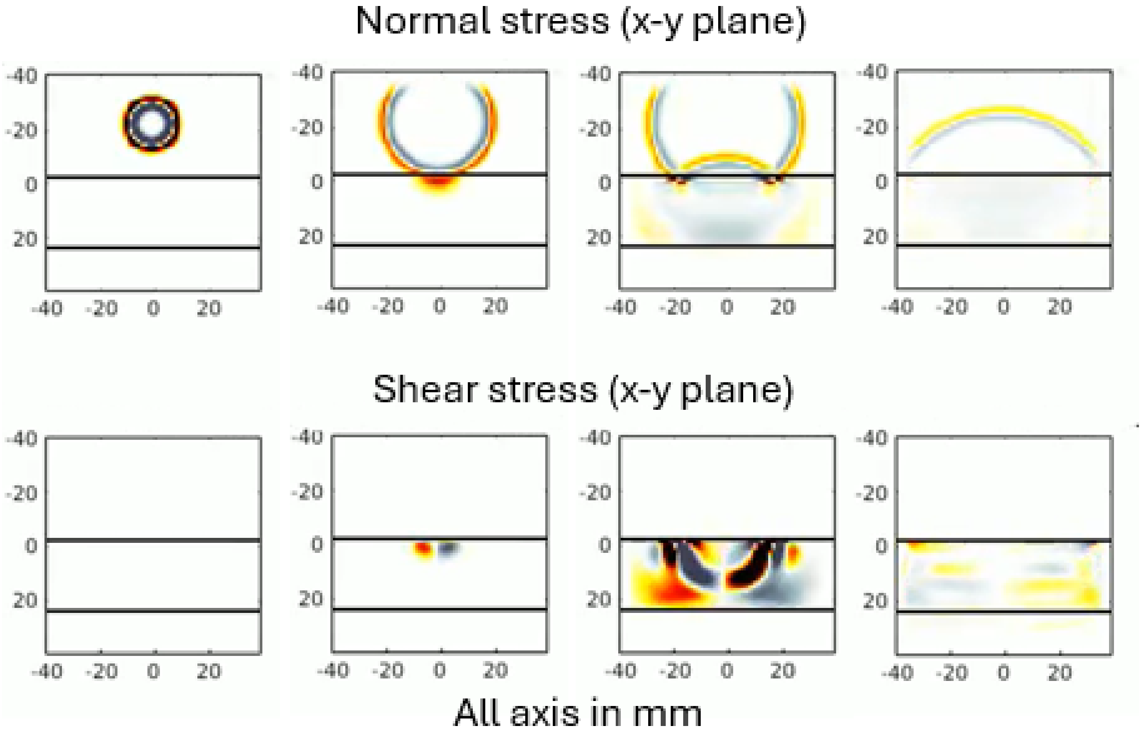

Figure 5.25: Time-lapse of the propagation of a 50 Pa wave within a layer of water, mine-like and sand. Grid size of 8*8*8 cm.

Figure 5.26, which shows the filtered signal (to which we subtracted $H_i(t)$) received by the sensor, also presents a pressure variation peak. This peak is relatively stronger than the one observed in the two-layer configuration for two reasons. The first is that the layer mimicking the mine appears to reflect the waves more effectively, and the second can be simply explained by the fact that the sensor is located slightly closer to the first reflection layer.

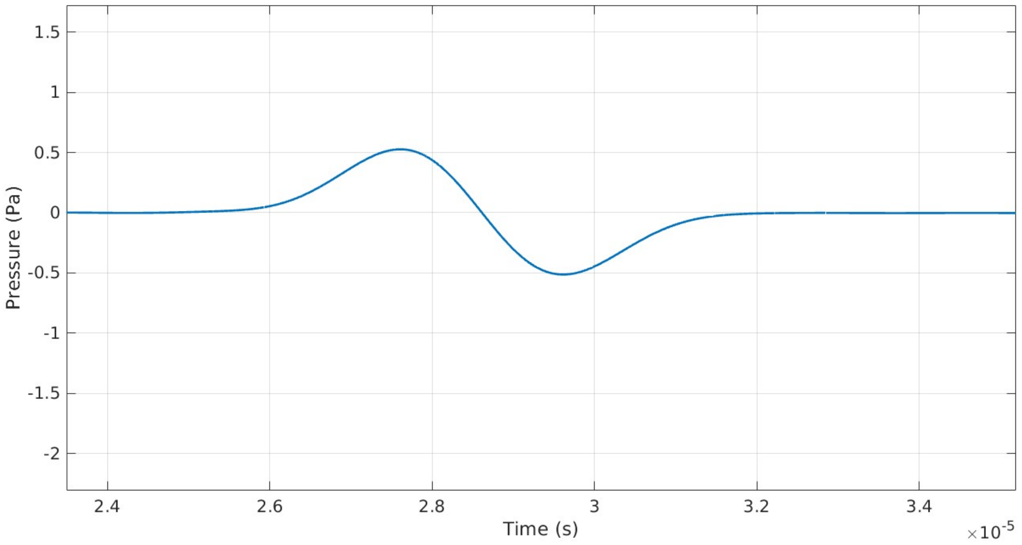

Figure 5.26: Filtered signal recorded by a monostatic sensor in a configuration involving a layer of water, a mine-like layer and a layer of sand.

Chapter 6

Discussion

6.1 Laboratory experiments

6.1.1 Gain function recovery

The gain recovery process therefore relies on an inverse modeling principle, which can lead to numerous errors. The method of recovering the gain may also seem somewhat subjective in its threshold setting approach, but the additional figures in the Appendix B prove that regardless of the threshold setting method, the coefficients R^2 are too low to conclude in any case that there is a linear model.

Figure 5.8, which enables obtaining normalized signals, is quite interesting to discuss because by dividing each signal by its attributed linear equation, we recover a striking similarity in the first part of the signal that even allows them to overlap. Thanks to this similar part, we can, in a way, compare the signals in their second half. A constant linear gain would have allowed drawing a line passing through all the tops of the first peaks related to the target reflection. Here, this is not the case. The different scaling of signals in their second half is almost entirely due to the y-intercept of the line equation.

In other words, a different constant seems to be applied to each signal almost entirely due to the y-intercept of the line equation. It could therefore be concluded that the applied gain is constant throughout the signal but increases as the distance between the object and the sensor increases. However, this claim is not proven for the last signal, where the gain applied to the signal is lower.

It appears that it is not possible to retrieve the gain that is automatically adjusted by the sensor because the gain changes without following any apparent logic. It may even be that the gain changes based on a concept of zones: thus, the applied gain would increase as the distance increases, and in other distance intervals or zones (whether larger or smaller), it would decrease.

In addition to the changes observed between measurements within the same interval, another source of variability must be introduced. This refers to the difference observed when two signals are taken at the same distance and in an entirely identical configuration. In fact, Figure 6.1 shows two measurements taken at different times (a week apart) for similar distances. The adjusted parameters and sensor configuration remain the same. However, although the sensor should return the same signal, the result differs. Indeed, the newly measured distance is no longer 445 mm, but 870 mm (see the saturated peak). A significant peak still appears near the distance that should be returned. Thus, under perfectly similar conditions (even though the temperature varies by a few tenths of a degree), the signals returned for the same configuration differ, and the gain is adjusted in an incomprehensible manner.

In the case of the Ping2 sensor, the gain seems to change for reasons other than distance. Other parameters, entirely beyond the user's control, must play a role in signal recovery. This sensor is designed to return a distance measurement as reliably as possible, regardless of the cost (manipulation and adjustment of the reflected signal). Its use in the context of this thesis seems to exceed the sensor's capabilities when it comes to the quality of the recovered signals.

Moreover, the inability to retrieve decimal data significantly limits the precision of the measurements, making it challenging to apply advanced processing methods.

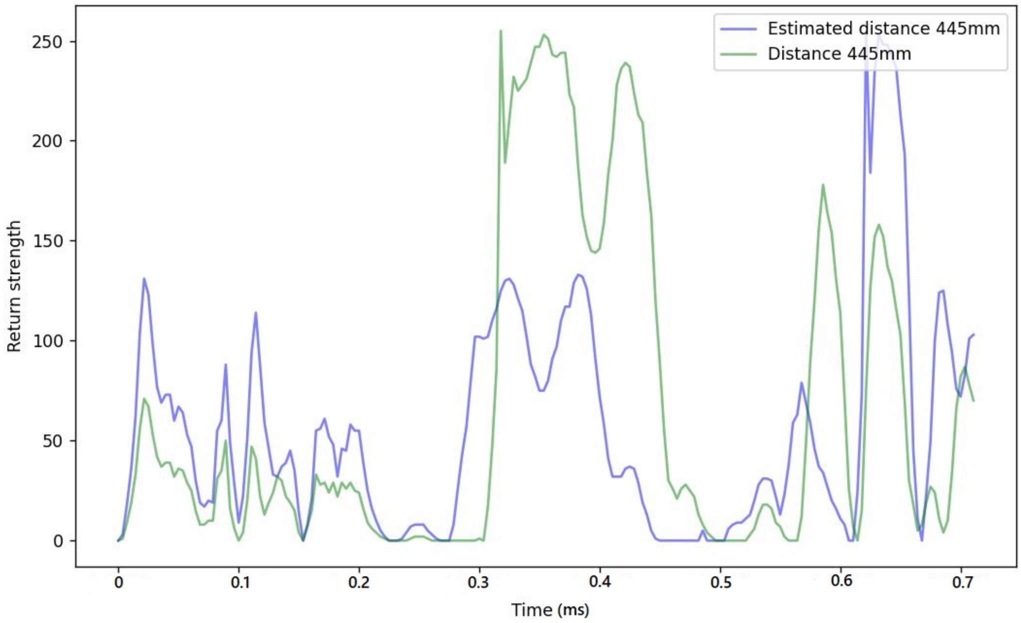

Figure 6.1: Graph of signals returned for the same configuration one week apart (11/19-2024 to 11/26-2024).

6.1.2 Perfect acoustic reflector (PAR) configurations

When the gain goes from 0 to 5 the signal changes to the extent that the transducer no longer recognizes the air-water interface as the main target, but thinks that a multiple reflection is our new surface of reflection because it is more pronounced. This does not pose a problem since the signal recovered up to the real interface is no longer saturated. As mentioned previously, multiple reflections are most likely responsible for this confusion, as they are reported relatively periodically. These multiple reflections can be explained by waves that bounce off the air-water interface, hit the bottom of the tank, and return to the sensor but could also be waves that reflect off the device, go again to the water-air interface, and come for second time to the sonar.

All the collected signals appear to be usable for comparison with the numerical simulations (here, only the distances of 30 cm and 38 cm can be compared). However, the residual issue is that the gain applied to these different measurements remains unknown, making it impossible to adjust them. As a result, the comparison is not feasible (not to mention that the simulations provide a pressure measurement compared to a return strength measurement for the sensor).

6.1.3 B-scans scenarios

Analysis of the B-scan results reveals a number of areas for improvement but also some interesting observations. The gain of 5 chosen when configuring the sensor introduces significant noise and vertical artifacts that complicate interpretation of the results and prevent accurate detection of the bottom of the reservoir.

The change in the type of surface from Plexiglas to sand observed in Figure 5.11 indicates that the sand absorbs and scatters part of the signal, making the bottom less visible. This can be explained by a different reflection or absorption coefficient. This absorption is typical for granular materials, which are less homogeneous than Plexiglas. Secondly, the addition of a relatively large target, such as a brick, produces additional reflections, confirming its presence with high-intensity patterns. These results could demonstrate that the sonar sensor is sensitive to the materials present and their interfaces.

There are also important technical limitations related to the experiment that need to be improved. The acceleration and deceleration phases of the sensor make it difficult to assign an exact position to each ping in terms of time or distance, which is a notable limitation. However, this situation is close to real-life conditions for bathymetry or other types of measurement (including the way the SBSS moves and collects data), where the speed of a boat or robot conducting the surveys is not always constant. In practice, these vehicles often take continuous measurements, and variations in sensor position and angle due to water agitation (waves, currents) influence the readings, adding a complexity similar to that observed in the laboratory (although they are equipped with differential GPS for positioning each measurement, regardless of the velocity variations). In addition, the motion of the vessel and the position of the sonar projector relative to the environment influence the quality of the data [Bjørnø et al., 2017]. However, acceleration and deceleration remain a concern. To improve these experiments in the future, it would be beneficial to use a sensor capable of accurately knowing the position of each ping in its environment. This would correct inaccuracies due to speed variations and improve the spatial resolution of the B-scans, as it is not known whether these nonuniform phases affect the reception of the signal by the receiver.

Another limiting factor is the size of the water tank used. With a volume of one cubic meter, the tank is relatively too small for this type of experiment. Even if the measurements are carried out in the far field, the confinement of space favors multiple reflections off the walls and rounded dome, introducing noise and additional disturbances. These reflections can disrupt the main signal and complicate the analysis of the results.

Finally, one of the last areas for improvement concerns the distribution and control of the height of the sand. In experiments, it is difficult to obtain a perfectly uniform surface once the sand is immersed, resulting in variable sand heights that affect signal reflections. A method allowing a more homogeneous sand distribution would improve the reliability of the measurement and the reproducibility of the results.

6.2 Numerical simulations

6.2.1 Green's function and free field simulations

For configurations with a water-air interface located at 30 cm and 38 cm, the simulations yield the Green's function for 2 different distances. Thus, these two configurations could have been compared with the results obtained in the laboratory, for the same distances, if the gain was removed, to calibrate the Ping2 transducer.

The results show marked variations in the amplitudes of the returned signals. These differences are directly related to the distance traveled by the waves and the reflection at the interface. The results show a temporal shift in the pressure peaks when the interface is moved, reflecting the proportional increase in the round-trip travel time. These observations corroborate the accuracy of the modeling.

In a free field configuration, the absence of a reflective interface highlights only the intrinsic properties of the source and the sensor. The signals recorded in this configuration serve as a reference to isolate parasitic contributions (such as internal reflections and transmissions of the transducer, modeled by $H_i(\omega)$. The measurements can be corrected using $H_i(\omega)$, which provides a more accurate representation of wave-medium interactions.

6.2.2 Pseudo-spectral time domain simulations

In simulations involving different layers, PSTD functions highlight the differences in wave propagation between a fluid and a solid. The introduction of a layer resembling a mine is an excellent exercise to understand how the waves received by the sensor are affected. The more complex configuration, including a layer simulating a mine between water and sand, reveals reflections and transmissions specific to the physical and acoustic characteristics of the "mine."

However, these simulations are limited by the size of the computational grids, preventing direct comparison with measurements conducted at the laboratory scale (although the configurations are not identical, except for the setup involving only a sand layer). This part of the simulation is therefore purely exploratory, although the results demonstrate the relevance of the PSTD functions for analyzing realistic scenarios.

The use of the k-wave package proves to be highly useful for simulating all acoustic phenomena occurring in a given situation. That said, this package has its limitations. In fact, it is not always suitable for every scenario encountered. The shape of the source and the way waves are initiated do not fully conform to the real tests conducted in the laboratory. Furthermore, k-wave does not directly provide a monostatic configuration, which can introduce biases into the results obtained. Finally, the use of PSTD functions simulates scenarios that again differ from those encountered in laboratories due to several factors, such as the inability to reproduce specific object shapes or the fact that the simulated layers are homogeneous throughout and insufficiently representative of natural layers.

Chapter 7

Conclusion and prospects

7.1 Conclusion

The aim of applying the GPR methodology, specifically designed for electromagnetic waves, to acoustic waves is an ambitious goal that, to the best of our knowledge, has never been tackled before. The purpose of this thesis was to provide all the elements necessary to achieve this adaptation. Unfortunately, the overall goal was not reached. This can be explained by several factors.

One of the most limiting factors in this thesis was the choice of transducer. This choice was made because of its ease of access, programming, and configuration. However, the applied dynamic gain function is not known and could not be retrieved. Additionally, the system only returns integer values, without any decimals, making this sensor unsuitable for this type of experiment.

The inability to retrieve the gain function and therefore the raw signal, makes it impossible to compare the results obtained through numerical simulations using the k-wave package. Thus, it is not possible to compare the simulated signals using the PAR at different distances with those collected in the laboratory under the same configuration.

However, these same numerical simulations provide consistent results that help to better understand how acoustic waves propagate. Simulations using the k-wave package also allowed us to obtain the Green's function for the 3D propagation of compressional waves in multilayered media, which was difficult to find in its analytical form in the literature.

In addition, these simulations allowed us to numerically recover one of the transfer functions $H_i(\omega)$ following the retrieval of signals under free field conditions. Unfortunately, the inability to compare the simulated signals with those collected under experimental conditions means that the transfer function $H_i(\omega)$) cannot be used for further signal processing (even if the results had coincided). It is worth noting, however, that measurements to retrieve the transfer function $H_i(\omega)$ under laboratory conditions would have been complicated, as it requires subtracting the signal under free field conditions. In fact, the water tank used is too small and would not have allowed such a configuration due to the numerous multiple reflections caused by its size.

Finally, the different scenarios, whether conducted in the laboratory or through numerical simulations, are relatively interesting, as they implement the concept of layers with varying acoustic and physical properties, while also introducing the notion of a target. The results of the B-scan were intended to serve as a database from which the filtered signal could be retrieved after applying the methodology to enhance the signals.

7.2 Prospects

For future perspectives, many details need to be improved in order to apply the GPR methodology to sonar signals. Indeed, one of the first areas for improvement would be to use a sensor that returns signals from which the acoustic pressure can be easily retrieved directly, rather than values for return forces set by the manufacturer. The goal is also to be able to easily recover the applied gain function or simply be able to disable the offset. Additionally, the experimental setup should ideally be adjusted to include a much larger water tank, such as a swimming pool, a lake, or even the sea, to enable measurements under free field conditions.

Regarding the use of the k-wave package, although it allowed for accurate simulation of certain configurations, the inability to replicate the shape of a specific object, such as a mine in this case, is a significant limitation. Another, more recent numerical simulation software in the library, which takes this type of parameter into account, would be a real improvement.

One of the final points to improve concerns the B-scan sections. These should be performed without acceleration or deceleration phases, or alternatively, the measurements could be synchronized with the scanner, as is done with GPR. They should also involve targets that closely resemble real mines. Furthermore, ideally, the target should be submerged much deeper than was done in the current setup, in order to later retrieve the burial depth of the object.

Bibliography

Douglas A Abraham. *Underwater acoustic signal processing: modeling, detection, and estimation.* Springer, 2019.

Michael A Ainslie. *Principles of sonar performance modelling*, volume 707. Springer, 2010.

Victor C Anderson. Sound scattering from a fluid sphere. *The Journal of the Acoustical Society of America*, 22(4):426–431, 1950.

Leif Bjørnø, Thomas Neighbors, and David Bradley. *Applied underwater acoustics.* Elsevier, 2017.

BlueRobotics Community. Interpretation of sonar raw data, 2023. URL `https://discuss.bluerobotics.com/t/interpretation-of-sonar-raw-data/11722/11`.

Leonid Maksimovich Brekhovskikh and Yu P Lysanov. *Fundamentals of ocean acoustics.* Springer Science & Business Media, 2006.

Jonathan M Bull, Martin Gutowski, Justin K Dix, Timothy J Henstock, Peter Hogarth, Timothy G Leighton, and Paul R White. Design of a 3d chirp sub-bottom imaging system. *Marine Geophysical Researches*, 26:157–169, 2005.

David S Burnett. Computer simulation for predicting acoustic scattering from objects at the bottom of the ocean. *Acoustics Today*, 11(1):28–36, 2015.

Brian R Calder and Larry A Mayer. Automatic processing of high-rate, high-density multibeam echosounder data. *Geochemistry, Geophysics, Geosystems*, 4(6), 2003.

José M Carcione. *Wave fields in real media: Wave propagation in anisotropic, anelastic, porous and electromagnetic media.* Elsevier, 2007.

Peter C Chu. Mine impact burial prediction from one to three dimensions. 2009.

Charles S. Clay and Herman Medwin. *Acoustical Oceanography: Principles and Applications.* Wiley-Interscience, 1977.

Yang Cong, Changjun Gu, Tao Zhang, and Yajun Gao. Underwater robot sensing technology: A survey. *Fundamental Research*, 1(3):337–345, 2021.

Weicheng Cui. An overview of submersible research and development in china. *Journal of Marine Science and Application*, 17(4):459–470, 2018.

Carlos A De Moura and Carlos S Kubrusly. The courant–friedrichs–lewy (cfl) condition. *AMC*, 10 (12):45–90, 2013.

Demanet. Mit opencourseware, intoduction to numerical analysis. `https://ocw.mit.edu/courses/18-330-introduction-to-numerical-analysis-spring-2012/pages/instructor-insights/`, note = Accessed: 2024-08-16, 2012.

Heidi M Dierssen and Albert E Theberge. Bathymetry: assessment. In *Coastal and Marine Environments*, pages 175–184. CRC Press, 2020.

Mariia Dmitrieva, Matias Valdenegro-Toro, Keith Brown, Gary Heald, and David Lane. Object classification with convolution neural network based on the time-frequency representation of their echo. In *2017 IEEE 27th International Workshop on Machine Learning for Signal Processing (MLSP)*, pages 1–6. IEEE, 2017.

Nicholas Dourado. Sediment laden ice detection using broadband acoustic backscattering measurements from calibration targets in ice. 2015.

J. J. Faran. Sound scattering by solid cylinders and spheres. *The Journal of the Acoustical Society of America*, 23:405–418, 1951.

Roberta Ferretti, Elisa Fumagalli, Massimo Caccia, and Gabriele Bruzzone. Seabed classification using a single beam echosounder. In *OCEANS 2015 - Genova*, pages 1–5, 2015. doi: 10.1109/OCEANS-Genova.2015.7271709.

Bengt Fornberg and David M Sloan. A review of pseudospectral methods for solving partial differential equations. *Acta numerica*, 3:203–267, 1994.

Iraklis Giannakis, Antonios Giannopoulos, and Craig Warren. A realistic fdtd numerical modeling framework of ground penetrating radar for landmine detection. *IEEE journal of selected topics in applied earth observations and remote sensing*, 9(1):37–51, 2015.

Martin Gutowski, Jon Bull, Tim Henstock, Justin Dix, Peter Hogarth, Tim Leighton, and Paul White. Chirp sub-bottom profiler source signature design and field testing. *Marine Geophysical Researches*, 23:481–492, 2002.

Roy Edgar Hansen. Synthetic aperture sonar technology review. *Marine Technology Society Journal*, 47(5):117–127, 2013.

Roy Edgar Hansen, Hayden John Callow, Torstein Olsmo Sabo, and Stig Asle Vaksvik Synnes. Challenges in seafloor imaging and mapping with synthetic aperture sonar. *IEEE Transactions on geoscience and Remote Sensing*, 49(10):3677–3687, 2011.

Michael P Hayes and Peter T Gough. Synthetic aperture sonar: A review of current status. *IEEE journal of oceanic engineering*, 34(3):207–224, 2009.

Ricardo Oliver Hein Hoernig. *Green's functions and integral equations for the Laplace and Helmholtz operators in impedance half-spaces*. PhD thesis, Ecole Polytechnique X, 2010.

Stanisław Hożyń. A review of underwater mine detection and classification in sonar imagery. *Electronics*, 10(23):2943, 2021.

Shih-Jung Hsu, Yagız Efe Bayiz, Pan Liu, and Bo Cheng. An insect tether system using magnetic levitation: Development, analysis and feedback control. In *Dynamic Systems and Control Conference*, volume 50695, page V001T09A004. American Society of Mechanical Engineers, 2016.

Lloyd C Huff. High-resolution multi-beam focussed side scan sonar. *Proceedings of the Institute of Acoustics, Acoustic Classification and Mapping of the Seabed*, 15(Pt 2), 1993.

John E Hughes Clarke. Multibeam echosounders. *Submarine geomorphology*, pages 25–41, 2018.

Camilo A Hurtado Erasso. Mi tercera poster session, 2024. URL `https://camihurs.biz/2024/11/17/mi-tercera-poster-session/`. Accessed: 2025-01-02.

Finn B Jensen, William A Kuperman, Michael B Porter, Henrik Schmidt, and Alexandra Tolstoy. *Computational ocean acoustics*, volume 2011. Springer, 2011.

Steven G Kargl, Kevin L Williams, and Eric I Thorsos. Synthetic aperture sonar imaging of simple finite targets. *IEEE Journal of Oceanic Engineering*, 37(3):516–532, 2012.

Hans Petter Knudsen. Long-term evaluation of scientific-echosounder performance. *ICES Journal of Marine Science*, 66(6):1335–1340, 2009.

Sébastien Lambot and Frédéric André. Full-wave modeling of near-field radar data for planar layered media reconstruction. *IEEE Transactions on Geoscience and Remote Sensing*, 52(5):2295–2303, 2014.

Sébastien Lambot, Evert C Slob, Idesbald van den Bosch, Benoit Stockbroeckx, and Marnik Vanclooster. Modeling of ground-penetrating radar for accurate characterization of subsurface electric properties. *IEEE transactions on geoscience and remote sensing*, 42(11):2555–2568, 2004.

Olga Lopera, Evert C Slob, Nada Milisavljevic, and Sbastien Lambot. Filtering soil surface and antenna effects from gpr data to enhance landmine detection. *IEEE Transactions on Geoscience and Remote Sensing*, 45(3):707–717, 2007.

Xavier Lurton. *An introduction to underwater acoustics: principles and applications*. Springer Science & Business Media, 2002.

Xavier Lurton. *An Introduction to Underwater Acoustics: Principles and Applications*. Springer, 2010.

David Marx, Matt Nelson, Enson Chang, Walt Gillespie, Angela Putney, and Kieffer Warman. An introduction to synthetic aperture sonar. In *Proceedings of the Tenth IEEE Workshop on Statistical Signal and Array Processing (Cat. No. 00TH8496)*, pages 717–721. IEEE, 2000.

Larry Mayer, Martin Jakobsson, Graham Allen, Boris Dorschel, Robin Falconer, Vicki Ferrini, Geoffroy Lamarche, Helen Snaith, and Pauline Weatherall. The nippon foundation—gebco seabed 2030 project: The quest to see the world's oceans completely mapped by 2030. *Geosciences*, 8(2):63, 2018.

Larry A Mayer. Frontiers in seafloor mapping and visualization. *Marine Geophysical Researches*, 27: 7–17, 2006.

Jim McDonald. Uxo detection and characterization in the marine environment. *ESTCP Project MM-0324 Final Report*, 2008.

P McGrane, IV Konoplev, K Ronald, AW Cross, and ADR Phelps. Experimental and theoretical study of constructive and destructive wave interference in a coaxial 1d bragg structure. In *Infrared and Millimeter Waves, Conference Digest of the 2004 Joint 29th International Conference on 2004 and 12th International Conference on Terahertz Electronics, 2004.*, pages 177–178. IEEE, 2004.

Yan Pailhas, Yvan Petillot, Chris Capus, and Reg Hollett. Study, design and concept of low frequency sas. *Proceedings of the Institute of Acoustics*, 32(01), 2010.

Xiang Pan, Qing Chen, Wen Xu, Jianlong Li, and Feng Sun. Shallow-water wideband low-frequency synthetic aperture sonar for an autonomous underwater vehicle. *Ocean Engineering*, 118:117–129, 2016.

Allan D Pierce. *Acoustics: an introduction to its physical principles and applications*. Springer, 2019.

Ruth MK Plets, Justin K Dix, Jon R Adams, Jonathan M Bull, Timothy J Henstock, Martin Gutowski, and Angus I Best. The use of a high-resolution 3d chirp sub-bottom profiler for the reconstruction of the shallow water archaeological site of the grace dieu (1439), river hamble, uk. *Journal of Archaeological Science*, 36(2):408–418, 2009.

Dhilsha Rajapan, PM Rajeshwari, and Shijo Zacharia. Importance of underwater acoustic imaging technologies for oceanographic applications–a brief review. *OCEANS 2022-Chennai*, pages 1–6, 2022.

Lord Rayleigh. *The Theory of Sound*. Macmillan, London, 1877.

Blue Robotics. Ping viewer documentation, 2024. URL `https://docs.bluerobotics.com/ping-viewer/`.

Francisco J Sánchez-Sesma and Ursula Iturrarán-Viveros. Propagation of elastic waves: Fundamentals. *Encyclopedia of Solid Earth Geophysics*, pages 1283–1291, 2021.

Mahmoud Mohamed Selim Saleh. Body waves. In *Encyclopedia of Solid Earth Geophysics*, pages 37–44. Springer, 2021.

Arthur Sluÿters, Sébastien Lambot, Jean Vanderdonckt, and Santiago Villarreal-Narvaez. Analysis of user-defined radar-based hand gestures sensed through multiple materials. *IEEE Access*, 12: 27895–27917, 2024.

Peter Staelens. *Defining and modeling the limits of high-resolution underwater acoustic imaging*. PhD thesis, Ghent University, 2009.

Kai Sun, Weicheng Cui, and Chi Chen. Review of underwater sensing technologies and applications. *Sensors*, 21(23):7849, 2021.

Olga Lucia Lopera Tellez, Alexander Borghgraef, and Eric Mersch. The special case of sea mines. *Mine Action—The Research Experience of the Royal Military Academy of Belgium; Beumier, C., Closson, D., Lacroix, V., Milisavljevic, N., Yvinec, Y., Eds*, pages 251–279, 2017.

A Tesei, JA Fawcett, and R Lim. Physics-based detection of man-made elastic objects buried in high-density-clutter areas of saturated sediments. *Applied Acoustics*, 69(5):422–437, 2008.

Anh Phuong Tran, Craig Warren, Frédéric André, Antonios Giannopoulos, and Sebastien Lambot. Numerical evaluation of a full-wave antenna model for near-field applications. *Near Surface Geophysics*, 11(2):155–165, 2013.

Bradley Treeby and Ben Cox. k-wave user documentation, 2024. URL `http://www.k-wave.org/documentation.php`. Accessed: 2024-12-30.

Robert J. Urick. *Principles of Underwater Sound*. McGraw-Hill, 1983.

Crescenzo Violante. Acoustic remote sensing for seabed archaeology. In *Proceedings of the IMEKO TC4 International Conference on Metrology for Archaeology and Cultural Heritage, Trento, Italy*, pages 22–24, 2020.

SM Walley and JE Field. Elastic wave propagation in materials. *Reference Module in Materials Science and Materials Engineering*, 1:1–7, 2016.

Anne-Cathrin Wölfl, Helen Snaith, Sam Amirebrahimi, Colin W Devey, Boris Dorschel, Vicki Ferrini, Veerle AI Huvenne, Martin Jakobsson, Jennifer Jencks, Gordon Johnston, et al. Seafloor mapping–the challenge of a truly global ocean bathymetry. *Frontiers in Marine Science*, 6:283, 2019.

Ziyin Wu, Fanlin Yang, and Yong Tang. *High-resolution seafloor survey and applications*. Springer, 2021.

Appendix A

Fundamental concepts

Bandpass

A bandpass signal is characterized by its spectral content being restricted to a specific frequency range f_c. The mathematical expression for a bandpass signal is [Abraham, 2019]:

$$s(t) = a(t)\cos(2\pi f_c t + \phi(t)),$$

where $a(t)$ is the amplitude and $\phi(t)$ is the phase. Bandpass signals can be classified as narrowband or broadband.

Narrowband signals

A signal is classified as narrowband if its bandwidth W is significantly smaller than its center frequency f_c. The condition is expressed as:

$$\frac{W}{f_c} \ll 1.$$

Broadband signals

In contrast, a broadband signal (also known as wideband) has a bandwidth W that is large relative to its center frequency f_c. This can be represented as:

$$\frac{W}{f_c} \gg 1.$$

Bulk modulus

The bulk modulus (κ_0) is a mechanical property of materials that describes their resistance to volumetric compression. It is defined as:

$$\kappa_0 = -V\frac{\partial P}{\partial V},$$

where P is the pressure and V the volume. As said earlier, the bulk modulus is directly related to the speed of acoustic waves in the formula:

$$c = \sqrt{\frac{\kappa_0}{\rho_0}},$$

where ρ_0 is the density of the fluid and c is the speed of sound.

The table below presents typical values of κ_0 and the speed of acoustic waves (c) for different materials:

Material	κ_0 (Pa)	ρ_0 (kg/m^3)	c (m/s)
Air	1.42×10^5	1.2	343
Water	2.2×10^9	1000	1482
Sand (sediments)	6.0×10^7	1900	177
Metal (steel)	1.6×10^{11}	7800	5100

Table A.1: Values of bulk modulus and acoustic wave speed for common materials involved for underwater detection.

Appendix B

Additional figures

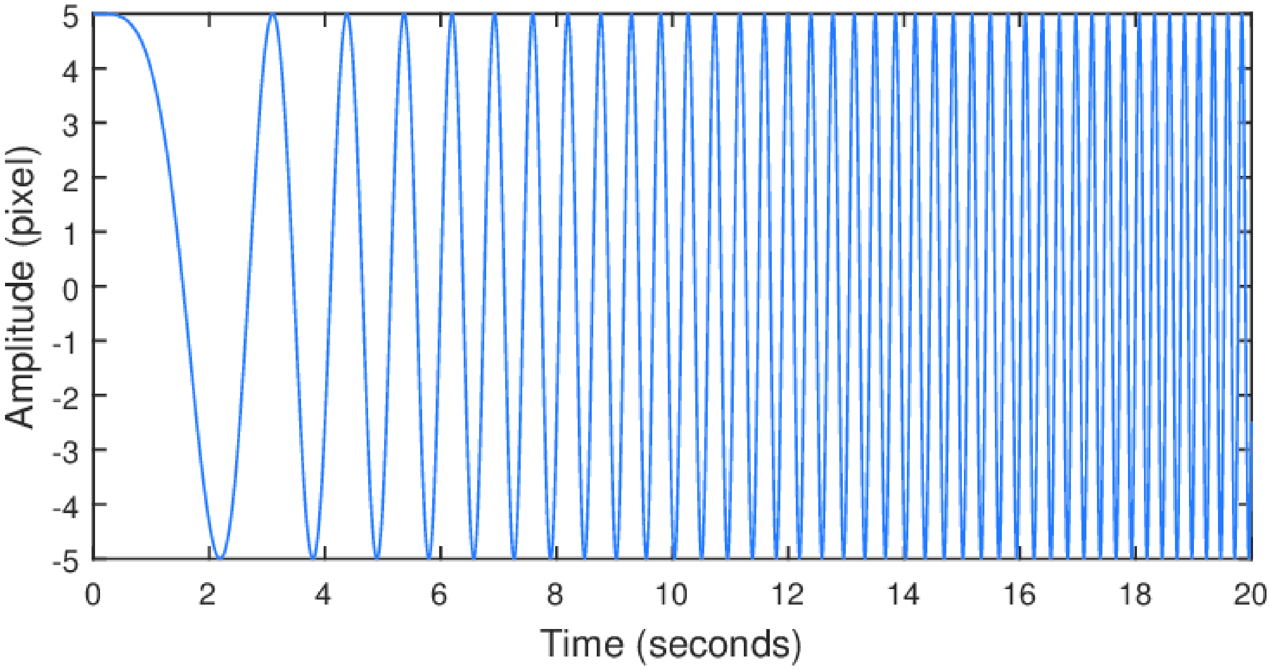

Figure B.1: Illustration of a Chirp signal from [Hsu et al., 2016].

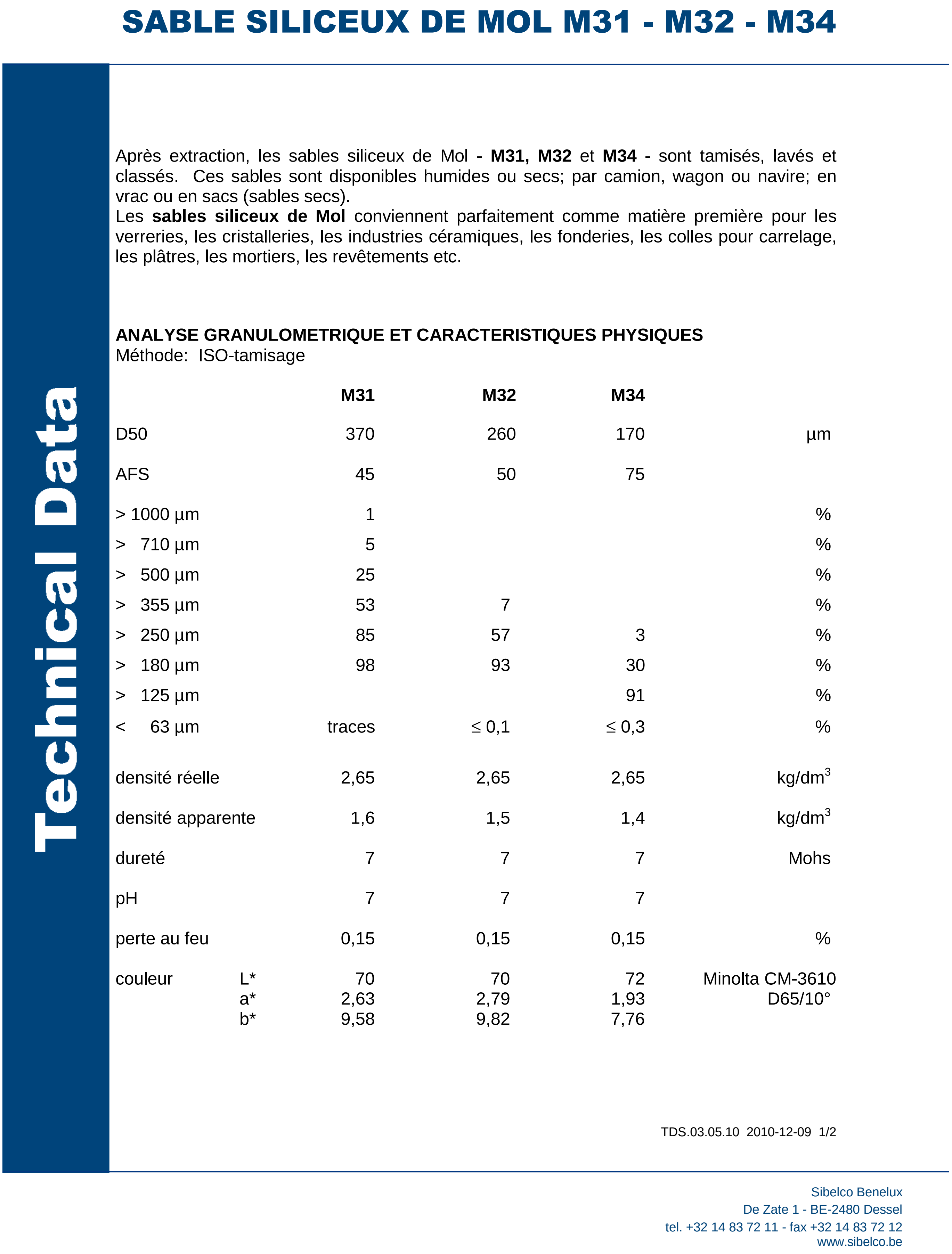

SABLE SILICEUX DE MOL M31 - M32 - M34

Technical Data

Après extraction, les sables siliceux de Mol - **M31, M32** et **M34** - sont tamisés, lavés et classés. Ces sables sont disponibles humides ou secs; par camion, wagon ou navire; en vrac ou en sacs (sables secs).
Les **sables siliceux de Mol** conviennent parfaitement comme matière première pour les verreries, les cristalleries, les industries céramiques, les fonderies, les colles pour carrelage, les plâtres, les mortiers, les revêtements etc.

ANALYSE GRANULOMETRIQUE ET CARACTERISTIQUES PHYSIQUES
Méthode: ISO-tamisage

		M31	**M32**	**M34**	
D50		370	260	170	µm
AFS		45	50	75	
> 1000 µm		1			%
> 710 µm		5			%
> 500 µm		25			%
> 355 µm		53	7		%
> 250 µm		85	57	3	%
> 180 µm		98	93	30	%
> 125 µm				91	%
< 63 µm		traces	≤ 0,1	≤ 0,3	%
densité réelle		2,65	2,65	2,65	kg/dm^3
densité apparente		1,6	1,5	1,4	kg/dm^3
dureté		7	7	7	Mohs
pH		7	7	7	
perte au feu		0,15	0,15	0,15	%
couleur	L*	70	70	72	Minolta CM-3610
	a*	2,63	2,79	1,93	D65/10°
	b*	9,58	9,82	7,76	

TDS.03.05.10 2010-12-09 1/2

Sibelco Benelux
De Zate 1 - BE-2480 Dessel
tel. +32 14 83 72 11 - fax +32 14 83 72 12
www.sibelco.be

Figure B.2: Technical data of the sand used

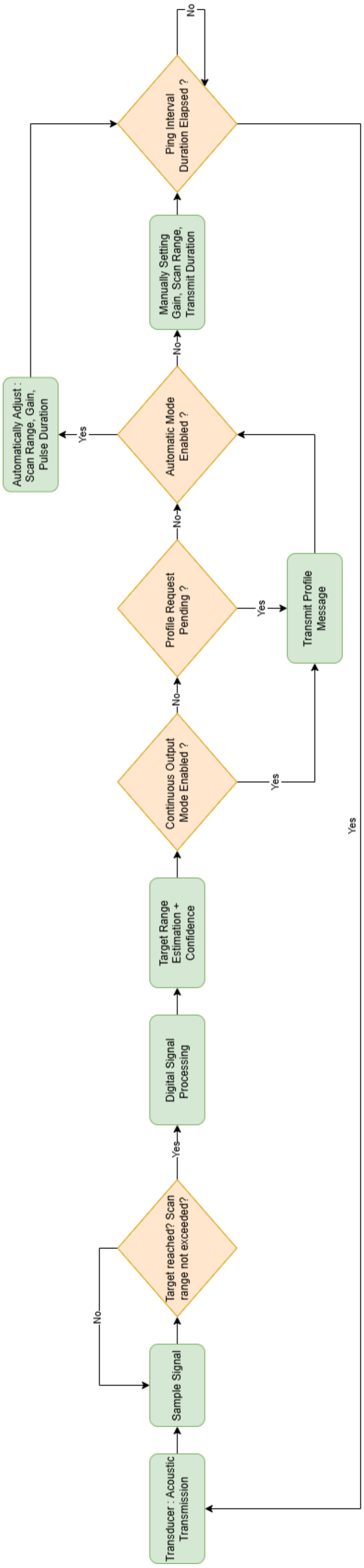

Figure B.3: Diagram of transducer operation once the signal has been sent.

Another gain function acquisition method

The previous method used to attempt to retrieve the gain function is detailed below. It has deliberately not been presented as it is considered less objective. The following steps explain the method applied on the same distance interval (429 to 715 mm):

- Begin by defining a reference signal, which should be the smallest distance measured by the sensor (429 mm).

- Next, independently take the other signals and divide them by this previously set reference signal.

- Focus on the result of the division and target only relatively stable values. To achieve this, set an acceptable threshold based on the smallest undefined value in the division graph, representing the smallest point of discontinuity where the division tends toward an infinite or undefined value.

- Once this threshold is determined and the values are filtered, a linear model can be fitted, assuming the gain follows a linear adjustment over time.

- Divide the raw signals by the corresponding linear relationship.

The results are presented here (note that the 625 mm profile data is not removed):

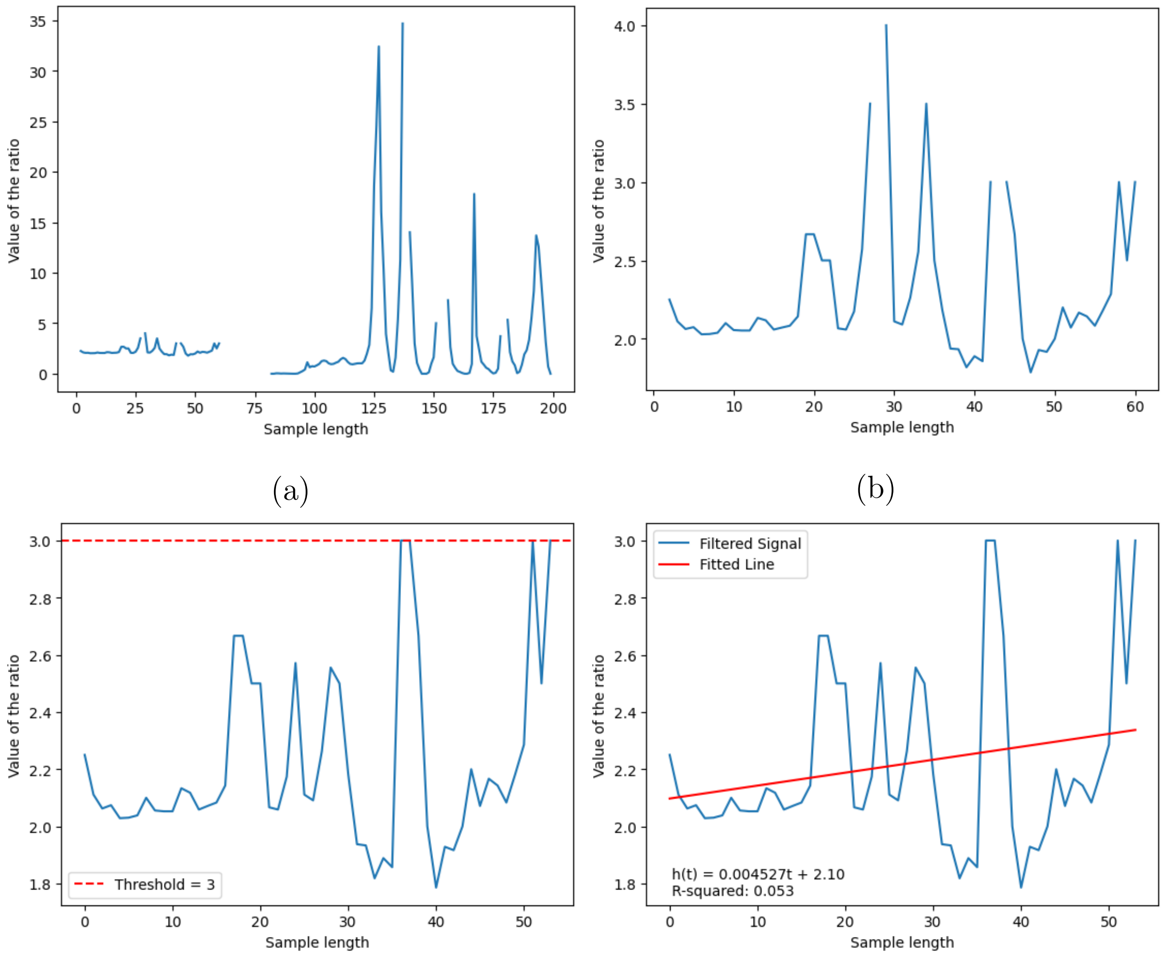

(a) (b)

(c) (d)

Figure B.4: (a) Graph of the ratio value between the 484 mm signal and the 429 mm reference signal. (b) Focus on the first part of the signal, corresponding to the ringing signal. (c) Filtering the data according to the smallest discontinuity value encountered. (d) Plotting the straight line of the linear model on the filtered values.

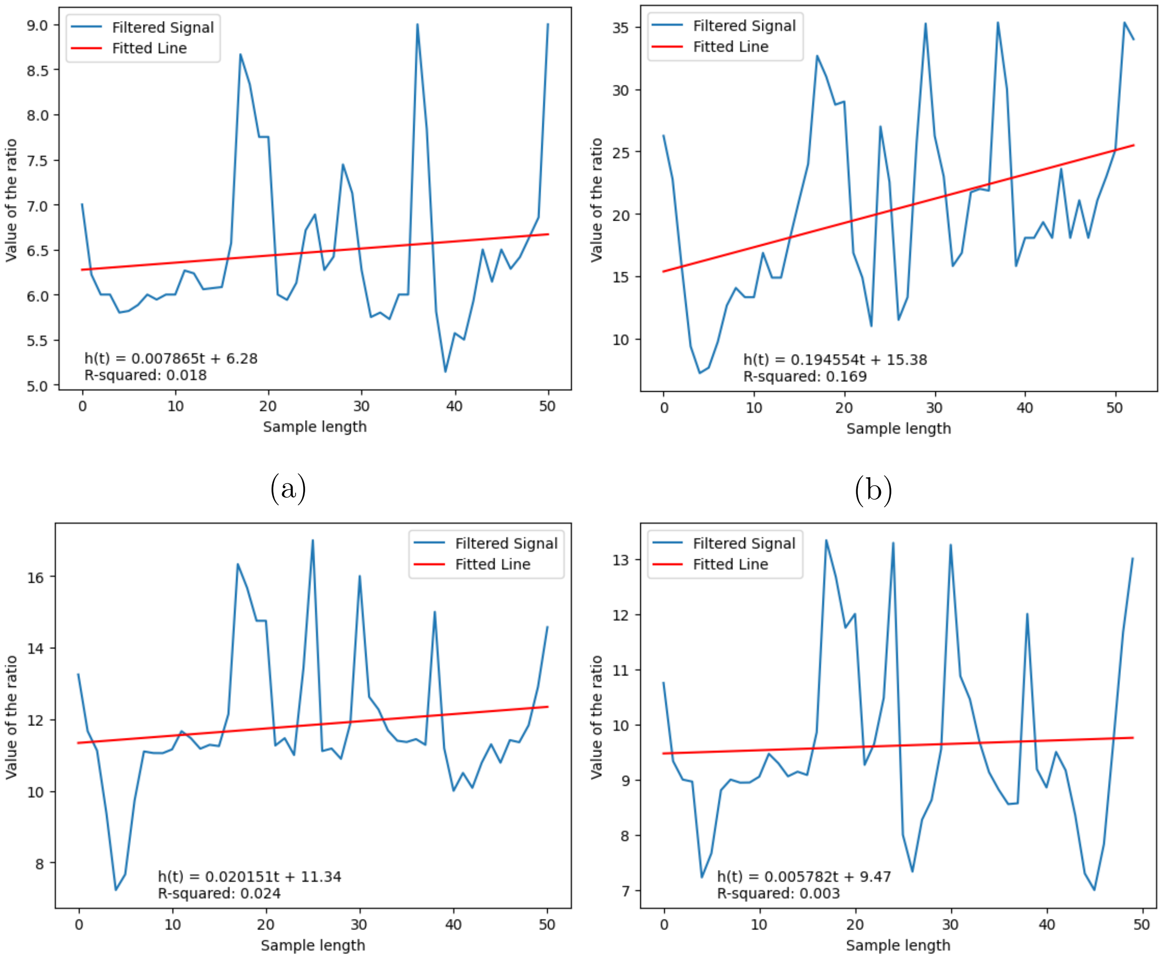

(a) (b) (c) (d)

Figure B.5: (a) Plotting the straight line of the linear model on the filtered values of the 560 mm distance measurement, (b) on the filtered values of the 625 mm distance measurement, (c) on the filtered values of the 675 mm distance measurement, (d) on the filtered values of the 715 mm distance measurement.

Appendix C

Codes

Ping2 codes

The code for Ping2 data acquisition is available below:

```
# simplePingExample.py
from brping import Ping1D
import time
import argparse
import pandas as pd
import os
import struct
from builtins import input

# Parse command-line arguments for device configuration
parser = argparse.ArgumentParser(description="Ping Python library example.")
parser.add_argument(’--device’, action="store", type=str, help="Ping device port (e.g., /dev/ttyUSB0)")
parser.add_argument(’--baudrate’, action="store", type=int, default=115200, help="Ping device baudrate (default: 115200)")
parser.add_argument(’--udp’, action="store", type=str, help="Ping UDP server (e.g., 192.168.2.2:9090)")
args = parser.parse_args()

# Ensure either a device or UDP is specified
if not args.device and not args.udp:
    parser.print_help()
    exit(1)

# Initialize the Ping device
myPing = Ping1D()
if args.device:
    myPing.connect_serial(args.device, args.baudrate)
elif args.udp:
    host, port = args.udp.split(’:’)
    myPing.connect_udp(host, int(port))

if not myPing.initialize():
    print("Failed to initialize Ping!")
    exit(1)

print("------------------------------------")
print("Starting Ping..")
print("Press CTRL+C to exit")
print("------------------------------------")

input("Press Enter to continue...")
```

```
# Initialize a list to store profile data
profile_data_list = []

# Function to decode profile_data from bytes to a list of integers
def decode_profile_data(profile_data_bytes):
    return list(struct.unpack(’<{}B’.format(len(profile_data_bytes)), profile_data_bytes))

# Configure the Ping device
myPing.set_speed_of_sound(1400000)  # Set speed of sound to 1400 m/s
print(f"Speed of Sound: {myPing.get_speed_of_sound()}")  # Optional debug output

# Set scan parameters
scan_length = 1000  # mm
scan_start = 0  # mm
myPing.set_range(scan_start, scan_length)
print(f"Scan Length: {scan_length} mm")  # Optional debug output

# Collect and process profile data
for _ in range(1):  # Adjust the range for multiple iterations if needed
    data = myPing.get_profile()
    if data:
        # Decode the binary profile data
        decoded_profile_data = decode_profile_data(data["profile_data"])
        print(
            f"Distance: {data[’distance’]} mm\tConfidence: {data[’confidence’]}%\t"
            f"Transmit Duration: {data[’transmit_duration’]}\tPing Number: {data[’ping_number’]}\t"
            f"Scan Start: {data[’scan_start’]} mm\tScan Length: {data[’scan_length’]} mm\t"
            f"Gain Setting: {data[’gain_setting’]}\tProfile Data: {decoded_profile_data}"
        )
        profile_data_list.append({
            ’Distance’: data["distance"],
            ’Confidence’: data["confidence"],
            ’Transmit Duration’: data["transmit_duration"],
            ’Ping Number’: data["ping_number"],
            ’Scan Start’: data["scan_start"],
            ’Scan Length’: data["scan_length"],
            ’Gain Setting’: data["gain_setting"],
            ’Profile Data’: decoded_profile_data
        })
    else:
        print("Failed to retrieve profile data")
    time.sleep(0.1)

# Save collected data to a CSV file
output_dir = os.path.join(os.path.dirname(__file__), ’..’, ’data’)
os.makedirs(output_dir, exist_ok=True)  # Ensure the output directory exists
output_path = os.path.join(output_dir, "profile_data.csv")
pd.DataFrame(profile_data_list).to_csv(output_path, index=False, sep=’,’)
print(f"Data saved to {output_path}")
```

Matlab codes

The Matlab optimized CPU code for the perfect acoustic reflector configuration can be found here. This is the code for the water-air interface at 30 cm, but it can easily be modified to perform the same simulation at 38 cm. The free field configuration, on the other hand, requires the removal of the water-air interface.

```
    % Grid parameters
dx = 1e-3;           % Spatial step in x [1 mm]
dy = 1e-3;           % Spatial step in y [1 mm]
dz = 1e-3;           % Spatial step in z [1 mm]
Nx = 512;            % Number of points in x (includes 30 cm distance + margin)
Ny = 256;            % Number of points in y
Nz = 256;            % Number of points in z
kgrid = kWaveGrid(Nx, dx, Ny, dy, Nz, dz);

% PML parameters
PML_size = [20, 20, 20];      % PML size in x, y, and z (20 grid points)
PML_alpha = [2, 2, 2];        % PML absorption in x, y, and z (2 Nepers per grid point)

% Water-air interface at Nx/2
medium.sound_speed = 1400 * ones(Nx, Ny, Nz);  % Speed of sound in water
medium.density = 1000 * ones(Nx, Ny, Nz);      % Density of water
medium.sound_speed(1:106, :, :) = 343;        % Speed of sound in air (just after PML)
medium.density(1:106, :, :) = 1.2;            % Density of air (just after PML)

% Source and sensor positions 30 cm from the interface
ball_x_pos = Nx - 106; % 4 cm from the grid end and 2 cm from the PML
ball_y_pos = Ny / 2; % centered
ball_z_pos = Nz / 2; % centered
ball_radius = 25;              % Source radius [grid points]
ball_magnitude = 7943;         % Source amplitude [Pa]

% Create the source
source.p0 = ball_magnitude * makeBall(Nx, Ny, Nz, ball_x_pos, ball_y_pos, ball_z_pos, ball_radius);

% Sensor mask at the same location as the source (monostatic)
sensor.mask = zeros(Nx, Ny, Nz);
sensor.mask(ball_x_pos, ball_y_pos, ball_z_pos) = 1;

% Input parameters for simulation with PML
input_args = {...
    'PMLSize', PML_size, ...                                     % PML size
    'PMLAlpha', PML_alpha, ...                                   % PML absorption
    'PlotLayout', true, ...                                      % Show layout
    'RecordMovie', true, ...                                     % Record video
    'DataCast', 'single', ...                                    % Use 'single' type to reduce memory usage
    'CartInterp', 'nearest'};                                    % Cartesian interpolation

% Run the simulation
sensor_data = kspaceFirstOrder3DC(kgrid, medium, source, sensor, input_args{:});

% Visualization of results
figure;
imagesc(sensor_data, [-80000, 80000]);
colormap(getColorMap);
```

```
ylabel('Sensor Position');
xlabel('Time Step');
colorbar;

% Create time array for Figure 2
dt = kgrid.dt;                   % Simulation time step
Nt = length(sensor_data);        % Number of time steps
t_array = (0:Nt-1)*dt;           % Time array corresponding to time step

% Visualization Figure 2
figure;
plot(t_array, sensor_data, 'LineWidth', 1);
xlabel('Time (s)');
ylabel('Pressure (Pa)');
title('Signal received by the hydrophone');
grid on;
```

The code for the Matlab configuration with 2 layers (water and sand) can be found here. Note that it is almost the same code for the 3 layers (water, mine-like, sand) if we add a layer and replace it with the correct physical characteristics.

```
function result = ElasPropMultiMedium2(varargin)

    p = inputParser;
    addParameter(p, 'size', 0.08); % meters
    addParameter(p, 'cfl', 0.1); % 0.4 seems to be the maximum allowed before
       instability
    addParameter(p, 'points_per_wavelength', 5);
    addParameter(p, 'sim_time', 70e-6); % Total simulation time
    parse(p, varargin{:});

    size = p.Results.size;
    cfl = p.Results.cfl;
    points_per_wavelength = p.Results.points_per_wavelength;
    t_end = p.Results.sim_time;

    f_max = 115000; % frequency of the sonar
    c0_min = 1400; % minimum sound speed in the medium (water)

    dx = c0_min / (points_per_wavelength * f_max); % grid point spacing in the x
       direction [m]
    Nx = 2^nextpow2(round(size / dx)); % number of grid points in the x direction
    dx = size / Nx;

    PML_size = 10;
    Ny = Nx; % number of grid points in the y direction
    Nz = Nx; % number of grid points in the z direction

    dy = dx; % grid point spacing in the y direction [m]
    dz = dx; % grid point spacing in the z direction [m]

    kgrid = kWaveGrid(Nx, dx, Ny, dy, Nz, dz);

    %% define the properties of the upper layer of the propagation medium (water)
    medium.sound_speed_compression = 1400 * ones(Nx, Ny, Nz); % [m/s]
    medium.sound_speed_shear = zeros(Nx, Ny, Nz); % [m/s]
    medium.density = 1000 * ones(Nx, Ny, Nz); % [kg/m^3]

    %% define the properties of the second layer of the propagation medium (sand)
    medium.sound_speed_compression(round(Nx/2):end, :, :) = 2000; % [m/s]
    medium.sound_speed_shear(round(Nx/2):end, :, :) = 800; % [m/s]
```

```
    medium.density(round(Nx/2):end, :, :) = 1200; % [kg/m^3]

    %% define the absorption properties
    medium.alpha_coeff_compression = 0.1; % [dB/(MHz^2 cm)]
    medium.alpha_coeff_shear = 0.5; % [dB/(MHz^2 cm)]

    %% create the time array
    kgrid.makeTime(max(medium.sound_speed_compression(:)), cfl, t_end);

    %% create initial pressure distribution using makeBall
    ball_magnitude = 50; % [Pa]
    ball_x_pos = 15; % [grid points]
    ball_y_pos = round(Ny / 2); % [grid points]
    ball_z_pos = round(Nz / 2); % [grid points]
    ball_radius = 1; % [grid points]
    ball_1 = ball_magnitude * makeBall(Nx, Ny, Nz, ball_x_pos, ball_y_pos, ball_z_pos, ball_radius);

    source.p0 = ball_1;

    %% The following is the position of the sensor so it coincides with the source
    x = (round(-Nx / 2) + ball_x_pos) * dx;
    y = 0 * dy;
    z = 0 * dz;
    sensor.mask = [x; y; z];

    %% define input arguments
    input_args = {'PlotScale', [-2, 2, -0.1, 0.1], 'DataCast', 'single', ...
        'PMLSize', PML_size, 'RecordMovie', true};

    % run the simulation with PML inside
    sensor_data = pstdElastic3D(kgrid, medium, source, sensor, input_args{:});
    result.sensor_data = sensor_data;

    % 3D representation of the monostatic sensor
    voxelPlot(source.p0);
    title('Position of the source');
    voxelPlot(cart2grid(kgrid, sensor.mask));

    figure(3);
    plot(result.t_array, sensor_data);
    xlabel('Time (s)');
    ylabel('Pressure (Pa)');
    title('Signal received by the hydrophone');
    grid on;
end
```

Detection of underwater mines using sonar

Lucas Pirot

Currently, underwater mines and unexploded ordnance represent a persistent threat to maritime navigation and the environment. In submarine warfare, detecting such objects is particularly challenging, especially when they are abandoned and buried under sand. To address this issue, mine countermeasures have been developed that take advantage of various technologies, including acoustic and electromagnetic waves.

Recently, new modeling approaches for ground penetrating radar (GPR) have led to significant advancements in the detection of buried landmines. The aim of this work is therefore to adapt the GPR methodology to enhance the detection and classification of underwater targets using sonar systems.

To achieve this, laboratory experiments were conducted to simulate various scenarios involving a sonar sensor, a sediment layer, and various targets. Particular attention was given to understanding the measurements and pre-processing steps specific to the sensor.

Subsequently, extensive numerical simulations were performed to validate and compare the results obtained experimentally. This comparison involved introducing the concept of a perfect acoustic reflector (PAR), which is useful for retrieving the transfer functions of the sonar-hydrophone-multilayered media system.

These experiments highlighted both the limitations and potential of the model for analyzing realistic scenarios. Technical limitations such as the size of the water tank and sensor limitations, posed challenges to fully achieving the objectives. Despite these difficulties, the results contribute to a deeper understanding of acoustic propagation mechanisms and pave the way for future optimizations in underwater detection applications by using the approach of adapting the GPR methodology.

UNIVERSITÉ CATHOLIQUE DE LOUVAIN
Faculty of bioscience engineering
Croix du Sud, 2 bte L7.05.01, 1348 Louvain-La-Neuve, Belgique | **www.uclouvain.be/agro**